



Devansh Dhard

**Grain-oriented Sputtering of Face Centered Cubic and Body
Centered Cubic Metals**

IPP 2023-07
Juni 2023



Max Planck Institute
for Plasma Physics

Bachelor's thesis

Grain-oriented Sputtering of Face Centered Cubic and Body Centered Cubic Metals

Devansh Dhard
Matr.-No. 03716081

Thesis Submitted in Partial Fulfillment of the Requirements for
the Degree of B. Sc.
in the School of Engineering and Design
at Technical University Munich

Examiners: Prof. Dr. Rudolf Neu
Max Planck Institute for Plasma Physics
Technical University Munich

Supervisor: Dr. Martin Balden
Max Planck Institute for Plasma Physics

Date of Submission: 17th January 2022

Statutory Declaration

I, Devansh Dhard, born on 8th January 1996, hereby declare on oath, that I have written this Bachelor's thesis independently and without outside help and that I have not used any other aids than those indicated.

Garching, 17th January 2022

Abstract

Sputtering occurs in a wide range of applications where charged particles impact on materials. The process of physical sputtering is intensively researched on single and polycrystalline target metals. Crystal orientation significantly influences sputter yield on crystalline targets. Low-indexed planes inside the body centered cubic crystal lattice of tungsten displayed up to an order of magnitude lower sputter yield than high-indexed directions. Extensive knowledge of grain orientation dependent properties of different materials could be beneficial for construction and manufacturing of any component interacting with charged particles, e.g. inside a fusion reactor.

This work aims to find resemblances in grain dependent sputtering of face centered cubic (fcc) and body centered cubic (bcc) crystal structure. Secondary electron (SE) emission efficiency was expected to have linear correlation to sputter yield. Both central questions were investigated with impacting gallium (Ga) ions with energies between 2 keV and 30 keV. The experiments were conducted on the polycrystalline bcc metals tungsten (W) and molybdenum (Mo) alongside the polycrystalline fcc metals copper (Cu) and platinum (Pt). Facilities at the Max Planck Institute for Plasma Physics in Garching include a scanning electron microscope (SEM), which is equipped with a focused gallium ion beam (FIB) and enabled to obtain orientation maps by electron backscatter diffraction (EBSD). Furthermore, a confocal laser scanning microscope (CLSM) was used to determine height profiles. The obtained data were processed with the python tool ‘DataToIPF’ developed by K. SCHLÜTER to combine EBSD images with measured SE intensity pictures or surface erosion data and generate the inverse pole figures (IPF) as full representation of the grain orientation dependence of these two properties.

Both bcc metals display similar grain dependent sputtering behavior with matching locations and distribution of maxima and minima inside the IPF. The fcc metals show promising results but include polishing errors for Cu and insufficient variation of grain orientation of the analysed area and thus insufficient coverage in the IPF for Pt.

For all four metals, SE intensity IPF show great resemblance to the sputter yield IPF with 30 keV Ga ions. The investigated linear correlation between SE emission efficiency and sputter yield is robust for the bcc metals Mo and W but unreliable for the fcc metals Cu and Pt for a 30 keV Ga ion beam. Unfortunately, lower beam energies introduced an unexpected behavior for Mo and Pt. Ga ion deposition might severely alter SE emission efficiency. Consequently, linear correlation was not present for Mo and Pt with 5 keV Ga ions. Furthermore, W and Cu did not display a robust linear correlation for impacting 5 keV Ga ions either.

The workflow for grain dependent property measurement was consolidated and allows quicker analysis of new material choices. The experimental data generated in the frame of this thesis are needed for reference and validation of sputter simulations.

Contents

List of Abbreviations	ix
1 Introduction	1
2 State of the Art	3
3 Background	5
3.1 Crystallography	5
3.1.1 Crystal Directions and Planes	5
3.1.2 Pole Figure and Inverse Pole Figure	6
3.1.3 Crystal Surface Structure	7
3.2 Sputtering	8
3.3 Microscopy	10
3.3.1 Scanning Electron Microscope	10
3.3.2 Electron Backscatter Diffraction	11
3.3.3 Focused Ion Beam	12
3.3.4 Confocal Laser Scanning Microscope	13
3.4 Materials	14
3.4.1 Tungsten	14
3.4.2 Molybdenum	14
3.4.3 Copper	14
3.4.4 Platinum	14
4 Preparation and Methodology	15
4.1 Sample Grinding and Polishing	15
4.2 Specimens	16
4.3 Measurement Process	18
4.4 Data Workflow	19
4.5 Data Filters and Optimization	21
4.5.1 Noise Filter	21
4.5.2 Grain Boundary Filter	22
4.5.3 Levelling and Difference Microscopy	22
4.5.4 Shading Correction	23

4.5.5	Angle Optimization	24
4.5.6	Inverse Pole Figure Generation	25
5	Results and Discussion	27
5.1	Body Centered Cubic Metals	28
5.1.1	SE Intensity of bcc Metals	28
5.1.2	Sputter Yield of bcc Metals	31
5.1.3	Comparison of bcc Sputter Yield and SE Intensity	34
5.2	Face Centered Cubic Metals	38
5.2.1	SE Intensity of fcc Metals	38
5.2.2	Sputter Yield of fcc Metals	42
5.2.3	Comparison of fcc Sputter Yield and SE Intensity	46
6	Conclusion and Outlook	51
	Bibliography	52
	List of Figures	xi
A	Appendices	I
A.1	Shading Correction Python Tool	I
A.2	Specimen Snapshots	IV
A.3	Optimization Filters	V
A.4	Supplementary IPF and Data	VI
A.4.1	SE Energy Series IPF	VI
A.4.2	Platinum Data without Shading Correction	IX
A.4.3	Sputter Yield IPF Linescans	XI
A.4.4	Reference Sputter Yield IPF	XIII

List of Abbreviations

Al	Aluminum
Au	Gold
bcc	Body Centered Cubic
CLSM	Confocal Laser Scanning Microscope
Cu	Copper
EBSD	Electron Backscatter Diffraction
fcc	Face Centered Cubic
Fe	Iron
FIB	Focused Ion Beam
Ga	Gallium
hcp	Hexagonal Close Packed
IPF	Inverse Pole Figure
Mo	Molybdenum
Pb	Lead (Plumbum)
Pt	Platinum
SD	Standard Deviation
SE	Secondary Electron
SEM	Scanning Electron Microscope
W	Tungsten

Chapter 1

Introduction

Nuclear fusion is one of the potential future energy production methods. The fusion reactor must handle plasma with a temperature higher than on the sun. Plasma is the fourth aggregate state with free roaming charged particles. The fusion plasma inside the reactor releases a great amount of energy where charged particles hit the surrounding wall. Physical sputtering is one of the resulting phenomena where particles of the target material are ejected through an incident particle. The divertor inside the reactor is one such surface where hydrogen plasma impurities impact the surface. The material choice for this component is critical as high-energetic, charged particles deposit a lot of heat and eroded particles, which contaminate the plasma. Fusion efficiency is greatly dependent on contamination in the hydrogen plasma and thus this contamination needs to be reduced as far as possible.

Sputtering behavior differs from material to material. While some elements were intensively investigated in the past (e.g. C, Be, W, Fe) and are used in fusion research now (W, Be), new material options may show better behaviour. Grain dependence of sputtering influences the average yield and can alter the properties of manufactured components. Lower sputter yield of new materials may lead to new design of armour materials. Existing material options may also be optimized during manufacturing to reduce (or increase) sputter yield even further without significant change in the production process. The new-found knowledge could also be used to better design components under charged particle exposure and thus lead to better estimations for their lifetime. The aerospace industry might utilize better materials for satellites operating close to the sun or other charged particle rich environments. Some areas where high sputter yield is desired may also profit from better material selection with optimized texture regarding sputtering. Surface coating through sputtering is one of many fields where high sputter yield might be beneficial. Reduced sputter yield on the other hand, has significant impact on the operating time of the previously mentioned divertor which needs regular replacement.

Chapter 2

State of the Art

This chapter outlines the history of sputtering investigations with focus on single and polycrystalline target metals. Current research topics are put into context with previous fundamental literature on sputtering and new findings regarding grain dependent sputtering are elaborated. Finally, the aim of this present thesis is established.

Physical sputtering is a long-researched phenomenon. It is being utilized in a wide range of industrial applications, like sputtering of silver to coat wax vinyl discs [1]. The deposition of sputtered material is the main focus for industrial application with detailed analysis on different sputter deposition processes [2]. Plasma-material interaction focuses on the material interaction with charged particles.

This sputter process was conducted and researched on single and polycrystalline targets. Either single grain orientations were exposed to charged particle fluxes to examine sputtering behavior for single-crystals or the specified sputtering area was large enough to contain a large amount of randomly oriented grains and the measured erosion was averaged over all the grains. The target was sometimes even modelled amorphously neglecting crystallinity of the sample to generate the average sputter yield. Sputter yield of only select crystal orientations were measured with orientations close to the major close-packed crystal plane displaying lower yields by a factor of 2 to 5 [3]. In some experiments, the tilt angle of the impacting ion beam was varied, and a significant variation of the sputter yield across this parameter was found. Furthermore, experiments of fcc crystal lattice structure were conducted for single-crystals and similar sputter yield maxima locations were found for variation of incident angle to crystal orientation for the fcc metals Pb, Au, Cu and Al [3]. Extensive analysis on greater areas inside the inverse pole figure was often difficult to conduct as each angle variation requires precise manufacturing and knowledge of surface geometry before and after ion beam exposure for single-crystals. Investigations on polycrystals were limited by older generation machines which did not provide sufficient detection speed for grain orientation determination through microscopic techniques or enough computing power. That hinders comprehensive analysis of big datasets for a great number of specimens.

Karsten SCHLÜTER [4] developed the statistical methodology in form of a python tool called 'DataToIPF', which reliably combined grain orientation maps with corresponding height or contrast data. Main statements from his work include:

SCHLÜTER showed that sputter yield of higher-indexed crystal orientations like (251) significantly deviate from lower-indexed crystal orientations like (100). It was shown that the sputter yield for tungsten with 30 keV Ga ion exposure differs up to an order of magnitude depending on the grain orientation. Sputter yield was larger by factors of 4 to 10 in higher-indexed crystal directions than crystal orientations with lower index. The overall sputter process showed high sensitivity of less than 1° to the sputter angle. The body centered cubic metal tungsten was analyzed with consistent results for the energy range from 2 keV to 30 keV Ga ion sputtering with conducted computer simulations [5]. The secondary electron emission efficiency under focused ion beam exposure was long known to display crystal orientation dependence and expected to have correlation with sputter yield [6]. A linear correlation was experimentally verified for 30 keV Ga ion FIB data acquisition in the work of SCHLÜTER [4].

This work focuses on two central questions regarding grain orientation dependent sputtering:

1. Is secondary electron intensity in FIB images linearly correlated to the sputter yield?
2. Do metals of fcc and bcc crystal lattice structure show respectively similar sputter yield distribution in the IPF?

This experimental thesis aims to investigate these two central questions by expanding the measured data for tungsten as one bcc metal with molybdenum of the same crystal lattice structure and copper as one fcc metal together with platinum. Energy dependence is studied for the experiments, which aims to generate reliable experimental data for comparison to theoretical simulations like those conducted by Kai NORDLUND with extensive simulation methods [7], [8], [9]. The workflow for grain oriented IPF generation is described in the following chapters and may facilitate future investigations on new material choices.

Chapter 3

Background

This chapter briefly describes the crystallographic background, the physical sputtering phenomenon as well as the measurement equipment and materials investigated. Detailed explanations can be found under these references [10], [11], [12], [13], [14], [15].

3.1 Crystallography

3.1.1 Crystal Directions and Planes

Metals are mostly found in a solid crystal structure at room temperature. Electromagnetic forces between metal ions are material-dependent, and different elements prefer different stable crystal structures. Lattice structure is discussed with the smallest possible repeating pattern, a unit cell. A cube, one such unit cell, with one atom located at each corner is the primitive cubic system seen in figure 3.1.

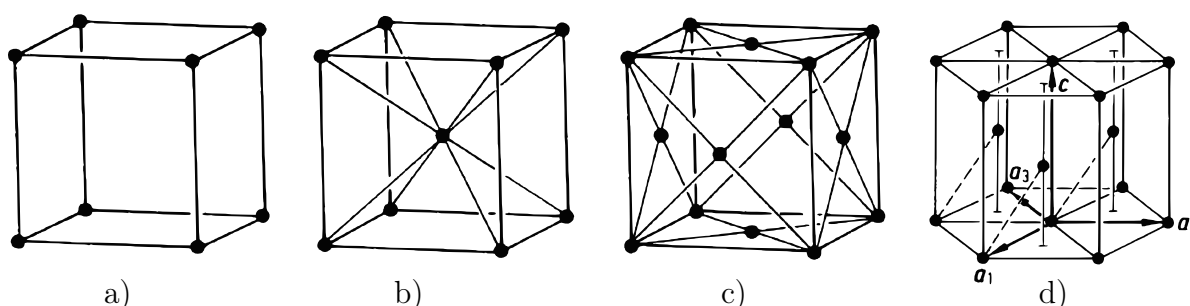


Figure 3.1: Schematic crystal structure of primitive cubic (a), body centered cubic (b), face centered cubic (c) and hexagonal close packed system (d) [10]

The body centered cubic (bcc) system contains one additional metal ion at the volumetric center of the unit cell as seen in figure 3.1. Face centered cubic (fcc) metals contain one additional ion at the center of each face of the unit cube. The majority of technically relevant metals display these two cubic crystal structures (bcc, fcc) with the addition of hexagonal closed packed (hcp) with a hexagonal unit cell. Crystal systems deviate from a perfect regular pattern and contain one or more defects like interstitial atoms, vacancies, dislocations, substitutions, distortion, etc.

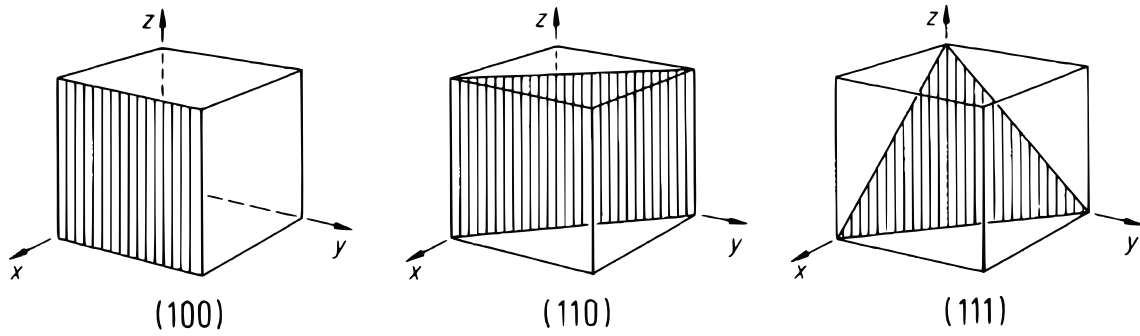


Figure 3.2: Unit cell with coordinate base and planes described with miller indices [10]

Figure 3.2 visualizes the definition of crystal planes and directions with vectors. One corner of the cubic unit cell marks the base with vectors pointing in the three dimensions. Direction families are represented with angle brackets: $\langle 100 \rangle$ contains the equivalent directions $[100]$, $[010]$, $[001]$, $[\bar{1}00]$, $[0\bar{1}]$, $[00\bar{1}]$. Planes are described with the help of miller indices which are calculated with the intersection points between the plane and each axis. Plane families are represented with curly brackets: $\{100\}$ contains all crystallographic equivalent planes (100) , (010) , (001) , $(\bar{1}00)$, $(0\bar{1}0)$, $(00\bar{1})$.

3.1.2 Pole Figure and Inverse Pole Figure

The pole figure is one method to display crystal orientation dependent data. One imaginary unit cell can be placed inside a sphere. Key crystal directions are marked by the piercing points of the vectors through the sphere. One data point is then placed at the sphere and projected to the circular intersection with projection for the corresponding crystal orientation to form the pole figure visible in figure 3.3. The projection method, e.g. stereographic, angle-preserving or area-preserving, defines the properties of a pole figure.

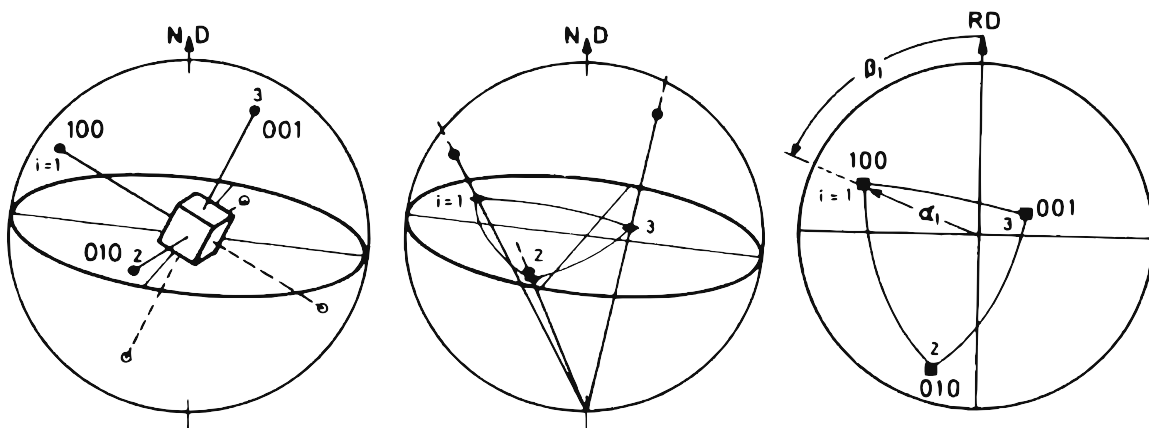


Figure 3.3: Construction of a pole figure [10]

The inverse pole figure can highlight effects that show similar results for equivalent crystal directions and planes like sputtering. The $[100]$ or $[010]$ directions are members of the $\langle 100 \rangle$ direction family and are eroded the same due to symmetry of cubic crystals. The inverse pole figure combines all symmetries inside the pole figure resulting in equivalent subsections. For cubic systems, one of these 24 triangular-shaped regions is chosen to represent all orientations as shown in figure 3.4. This representation is used to display the data obtained in this thesis. This representation is angle-preserving and allows quick analysis of sputtering behavior.

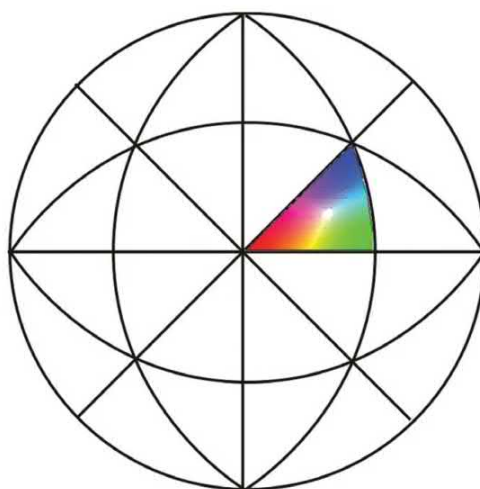


Figure 3.4: Construction of an inverse pole figure: The colored triangle represents one of the 24 directionally equivalent areas for a cubic crystal lattice inside the pole figure. [16]

3.1.3 Crystal Surface Structure

The arrangement of atoms defines the structure of the material. A single crystal sample only contains one regular arrangement of atoms while a polycrystalline sample displays several crystalline grains with grain boundaries in between as seen in figure 3.5. An amorphous sample may only display long-range order which is beyond next-atom distance. The investigated samples were polycrystals with their specific surface structure described in section 4.2. Simulations conducted with SDTrimSP in chapter 5 assume amorphous targets.

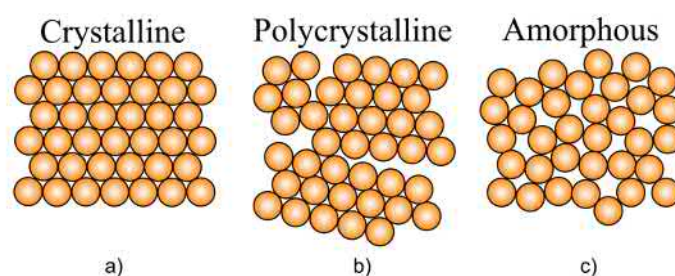


Figure 3.5: Crystalline (a), polycrystalline (b) and amorphous (c) structure [17]

Polycrystalline samples contain several crystalline grains. Figure 3.6a illustrates a texture-free sample where grain orientations of grains are randomly distributed across the surface. A sample surface is 'textured' if one or more grain orientations dominate as shown in figure 3.6b.

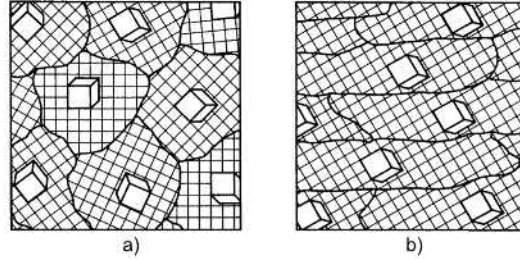


Figure 3.6: Illustration of polycrystalline texture-free (a) and textured (b) surface [10]

3.2 Sputtering

Physical sputtering is a phenomenon that occurs when an energetic particle hits the surface. A sequence of collisions is triggered in the amorphous and crystalline targets by the incident particle with the release of secondary electrons (SE) and sputtered particles alongside other particles. The random behavior of these collisions either results in a reflected particle or the release of one or more target atoms with possible implantation of the incident particle. Sputter yield is the ratio of released atoms to incident particles which may be ions, neutral atoms, neutrons, electrons, or energetic photons [11]. The following formula was used to determine the sputter yield for the experiments in this thesis:

$$SY = \frac{h * \rho}{I * t} * A$$

where SY is the sputter yield, h the erosion height, I the ion current, t the sputter time, ρ the atomic density of the target and A the sputtered area. The sputter yield depends on the binding energy of the target material, the mass ratio of incident particle to target particle, energy of the incident particle and incident angle. Larger binding energy of the target material reduces the sputter yield, as a higher transferred energy component normal to its surface is needed to release a target particle. In order to obtain optimal energy transfer, the mass of the target atom and incident atom should be equal [12]. Low particle energy in the eV-range ('Single-Knock-Regime') may not transfer enough kinetic energy to eject target atoms while particles in the MeV-range ('Spike-regime') penetrate the surface and deposit their energy deeper inside the target. The experiments in this thesis were conducted with the incident particle energy in the keV-range ('Linear-Cascade-Regime') as the energy is then deposited primarily close to the surface. The sputter yield is the largest in this regime. Additionally, the incident angle alters the most probable collision cascades and thus the sputter yield at higher incident beam angle. For the conducted experiment in this thesis, the impact angle of the incident particle is perpendicular to the surface which requires pulse reversal inside the target for particle ejection. Further explanation on sputtering kinetics and collision cascades can be found under [12], [18], [19].

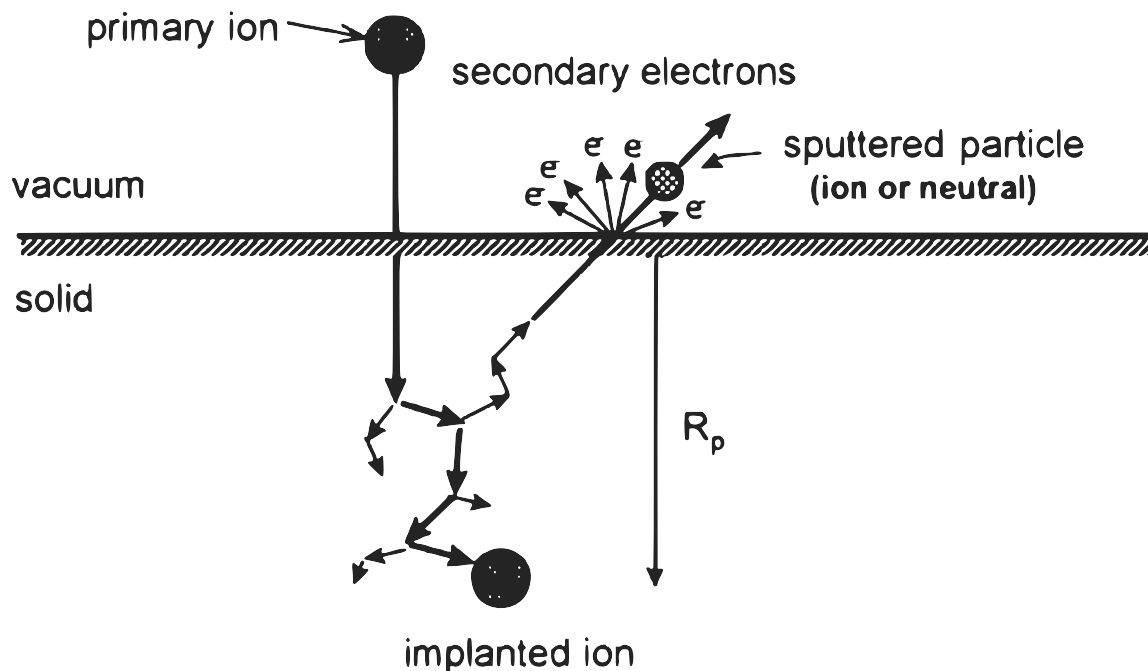


Figure 3.7: Physical ion sputtering: R_p represents the projected range. [20]

The sputter yield varies with changing sputter angle relative to crystal orientation for single-crystal targets and this behavior was assumed to be due to channeling. The incident particle may avoid collision with surface atoms at low-index crystal directions and channel between target atoms. This results in deeper implantation of the particle. This is represented by the projected range and thus energy is deposited deeper inside the target. Consequently, sputter yield is significantly lower for low-indexed planes [19].

Contrary to initial belief, sputter yield is not directly correlated to projected range as researched in [5]. The projected range is one measured result of particle impact as seen in figure 3.7 and it leads to collision cascades but higher projected range does not directly correlate to a lower sputter yield. The significant increase in the projected range close to low-index directions inside the crystal was not proportionally reflected by sputter yield decrease. The target was modeled as a polycrystalline metal which shows significant difference to simulations modeled with an amorphous target. Furthermore, the sputter yield was expected to have direct linear correlation to the energy deposition at surface level [19] and this was further solidified in newer studies [5]. Sputter yield and related molecular dynamics on (poly-)crystalline targets are currently investigated in several studies and go beyond the scope of this thesis.

3.3 Microscopy

EBSD maps, SE intensity images or height data were generated at facilities at the Max Planck Institute for Plasma Physics in Garching. The utilized microscopes and key principles for general data generation are outlined in this section.

3.3.1 Scanning Electron Microscope

The SEM used to conduct the experiments is the HELIOS Nanolab 600 equipped with a Schottky field emission electron gun. Figure 3.8 shows the schematic SE image generation process inside a SEM. The emitted electrons are focused with electromagnetic lenses and form a beam. The sample is scanned in a grid pattern with the emitted electrons detected. Primary electrons are scattered and secondary electrons are generated at the incident location. While primary electrons are backscattered even from deeper atom layers as their energy and mean free pass inside the target is greater, the SE have a lower energy and lower mean free pass. This results in the detection of secondary electrons mainly generated at the surface layers as SE generated at deeper layers cannot escape the target. They characterize the top layers with topographic contrast due to shadowing effects. A lateral resolution of about 1 nm can be reached in the SEM images. A greyscale picture representing the intensity of electrons per pixel is generated [13].

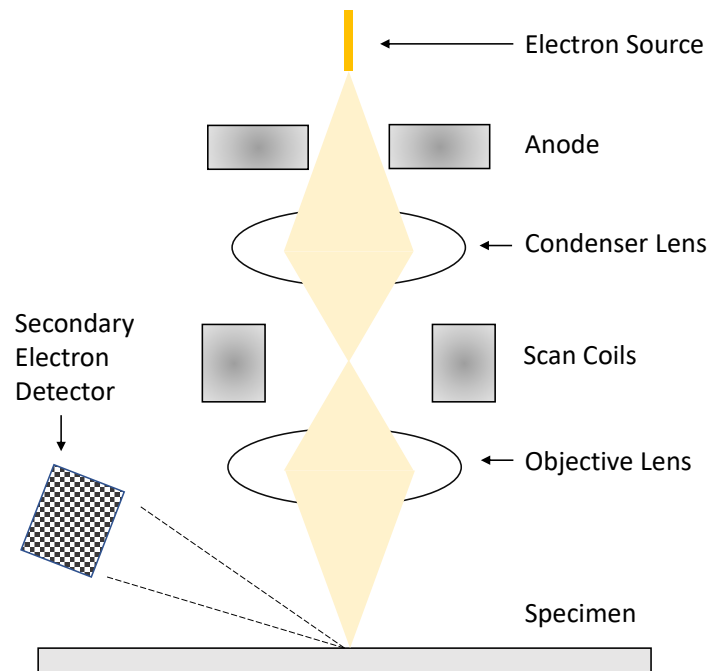


Figure 3.8: General structure of a scanning electron microscope [13]

3.3.2 Electron Backscatter Diffraction

Electron backscatter diffraction (EBSD) aims to detect the crystal orientation present at the surface of a sample. Oxford AZTEC acquisition software with an Oxford Symmetry Detector were utilized to generate grain orientation data. As visible in figure 3.9 the sample surface is hit with an electron beam ideally under an angle of about 70° . The technical limitations inside the HELIOS Nanolab 600 do only allow a tilt angle of 57° for EBSD generation. Backscattered electrons from deeper surface layers are diffracted along the regularly positioned metal ions towards the surface. The conditions for the Bragg formula are met with formation of local maxima if diffracted electrons display constructive interference and minima if the interference is destructive. These extrema are visible on the detector with higher electron intensity for maxima and lower intensity for minima in the half-space. Only variation from the overall electron noise level is considered and they form the so-called Kikuchi pattern. Position of intersections and distance between individual lines in the Kikuchi pattern specify the crystal orientation present at the incident location. The solver in the acquisition software characterizes and maps the detected orientation to the physical location. The sample is scanned in a grid pattern and a pixel map like figure 3.10 where the Euler angles of the crystal orientation are represented is generated.

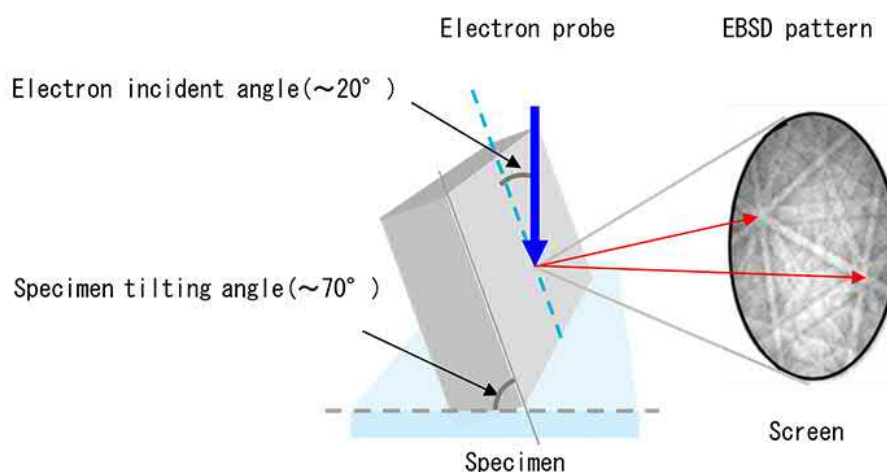


Figure 3.9: Principle of electron backscatter diffraction [21]

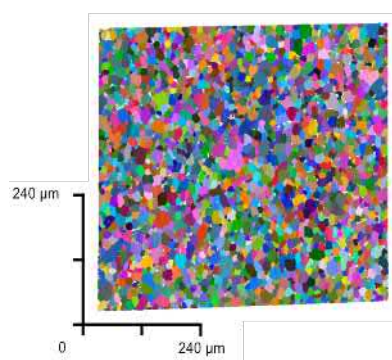
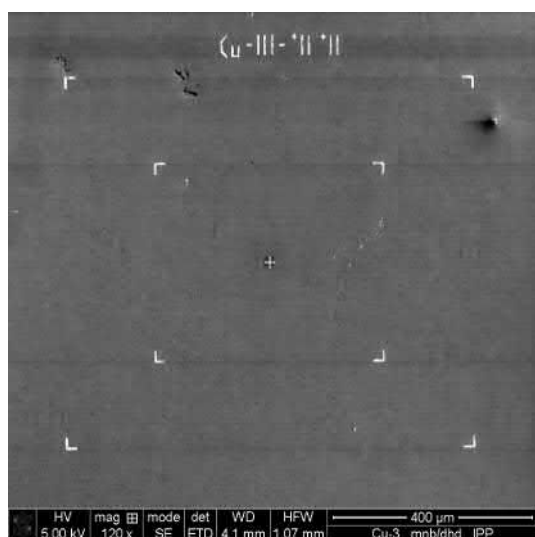


Figure 3.10: EBSD map for a polycrystalline recrystallized tungsten sample: The color encodes the detected Euler angles of the grain.

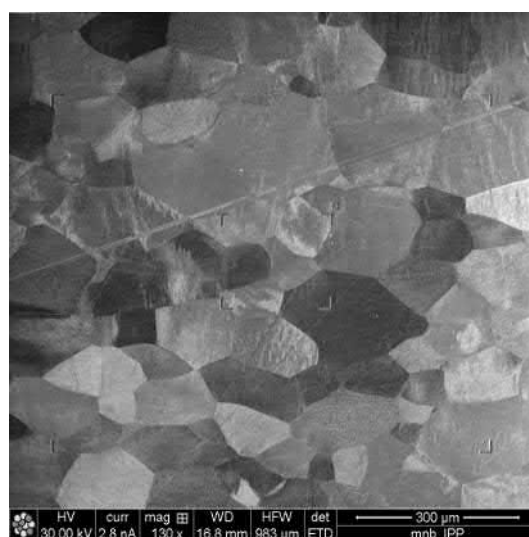
3.3.3 Focused Ion Beam

The HELIOS Nanolab 600 is equipped with a liquid metal source. Ga ions are accelerated with 2 kV to 30 kV and hit the target as a focused ion beam (FIB). The beam forming is very similar to the one for the electron beam in the SEM. There is no ion detector installed but the ions generate secondary electrons, which can be detected. A lateral resolution below 10 nm is achievable, and the same scanning principle as the SEM can be utilized to obtain e.g. images. The FIB was used for:

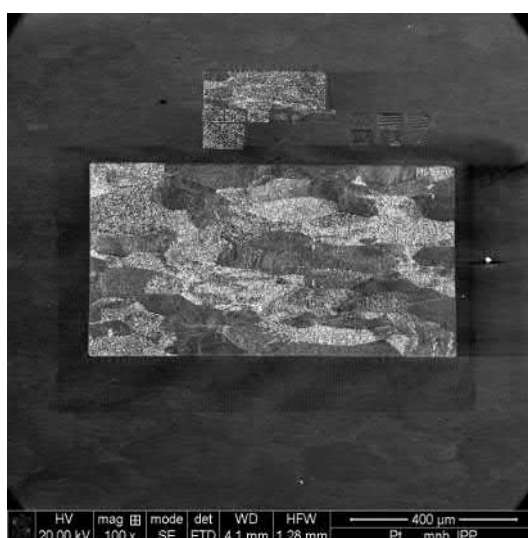
- a) Marker and name placement on sample (see figure 3.11a)
- b) SE intensity image generation (see figure 3.11b)
- c) Sputtering of large areas with max. size: 900 μm x 750 μm (see figure 3.11c)



(a) Electron picture of copper sample displaying marker placement



(b) SE intensity picture of platinum sample



(c) Electron picture of a marked area on the platinum sample after sputtering

Figure 3.11: Images of the samples eroded by the FIB

3.3.4 Confocal Laser Scanning Microscope

The confocal laser scanning microscope (CLSM) Olympus LEXT OLS4000 generated the height data for all samples. This optical instrument uses laser light and a series of lenses to focus light to one plane inside the measurement volume. The target surface reflects the laser light and this reflection is projected onto a pinhole with a detector located behind it. The pinhole ensures that the light from the focus-plane is measured as a maximum in luminosity and light reflected from planes out of focus are measured with lower luminosity. Repeated images are captured for different focus planes associated to their corresponding step motor height of the microscope. The algorithm then reconstructs the topographic sample profile where each pixel is fitted for luminosity vs height and outputs the height profile alongside the intensity image. Such a height image can be seen in figure 3.12b. The lateral resolution is in the μm range and the height direction can be resolved down to 10 nm. Overall scan range in x-y-plane can be increased through image stitching to several mm^2 [14].

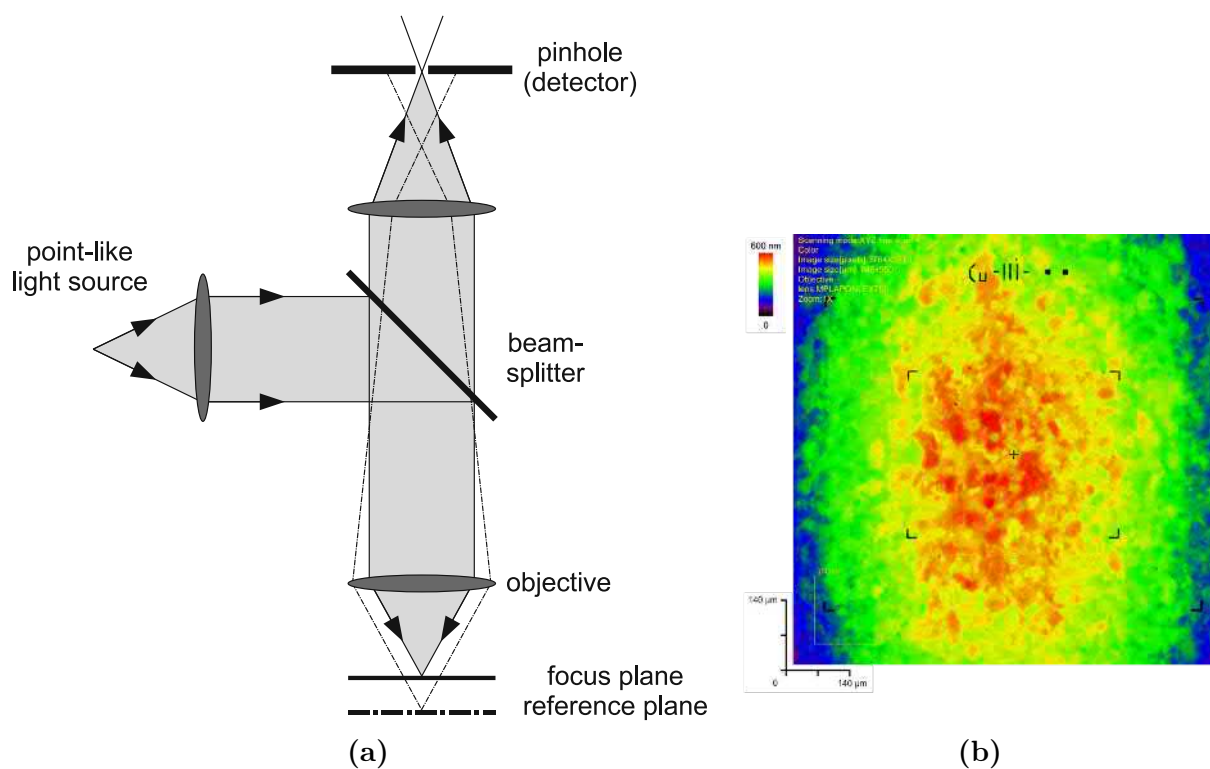


Figure 3.12: Structure of a confocal laser scanning microscope [14] (a) and CLSM image of the Cu sample (b): The red surfaces mark elevated topology while blue surfaces show deeper sections relative to machine height-axis.

3.4 Materials

Different metals were selected based on current availability and suitability where bcc and fcc metals should be represented equally with at least two specimens. The initial sample selection included titanium as a representative of hcp crystal structure and another fcc aluminum sample but they did not produce robust EBSD data due to scratches or other surface defects. The polishing procedure needs further optimization for those samples. Oxidation of samples with residual gas inside the machine and possible reactions with Ga may significantly affect sputtering at lower fluences as experienced with chromium [22]. Some material specific properties are presented in this section.

3.4.1 Tungsten

Tungsten with the atomic number of 74 is a brittle metal with the highest melting point of all metals of 3415°C. A thin oxide layer is formed on the surface of pure tungsten that protects it from further corrosion through oxygen in the air. Tungsten has a body centered cubic lattice structure at room temperature. It is widely used for high temperature applications and can also form strong and high temperature resistant alloys with other metals [15].

3.4.2 Molybdenum

Molybdenum with the atomic number of 42 is a blue-grey shiny hard and brittle metal. It has very good electrical conductivity and is self-passivating. This surface oxide layer protects the underlying structure against air, water, or not-oxidizing acids. Molybdenum has a body centered cubic lattice structure at room temperature. It is widely used as a component for industrial alloys and is easier to machine and process than tungsten [15].

3.4.3 Copper

Copper with the atomic number of 29 is a yellow-red shiny and ductile metal. Its crystal structure at room temperature is face centered cubic. It has one of the highest thermal and electrical conductivity among all metals and is thus used in electrical wiring and cooling applications. It also shows good corrosion resistance [15].

3.4.4 Platinum

Platinum with the atomic number of 78 has a face centered cubic crystal structure at room temperature. The silver-white shiny noble metal display low hardness and is relatively ductile. Platinum is widely used in alloys for medical equipment, catalysts, thermocouples, and many more [15].

Chapter 4

Preparation and Methodology

This chapter outlines the methodology from specimen grinding and polishing to data acquisition inside the SEM and CLSM. The experimental process is described and the data processing to generate the IPF is stated. Finally, the interpretation of the IPF types used in this thesis is elaborated. While data generation inside the SEM and CLSM follow universal steps for all specimens, grinding procedure and data processing were sample-specific. Each experiment step is described in the following sections.

4.1 Sample Grinding and Polishing

A flat sample surface is a key factor for grain orientation detection with EBSD. Distorted layers from improper polishing can alter the Kikuchi patterns. Better alignment in the CLSM with reduced acquisition time for larger areas and less shadowing effects due to surface roughness inside the SEM are advantages of a levelled sample surface. Grinding and polishing can achieve a flat surface but a mirror like surface is difficult to achieve due to the mechanical toughness of specific grains and (grain dependent) variation of the etching rate in the final polishing step. The process must be tailored to the specimen and material which requires a lot of experience.

Polishing was kindly performed by Katja Hunger. Some specimens were previously prepared for different studies [4], [22]. The general process included water-cooled grinding by the grinding machine Phoenix 4000. Increasingly fine SiC grinding paper of granular up to 4000 was used for 1 min on each sample. Finer polishing was performed differently for each sample. The tungsten sample was electropolished with the Struers LectroPol-5 with a 1.5 % NaOH solution for 1 min under 19 Volt. The copper sample was polished with 1 μm sized diamond particles for 5 min and then vibration polished by the Vibromet by Buehler for 90 min. The other samples received vibration polishing for 120 min.

4.2 Specimens

The specimen should have no texture as far as possible and adequately sized grains. Uneven polishing can create unwanted morphological changes to the surface. If one sample shows texture, less present orientations are insufficiently represented within the analyzed area. Only few orientations can be observed within the marked area if grain size is too big while in return very small grain sizes are affected more strongly by polishing imperfections. Erosion might progress into the next layer if sputter depth is too great relative to grain size. This section briefly describes the grain structure and height profile with stitched snapshot pictures of all samples in appendix A.2.

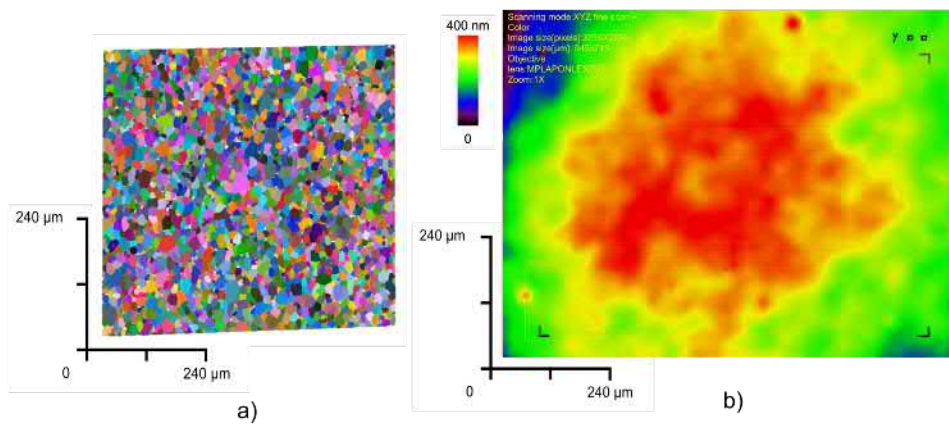


Figure 4.1: EBSD map (a) and CLSM image (b) of W specimen

The tungsten sample contains grains around 10 μm in size. As the sample was recrystallized, the individual grains are uniform and without distortions or defects. Clear boundaries are visible in figure 4.1a. In the CLSM plot in figure 4.1b, the surface displays marginal bumps of about 100 nm in height. Electropolishing creates the modulation in height with lateral size of several grains.

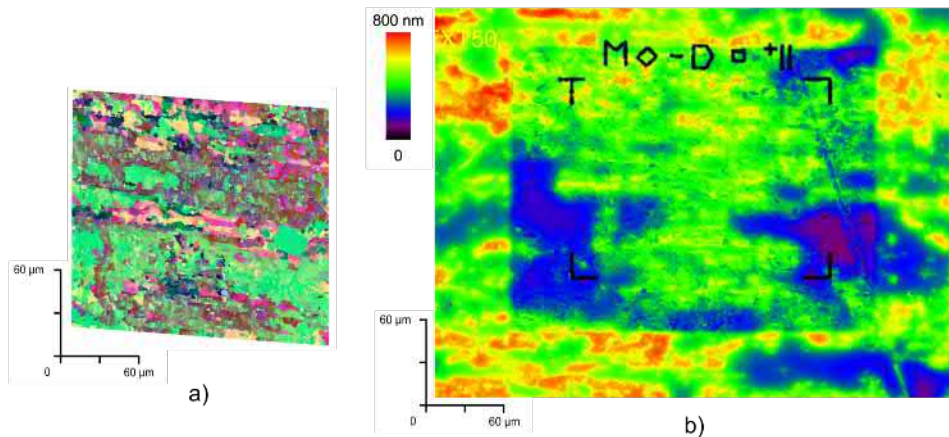


Figure 4.2: EBSD map (a) and CLSM image (b) of Mo specimen: Please note the rectangular depression from FIB sputtering for sputter yield determination.

The molybdenum sample displays a bimodal grain structure distribution. The deeper situated, blue areas visible in figure 4.2b contain grains with up to 25 μm in size with some dominant crystal orientations. In figure 4.2a few distortions are visible here. The smaller higher located structures contain significantly smaller grains of around 1 μm in size. A diverse set of crystal orientations is visible in these elevated regions with grains containing distortions.

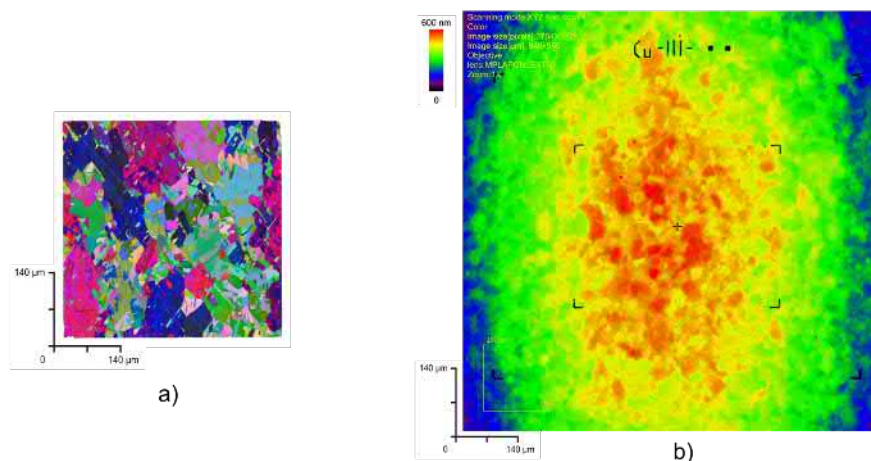


Figure 4.3: EBSD map (a) and CLSM image (b) of Cu specimen

The copper sample includes a variety of grain orientations with individual grain size ranging from 10 to 20 μm . The majority of grains display distortions which increase the variety of detected orientations and thus cover a wider area in the IPF. Slips and crystal twins are visible in figure 4.3a, too. The grain pattern is partially visible on the CLSM height plot 4.3b. Some grains thus were less or more affected by polishing.

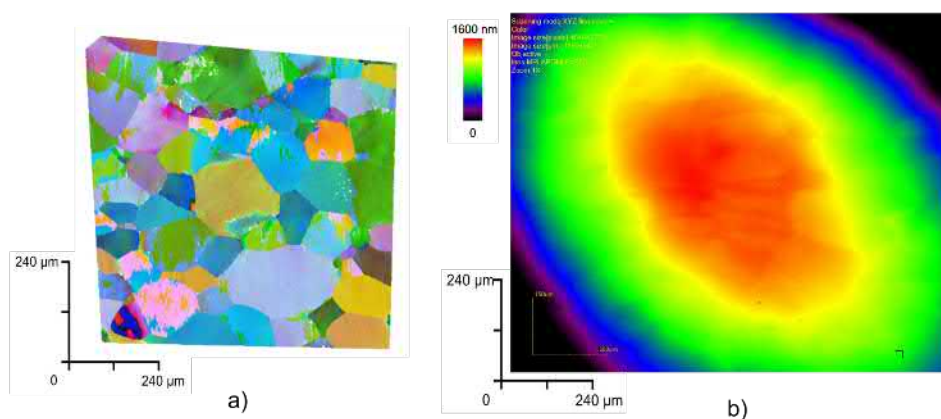


Figure 4.4: EBSD map (a) and CLSM image (b) of Pt specimen

The platinum sample consists of large grains sometimes extending up to 200 μm visible in figure 4.4a. The large grain size limits the amount of grains and orientations accessible in the marked area. The grains themselves are uniform across their surface without significant distortions. Crystal twins are present in some grains. The surface of the platinum sample displays faint grain topology with a spherical curve visible in figure 4.4b.

4.3 Measurement Process

The SE intensity image generation with the FIB and the sputter yield experiments with 30 keV and 5 keV Ga ion beam were conducted with the kind help of Martin Balden. The polished sample is first marked with the FIB. The marked area can then easily be relocated in all instruments. The marked positions are assigned to one experiment type as shown in figure 4.5. Each sample undergoes both workflows visible in figure 4.6 at their respective marker locations with additional studies on the sample in advance, e.g., the flux-series, which is a quick test to rule out unexpected phenomena in relation to fluence as occurred on chromium in earlier studies [22].

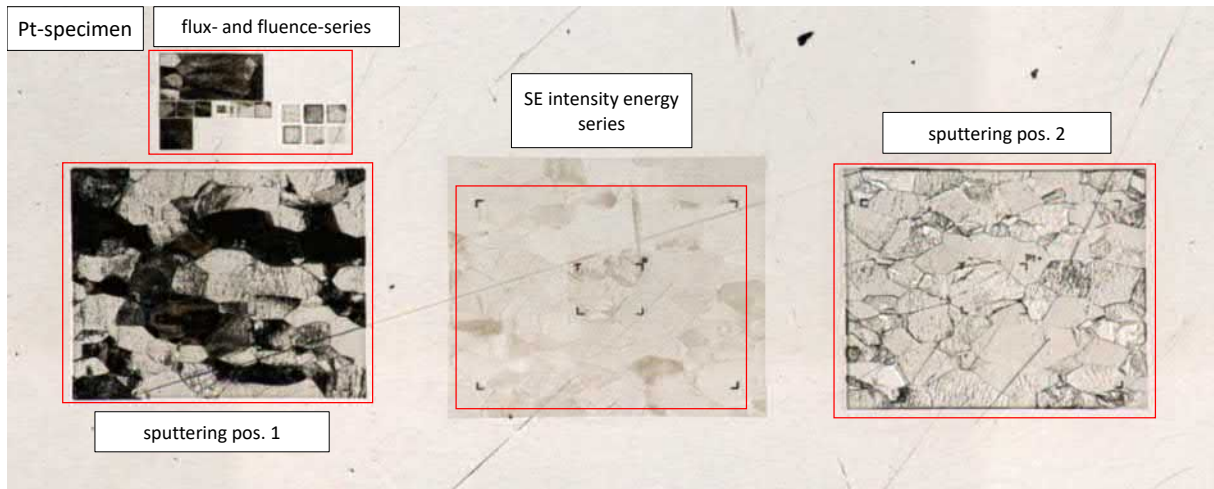


Figure 4.5: Picture of marker placement and experiment classification on platinum sample: The location for each specific experiment is marked.

For SE intensity image generation, the marked area is first characterized with EBSD to generate the grain orientation map for data merging. The highest Ga ion energy of 30 keV is selected, to sputter possible remaining debris from polishing and remove the thin natural oxide layer from the surface, and the FIB scans the surface in a grid pattern. The Ga ion energy is varied in discrete steps from 30 keV over 16 keV, 8keV, 5 keV to 2 keV and back to higher energies. The greyscale intensities of the grains inside the image shift during the initial phase of beam exposure and reach an equilibrium within 3 to 10 mins. Multiple images of the same FIB energy were compared to find possible correlation between previous lower or higher energy FIB exposure, which did not occur. The contrast image characterizes the surface through the SE emission efficiency of the near surface atoms. This image is saved to generate the SE intensity IPF plots. This measuring process is comparatively quick as everything is performed inside one machine with EBSD detection speed mainly defining the overall time needed. The full energy series excluding material specific EBSD detection time took less than 1 day per sample. In the future, sputter yield IPFs for other samples or metals can be generated more rapidly with this process if the first central question, that the SE have a linear correlation to sputter yield, turns out true for all energies.

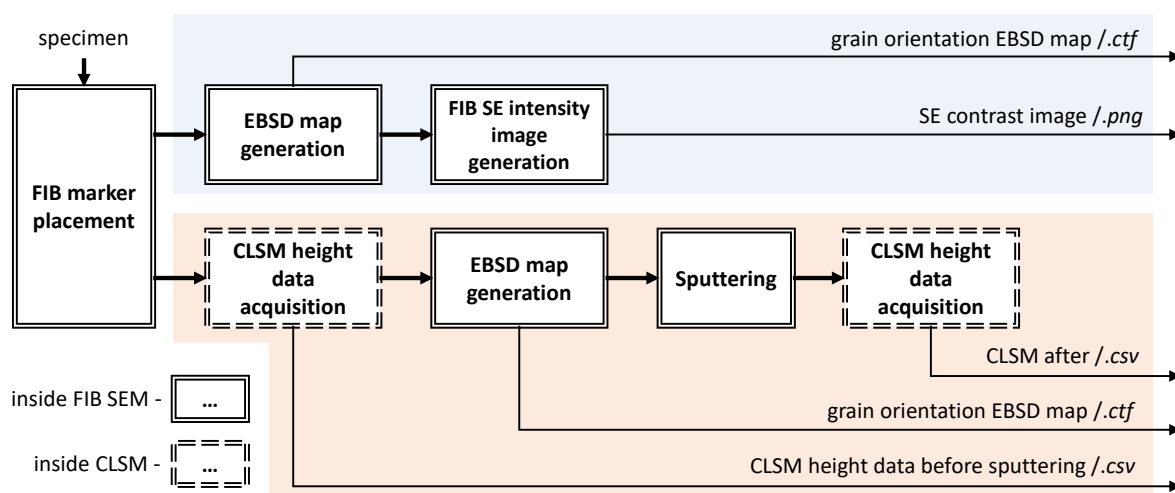


Figure 4.6: Measurement workflow for IPF data generation: The upper blue path outlines the steps for SE intensity image generation. The lower orange path outlines the steps for obtaining sputter yield.

The acquisition of the needed data for obtaining sputter yield takes significantly longer and involves the CLSM data acquisition before sputtering in order to apply difference microscopy. The sample is mounted into the CLSM after marker placement to generate the height map before beam exposure. Then the sample is remounted into the SEM to characterize the surface with EBSD for the EBSD map. The sputtering is then performed with the 30 keV and 5 keV Ga ion energy with the incident angle of the FIB normal to the surface. Sometimes EBSD is performed again after sputtering. The sample is once again mounted into the CLSM to obtain the height profile after sputtering. Sputtering alone can take easily longer than one day, e.g. more than 60 hours for 5 keV with Ga ions on W and several mounting and dismounting between two microscopes may create errors.

4.4 Data Workflow

K. SCHLÜTER programmed a python tool 'DataToIPF' capable of merging grain orientation maps with other maps displaying a property, e.g. a contrast or height map. Figure 4.7 describes the workflow to generate the data IPF shown in this thesis. The tool encompasses all steps except intensity shading correction, which was performed with a new self-written python tool 'shading correction'. The data workflow is described in this section while the new tool 'shading correction' is elaborated in appendix A.1 in more detail.

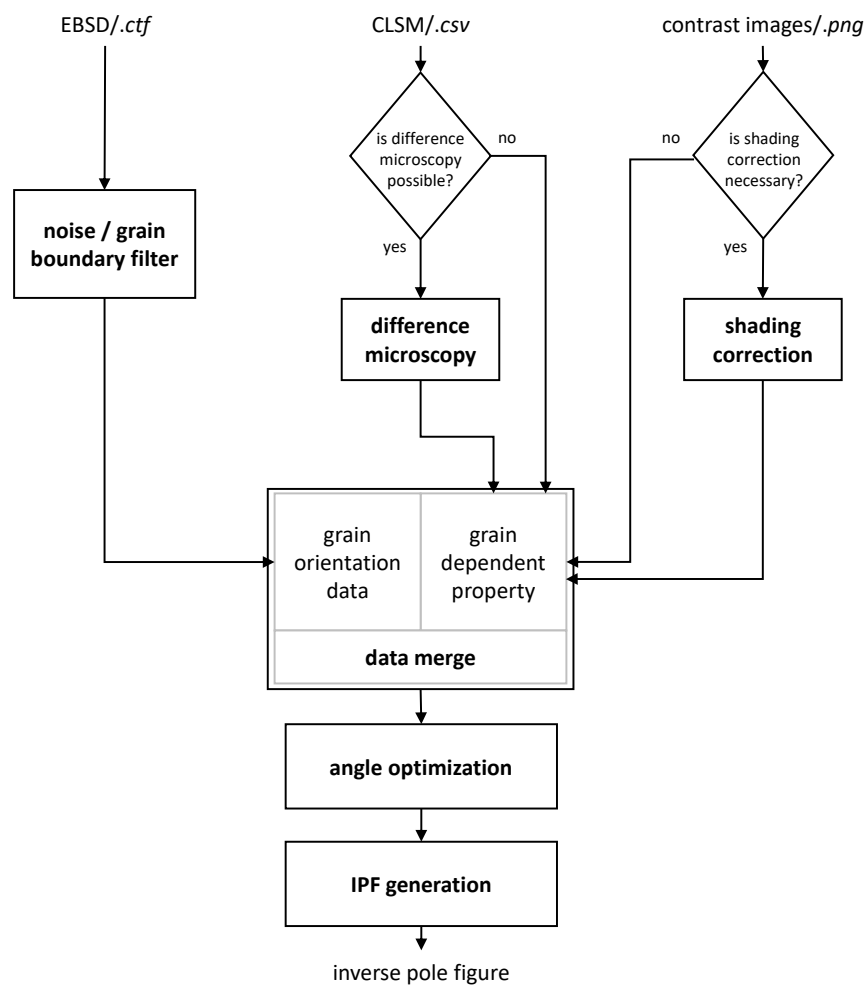


Figure 4.7: Workflow of EBSD, contrast and CLSM data with difference microscopy, filters and optimization

The EBSD data acquired before sputtering is saved as ctf files and undergoes cleanup through an optional noise and grain boundary filter. This grain orientation map is then merged either with CLSM height data of csv type or images like the SE intensity images of png or jpeg type. CLSM data should undergo difference microscopy if possible and intensity shading correction can be applied to images if necessary. The merged file can already be used to display the IPF but angle optimization under the minimum error principle should be utilized for more reliable results. Each individual block is elaborated in the next subsections.

4.5 Data Filters and Optimization

Only reliably detected and processed data pixels should be merged with height or intensity data. Grain boundaries, dust particles, remaining debris from sample preparation, deep plastic scratches or angle differences due to tilted or imperfectly polished surfaces are reasons for improper grain orientation detection. While most mentioned disturbance factors can be eliminated with adequate sample preparation, surface texture is primarily affected by the manufacturing process and recrystallization or other heat treatment. Cleanup of unreliable data, e.g. along grain boundaries can be achieved with different filters and evaluation techniques after the measurement.

4.5.1 Noise Filter

The EBSD map displays the measured grain orientation represented by many pixels where each is the solution to the diffracted Kikuchi-pattern. Plastic deformation, dirt particles, an oxidized metal layer or other phenomena may wrongly classify one pixel inside an otherwise homogenous grain. Such spike errors can be discarded with a noise filter. If one pixel value greatly exceeds the average of all other values inside a specific area, the abnormally classified orientation is discarded. This is shown in figure 4.8.

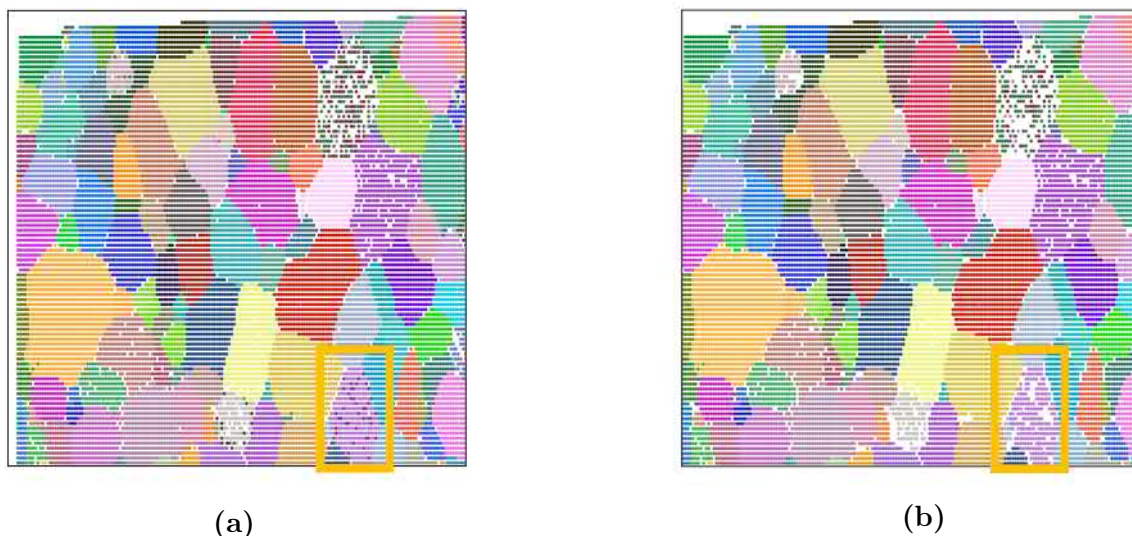


Figure 4.8: EBSD map before (a) and after (b) applying the noise filter: Spike errors visible in the yellow rectangle got discarded by the noise filter.

4.5.2 Grain Boundary Filter

At grain boundaries the Kikuchi patterns from adjacent grains are superimposed. This superposition of patterns or height steps developed during polishing and resulting shadows may not allow clear orientation classification through the solver in the EBSD acquisition software. Additionally, spatially dislocated EBSD and height or SE intensity data may wrongly match data to the adjacent grain. These errors are localized along grain boundaries and can be discarded through a filter. The grain boundary filter discards all pixels in a predefined area of specific size if the orientation difference between two measurements exceeds a threshold. This filter can reliably separate different grains from another. One should carefully adjust the filter parameters as a great amount of reliable data can get discarded and random spike errors might be considered as a separate grain. The effect of the grain boundary filter is illustrated in figure 4.9.

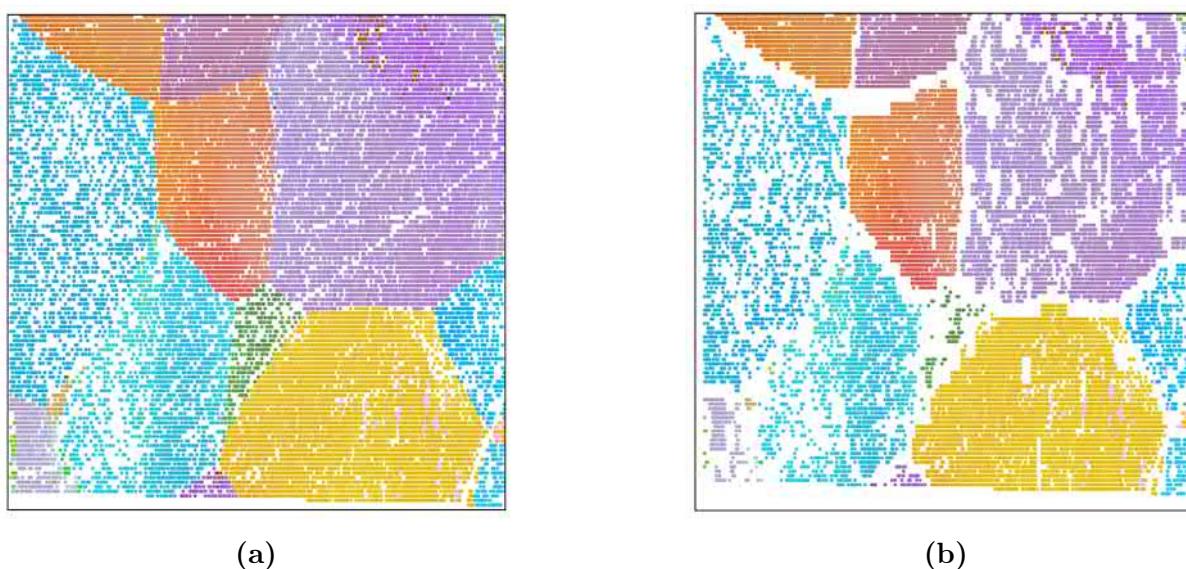


Figure 4.9: EBSD map before (a) and after (b) applying the grain boundary filter: The EBSD data was filtered with an exaggerated setting for illustrative purpose. Grains are clearly separated but even correctly classified datapoints were discarded.

4.5.3 Levelling and Difference Microscopy

The CLSM data measures the absolute height of the specimen from a machine specific reference zero level. Surface geometry as well as all imperfections are captured with one measurement. Geometric levelling can approximate the best fitting level plane onto the dataset through the minimization of distances between a datapoint and the fitted plane as shown in figure 4.10. Subtracting this plane from the data can correct mounting errors and thus previously tilted surfaces can be levelled post measurement. The use of geometric levelling should be carefully considered as wrongly applied levelling can distort the data.

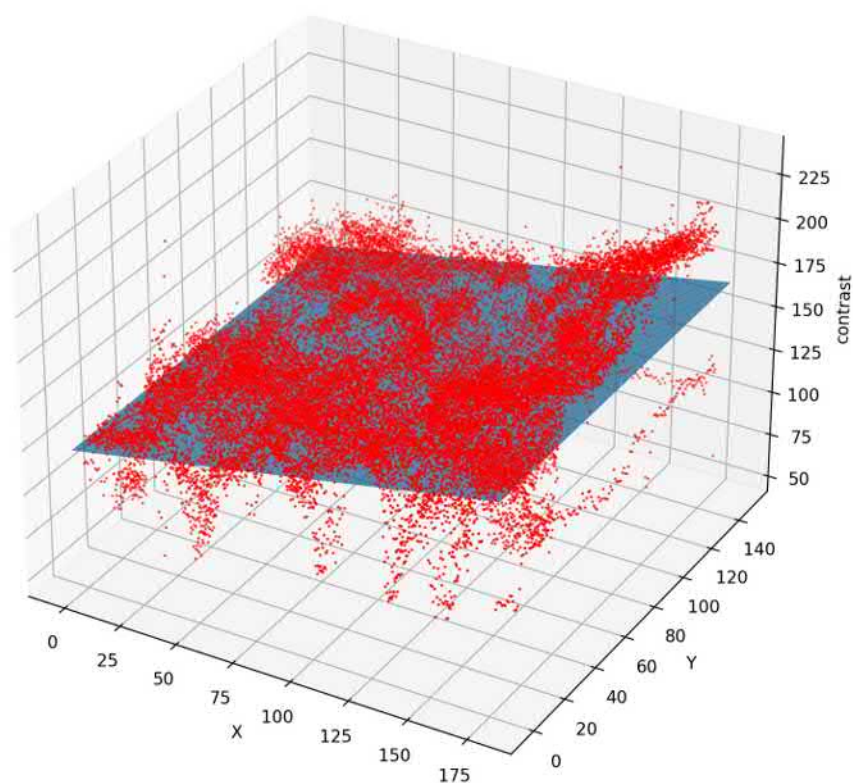


Figure 4.10: Geometric levelling through a linear fitted plane

Difference microscopy is a more effective method for data evaluation compared to levelling alone. If CLSM data is measured before and after the ion beam exposure, these two height maps are then projected onto each other through an affine transformation. This ensures that even distorted maps are accurately subtracted. The effect of sputter erosion can be isolated and warped surfaces, polishing morphology and scratches as well as other plastic imperfections are discarded. Geometric levelling then orients the height difference to the reference axis and eliminates resulting tilt error from the subtraction.

4.5.4 Shading Correction

Some SE intensity measurements showed a visible change in shade along the diagonal from left top to bottom right corner as visible in figure 4.11. The resulting merged data showed high standard deviation for individual pixels. This effect might be occurring due to a wide area scan covering the size of about 1x1 mm and the SE detector physically located right to the imaged area. The three-dimensional electric field for SE detection might not be uniform across this large area. Preparation imperfections like warped surfaces can geometrically reduce or increase the SE detection count rate for tilted surfaces. A fitted paraboloid can be subtracted from the measured data under the assumption that the contrast level should be uniform across the measured surface as grains are randomly oriented. The resulting intensity picture displays no contrast shade. This data optimization process should be used carefully as it greatly alters the detected raw data and consequently the location and magnitude of maxima in the IPF plots.

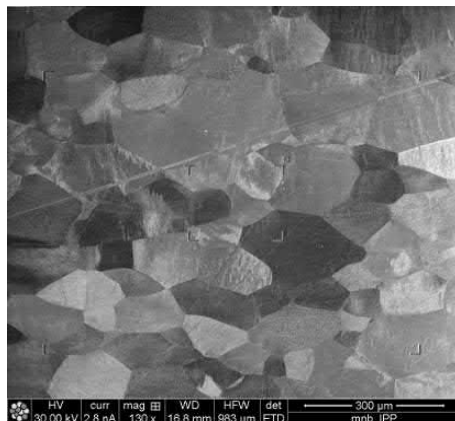


Figure 4.11: Example for visible contrast shade in SE intensity image of platinum

4.5.5 Angle Optimization

Sputtering of metals is sensitive to angle misalignments of 1° [4]. Mounting and dismounting the specimen can apply a rotation to sputter yield data if EBSD generation and sputtering are not performed in succession. Furthermore, machine-specific design tolerances or misalignment of the FIB and stage apply unwanted rotations. Data optimization under the minimal error principle can be utilized post measurement. The influence of this optimization was evaluated for each sputter yield measurement and once for each SE intensity series with the result applied to the whole set of IPFs. Some examples are provided in appendix A.3. For minimum error optimization, a reduced dataset for faster computing is rotated and tilted within a given range and the resulting standard deviation IPF plot (described in the next subsection) characterizes the applied rotation. A map, with each pixel representing the mean standard deviation over the complete IPF at one applied rotation, is generated and the minimum location indicates the most reliable angle misalignment as shown on figure 4.12. This rotation is then applied to the whole dataset, and therefore the location of maxima are more accurately described in the IPF.

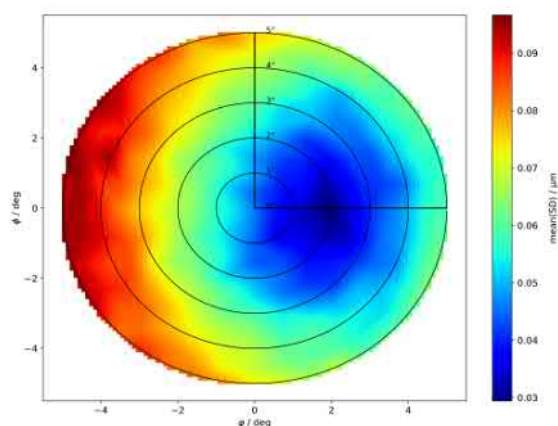


Figure 4.12: Polar plot of minimum error optimization on incident beam angle: The color represents the mean standard deviation over the complete IPF plot at one applied rotation of the EBSD dataset. The minimum location indicates the most probable incident angle for the ion beam.

4.5.6 Inverse Pole Figure Generation

The IPF displays one property with respect to the grain orientation of the crystal. The IPF in figure 4.13 are generated through the merge of grain orientation data from EBSD and property data, e.g. SE intensity information. The EBSD map and data image are matched through an affine transformation and the data value is coupled to the specific grain orientation present at its position. Crystallographic similar crystal orientations are rotated into one of the 24 triangles of the pole figure described in section 3.1.2 and corresponding data points are accumulated. Euler angles and thus crystal orientation result in a point representation in the IPF. Several adjacent orientations inside the IPF are pooled and one pixel now represents a close set of crystal orientations with the 'resolution' parameter defining the size of each pixel. Lower resolution spatially covers a greater area in the IPF and thus contains more grain orientations. Each pixel contains multiple data points and this is desired for statistical analysis for each pixel. A cut-off filter for IPF generation can now discard pixels containing few data points. The median value of the data points is determined to represent the specific grain orientation of the pixel. The data IPF in figure 4.13a maps the measured grain dependent property to the crystal orientation, e.g., the SE intensity IPF and sputter yield IPF. The count IPF in figure 4.13b represents the amount of data points measured in relation to their grain orientation. The SD IPF in figure 4.13c describes the standard deviation for each pixel inside the IPF.

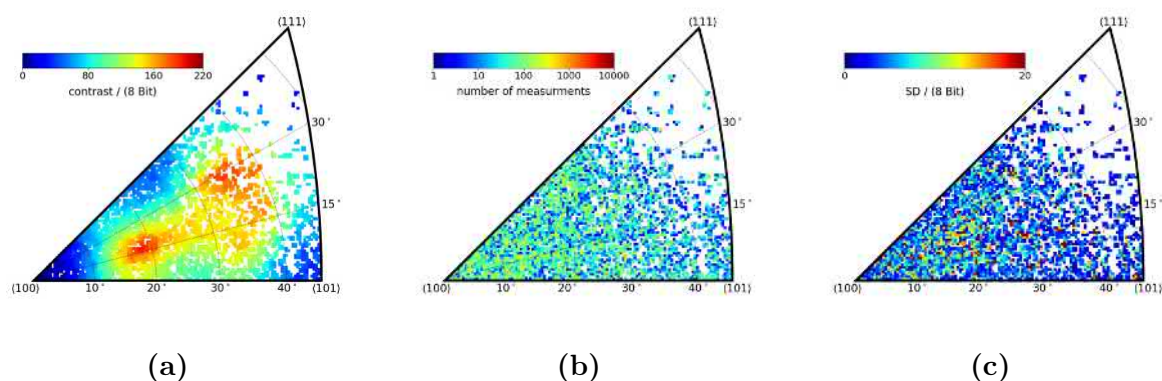


Figure 4.13: Data IPF (a), count IPF (b) and SD IPF (c) for W: A pixel inside the IPF equals about 1° , which is the expected accuracy achievable after data optimization. Pixels containing less than 3 data values were discarded with the cut-off filter.

Chapter 5

Results and Discussion

This section elaborates the results acquired by the measurement process. We expect to see similarities with sputtering yield for the body centered cubic metals molybdenum and tungsten as well as for the face centered cubic metals copper and platinum. First the SE intensity results are elaborated, and sputter yield through FIB erosion is discussed in the subsequent section for bcc and fcc, respectively. Matching SE intensity IPF and sputter yield IPF of materials of the same crystal lattice structure may support the second central question that similar crystal structure display alike grain dependent sputtering behavior. The sputter results are then compared with the SE intensity results to determine similarities which could confirm the first central question of this thesis that SE emission efficiency is linearly correlated to sputter yield.

Each measurement type requires adequate processing to better isolate the sputter phenomenon. Different processing types as described in section 4.4 were utilized to generate the best possible result. The connection between IPF and the measurement process and the specimen texture are put into context. Some of the measurements showed unexpected results. These unexpected occurrences are discussed after the general description of the IPF. Only relevant IPF were used to discuss key aspects in this chapter. The full set of IPF generated for this thesis can be found in appendix A.4.

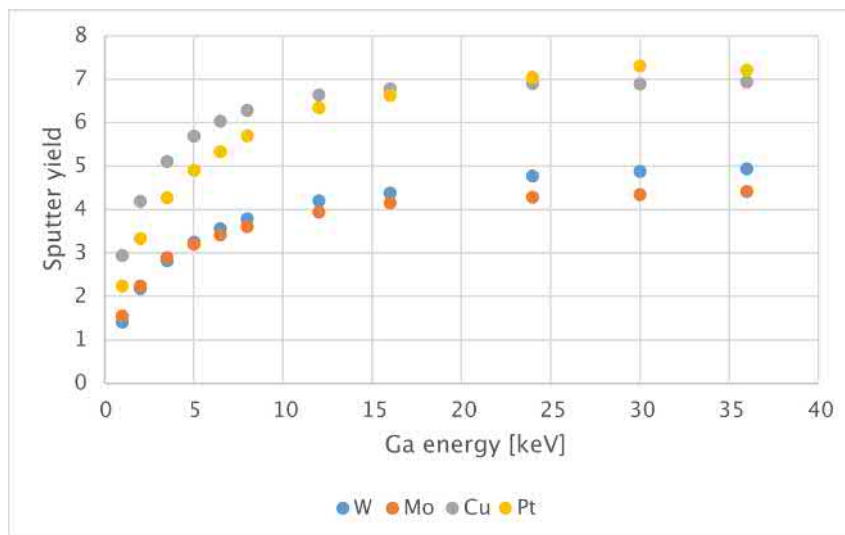


Figure 5.1: SDTrimSP [23] sputter yield simulation results

Simulations with the software SDTrimSP [23] were conducted to determine the expected average sputter yield for all metals over the range of 1 to 36 keV. The Ga ion beam hits the surface perpendicular to it and an amorphous target was used for the simulation. Rodrigo Arredondo kindly provided these simulation results.

The average sputter yield mainly decreases for lower beam energy in figure 5.1. We expect to be in the 'Linear-Cascade-Regime' mentioned in section 3.2 where the sputter yield is highest. The 'Single-Knock-Regime' spans incident energies up to several 100 eV [12] and thus should be beyond the lowest Ga ion energy of 2 keV but the energy range selected in this thesis may display phenomena from the surrounding regimes.

5.1 Body Centered Cubic Metals

5.1.1 SE Intensity of bcc Metals

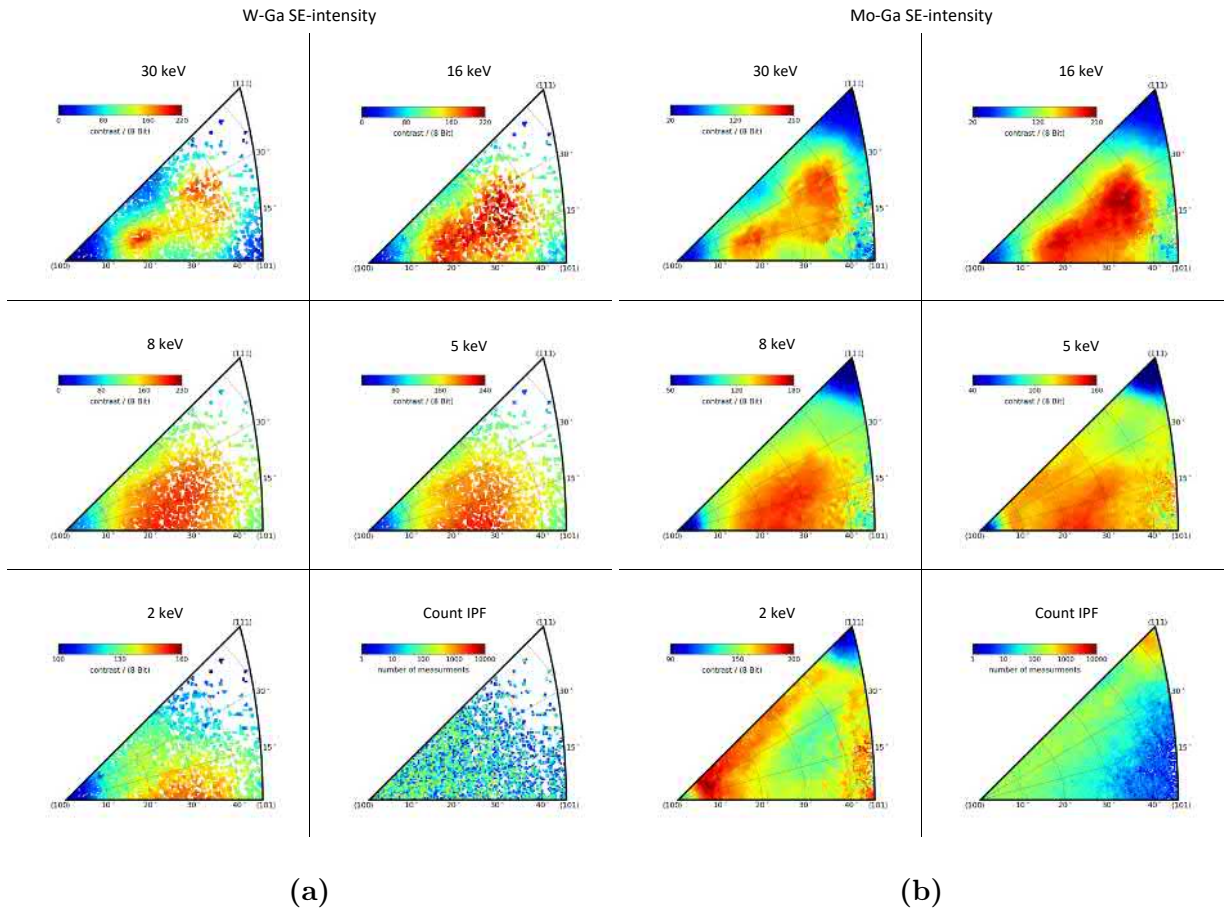


Figure 5.2: SE intensity energy series IPF for the bcc metals tungsten (a) and molybdenum (b): The count IPF in bottom right corner is same for all measurement as images were taken from the same area. SD IPF are provided in appendix A.4.1

Figure 5.2 shows the SE intensity energy series performed on the bcc metals tungsten and molybdenum with a Ga ion beam. The SE intensity IPF for molybdenum and tungsten with 30 keV Ga ions display great resemblance. The positions of maxima in the IPFs align

when tracing out the 20° and 40° arc. The hammer-like shape with its handle oriented towards the left (100) corner is clearly present in both. The standard deviation in those areas of higher intensity is greater for molybdenum. The greater amount of measured orientations in the molybdenum count IPF provides more data points for each individual pixel and thus increasing the confidence in the results. The locations of maxima shift towards the bottom edge and increasingly flatten for lower energy beams. This effect is visible for both tungsten and molybdenum SE plots until an energy of 5 keV is reached. The 5 keV molybdenum SE intensity IPF deviates from the development of tungsten at 5 keV. The maximum is broader and not as localized as the maximum of tungsten at the bottom edge. At 2 keV molybdenum shows unexpected results as the maximum is located around the edge of the IPF except for the top (111) corner. Contrary to this, tungsten shows its intensity maximum at the bottom edge with a gradual decline in all directions. Conclusively, SE intensity IPF for molybdenum may not be trustful below 8 keV.

The count IPFs for both metals also reflect the texture of the materials. Tungsten shows texture as the top (111) corner of the count IPF in figure 5.3b is less populated. These specific grain orientations were not present in the selected area of measurement and other pixels are uniformly spread across the count IPF. Each grain is uniform and displays almost no distortions. This is related to the individual point like appearance in the count IPF as each grain orientation is separated with clearly visible boundaries. The standard deviation is low, which is represented by the low span of 20 (compared to 256 which is the maximum '8 Bit value') in the SD IPF plot in figure 5.3c.

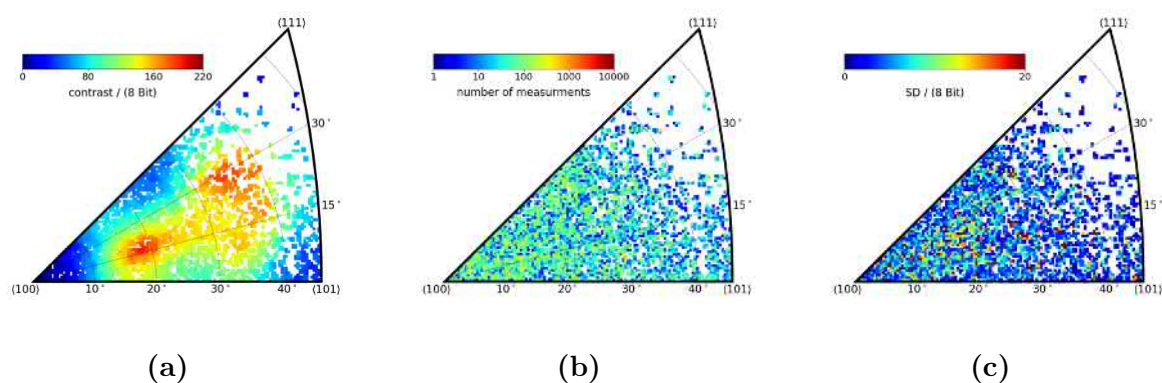


Figure 5.3: W 30 keV Ga ion energy SE intensity IPF (a), count IPF (b) and SD IPF (c): This plot is a magnified figure from the SE intensity energy series of W (see figure 5.2a)

Molybdenum displays a bimodal grain size distribution as described in section 4.2. There are large grains in the top (111) corner in the count IPF in figure 5.4b, which leads to an order of magnitude more measured orientations. Smaller distinctly located areas contain a variety of other grain orientations. The bottom right (101) corner is less populated thus SE intensity results in the SE intensity IPF in figure 5.4a show more inconsistencies there. The grain size in these smaller surface areas is very small and individual grains display distortion. Some grains do not show a clear boundary. This is reflected by the distributed green area in the count IPF in figure 5.4b. The standard deviation is high at specific locations in the SD IPF in figure 5.4c but the overall high amount of measured orientations along with the selection of the modal value for one specific pixel inside the IPF described in section 4.5.6 increases the confidence of an accurate reading.

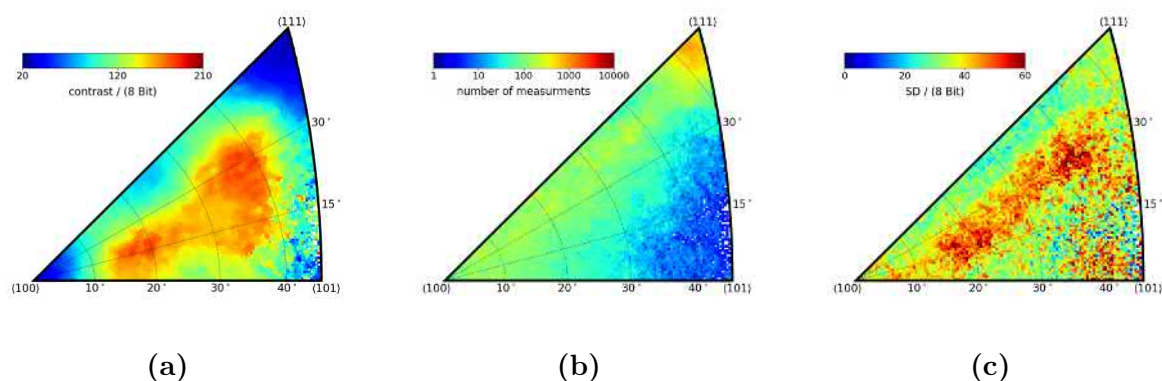


Figure 5.4: Mo 30 keV Ga ion energy SE intensity IPF (a), count IPF (b) and SD IPF (c): This plot is a magnified figure from the SE intensity energy series of Mo (see figure 5.2b)

The 2 keV SE intensity IPF of molybdenum in figure 5.5 greatly differs from the expected result. Further investigation showed unexpected behavior for some grain orientations. These seemed to flip in SE intensity under the exposure of lower energy beams and previously brighter grains darkened significantly as darker grains lightened up. This effect was reversed when a higher FIB energy was selected. This phenomenon was reproducible when alternating between high and low beam energy. Ga deposition might be one cause for this unexpected behavior as Ga ions deposit more frequently at lower energy and affect the SE emission efficiency of the surface.

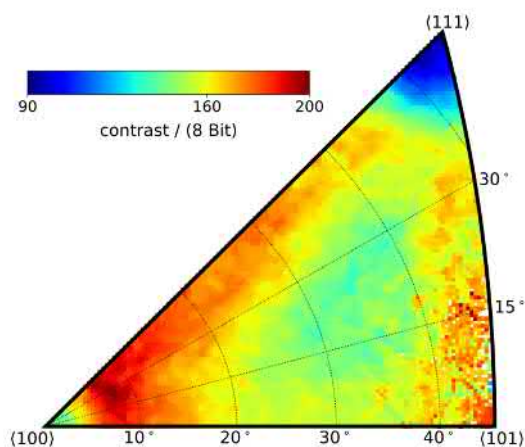


Figure 5.5: Molybdenum 2 keV Ga ion energy SE intensity IPF: This plot is a magnified figure from the SE intensity energy series of Mo (see figure 5.2b)

5.1.2 Sputter Yield of bcc Metals

The sputter yield IPFs for molybdenum and tungsten with 30 keV Ga ion energy in figure 5.6a and figure 5.7a show great resemblance. The hammer like maximum with its handle oriented towards the left (100) corner, as described in the previous section 5.1.1, is clearly visible for both bcc metals. The consistently low standard deviation indicates reliable results. Molybdenum shows inconsistencies in the right (101) corner and tungsten contains fewer data points close to the top (111) corner. Both occurrences are due to the texture of the used materials with low population in the corresponding areas. The sputter yield of the molybdenum maximum is 15 percent higher than for tungsten whereas the simulated average sputter yield with SDTrimSP was 12 percent lower for molybdenum (see figure 5.1). The maximum sputter yield for both metals is 3 to 8 times higher compared to their respective minima. While tungsten displays sputter yield close to or lower than 1 in the low-indexed directions, molybdenum shows sputter yields higher than 2 in the low-indexed crystal directions.

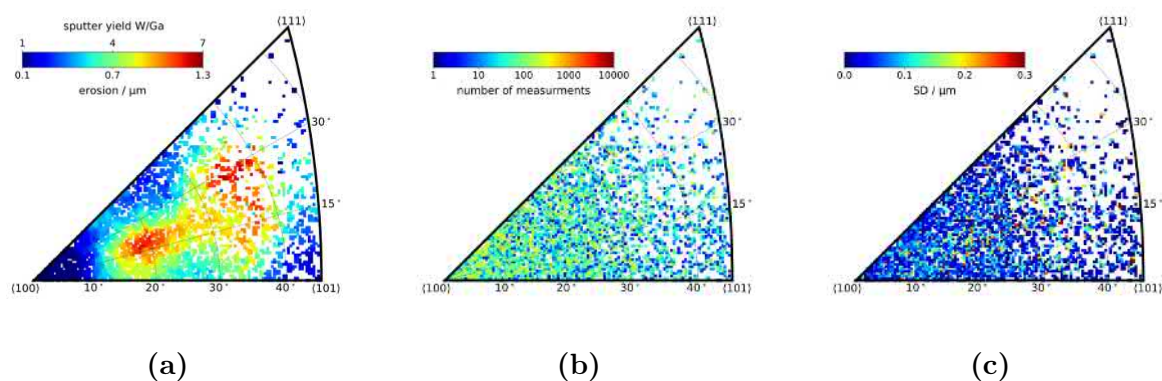


Figure 5.6: W 30 keV Ga ion energy sputter yield IPF (a), count IPF (b) and SD IPF (c)

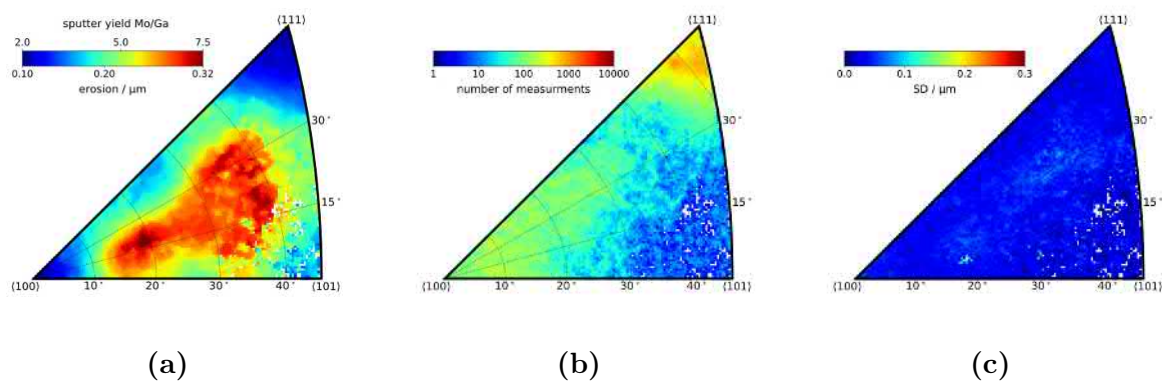


Figure 5.7: Mo 30 keV Ga ion energy sputter yield IPF (a), count IPF (b) and SD IPF (c)

The sputter yield IPF for molybdenum and tungsten with 5 keV Ga ion energy in figure 5.8a and figure 5.9a do not match completely. The minima in the left (100) and top (111) corner are present in molybdenum. Tungsten also reliably displays the minimum at the left (100) corner and an estimated one in the top (111) corner. The texture of tungsten does not provide enough data points for reliable extrapolation but experiments from K. SCHLÜTER [4] show a minimum in the top (111) corner for tungsten. The sputter yield maximum of tungsten visible at the bottom edge, which gradually decreases in all directions, is not clearly visible in the molybdenum sputter yield IPF. Only the outline of the maxima oriented towards the diagonal edge between the left (100) and top (111) corner can be reliably discerned with inconsistent sputter yield distribution towards the bottom edge and right (101) corner. The molybdenum count IPF in figure 5.9b displays few measured grain orientations in the inconsistent area with a standard deviation of up to 0.1 μm . The overall erosion span for molybdenum at 5 keV Ga ion energy exposure is only 0.17 μm . Therefore, the data at the estimated maximum for molybdenum is uncertain.

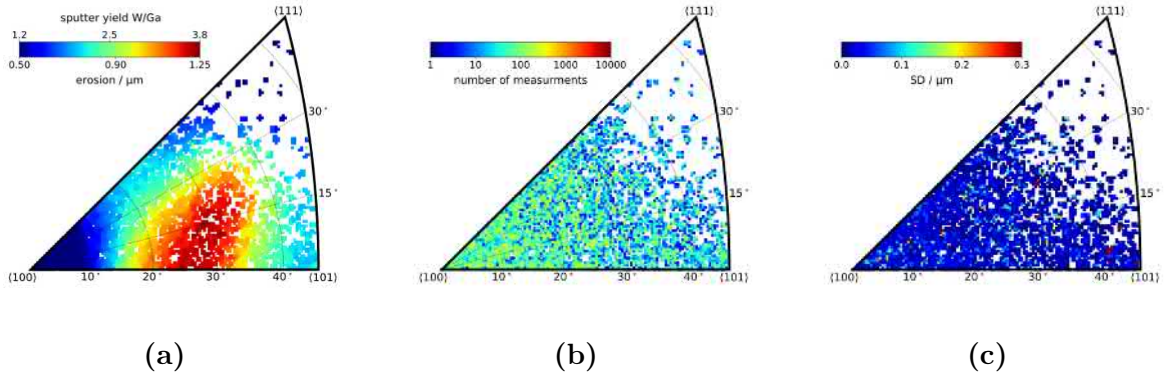


Figure 5.8: W 5 keV Ga ion energy sputter yield IPF (a), count IPF (b) and SD IPF (c)

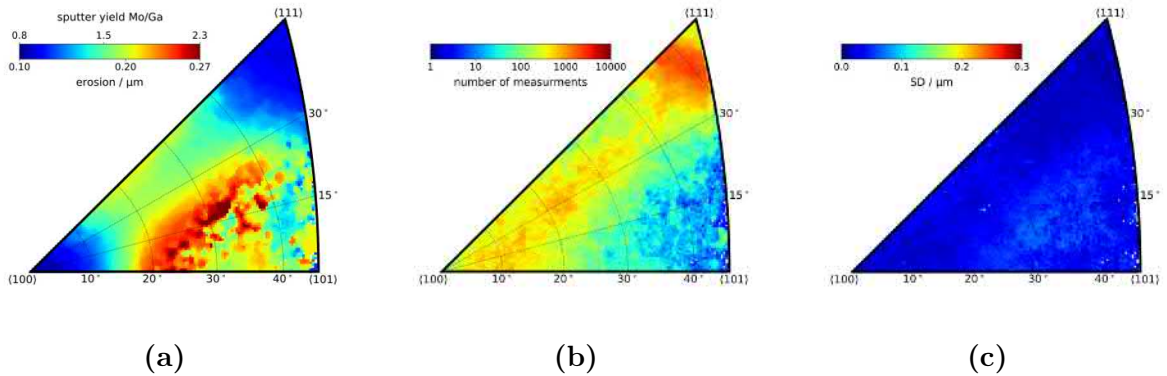


Figure 5.9: Mo 5 keV Ga ion energy sputter yield IPF (a), count IPF (b) and SD IPF (c)

The small grain size of molybdenum was taken into consideration for the sputter experiment. A low sputter depth of 0.25 μm was chosen prior to beam exposure. The EBSD measurements in figure 5.10 still show shifted or completely eroded grains which the color shift indicates.

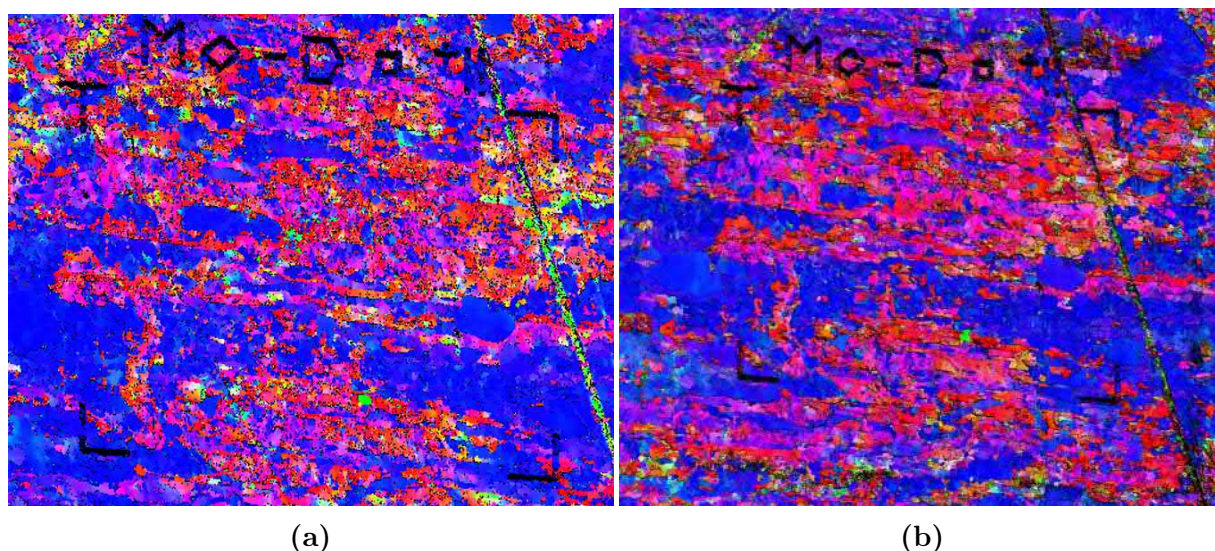


Figure 5.10: EBSD map of molybdenum sample before (a) and after (b) 5 keV Ga ion beam exposure: Please note the reduction of green and yellow pixels and thus grain orientations after (b) beam exposure.

The different EBSD maps in figure 5.10 used for data processing result in different sputter yield IPF for molybdenum. Height data was merged with EBSD maps generated before and after sputtering and the resulting sputter yield IPF are shown in figure 5.11. Boundaries for the minima are less clear in the EBSD merge after exposure. The estimated maximum at the bottom edge is even less clear with a significant portion of high yield area flipped. The right (101) corner is less populated and shows missing data points compared to the EBSD merge prior sputtering in figure 5.11a. These grains may have been fully eroded with the FIB.

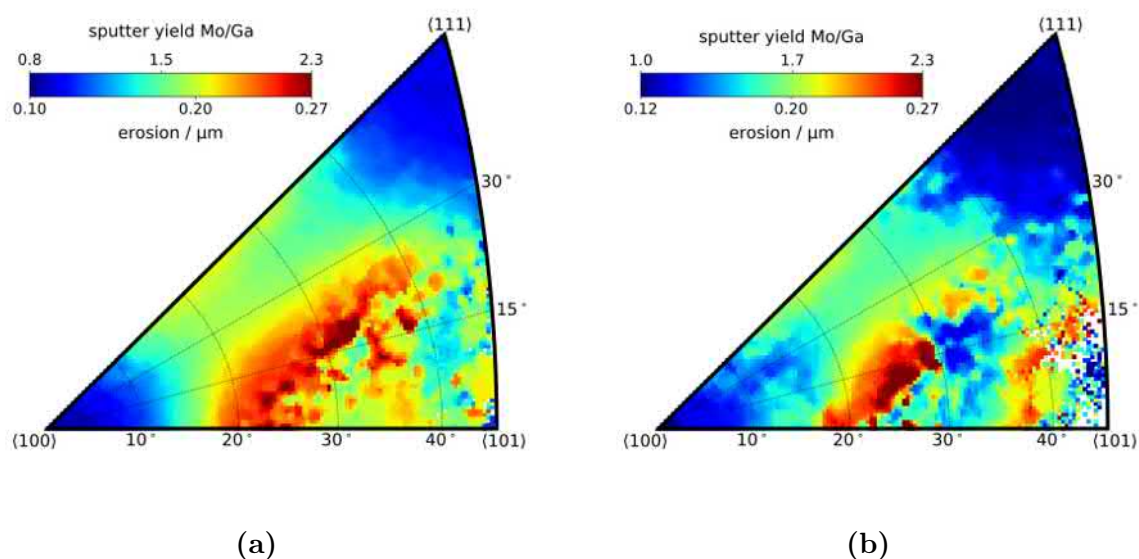
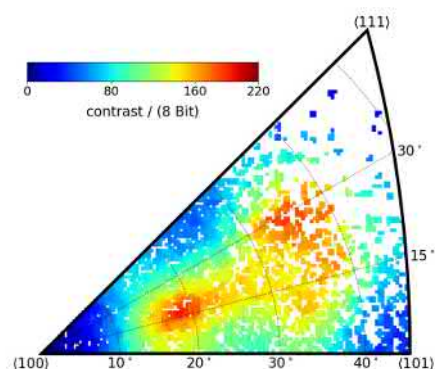


Figure 5.11: Mo CLSM data merged with EBSD map generated before (a) and after (b) sputtering with 5 keV Ga ion beam

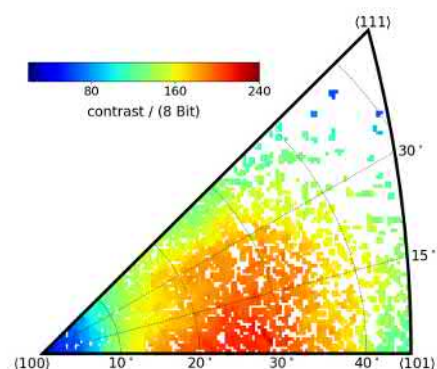
These uncertain positions from possibly completely eroded grains, which may even display the sputter yield of the underlying grain, can be eliminated in future experiments. A computational comparison of the EBSD map before and after sputtering can reveal altered grain boundary location. This modified area can be eliminated from the initial EBSD map to only include confident data points for data processing.

5.1.3 Comparison of bcc Sputter Yield and SE Intensity

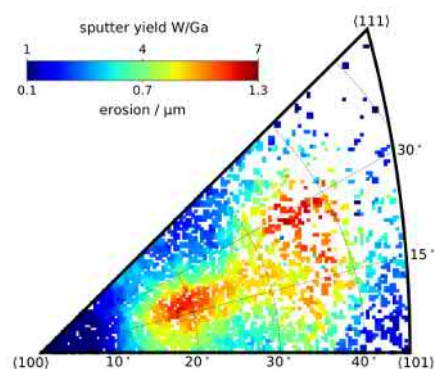
For 30 keV Ga ion energy on a tungsten target, the comparison of SE intensity IPF and sputter yield IPF shows matching results as visible in figure 5.12. Position and intensity of maxima and minima align with similar intensity decline in both IPF. For 5 keV Ga ion energy the intensity IPF displays a wider maximum with a more gradual decrease in all directions compared to the sputter yield. The location of minima and maxima match for both IPF.



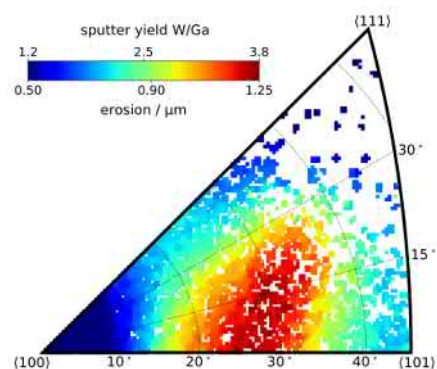
(a) W SE intensity IPF with 30 keV Ga ions (from figure 5.2a)



(b) W SE intensity IPF with 5 keV Ga ions (from figure 5.2a)



(c) W sputter yield IPF with 30 keV Ga ions (see figure 5.6a)



(d) W sputter yield IPF with 5 keV Ga ions (see figure 5.8a)

Figure 5.12: Comparison of SE intensity IPF and sputter yield IPF for tungsten sputtering with a 30 keV and 5 keV Ga ion beam

The plots in figure 5.13 correlate the intensity inside the 30 keV and the 5 keV SE intensity IPF in figure 5.2a with the 30 keV sputter yield IPF in figure 5.6a and 5 keV sputter yield IPF in figure 5.8a with colored datapoints representing their crystal orientation. One specific grain orientation inside the sputter yield IPF is matched with the corresponding orientation in the SE intensity IPF. The matched sputter yield and SE intensity values are shown in the plot. A linear correlation between sputter yield and SE intensity is visible in figure 5.13 for a Ga ion energy of 30 keV. The 5 keV correlation plot slightly deviates from a robust linear correlation. The data points seem to follow an imaginary 'S-curve' with lower incline in the left half of the plot and gradual rise towards higher intensity values.

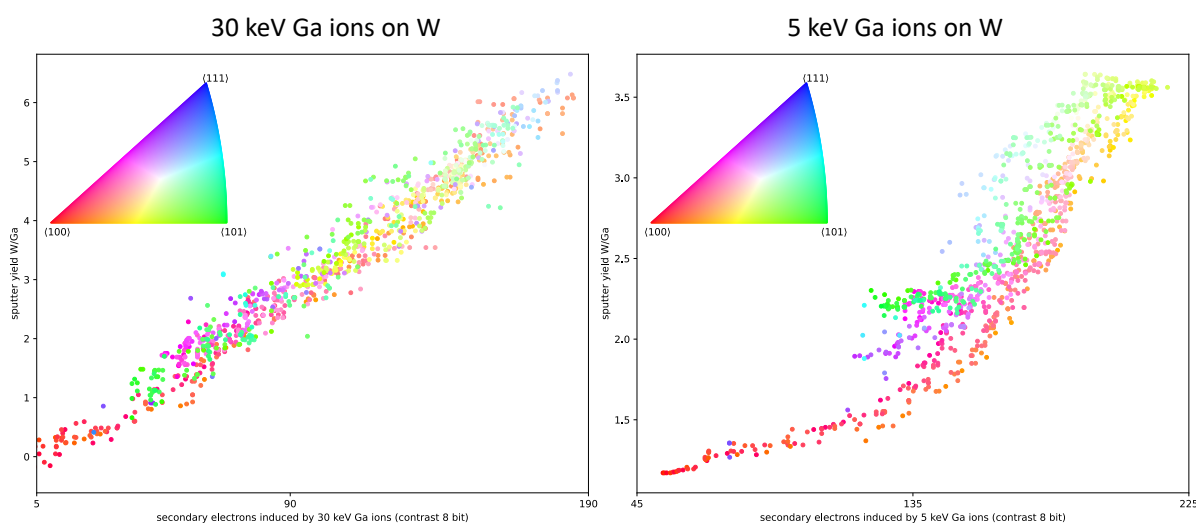
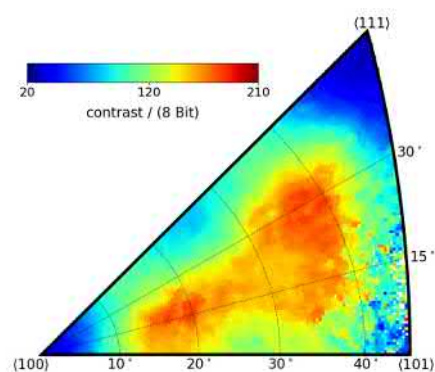
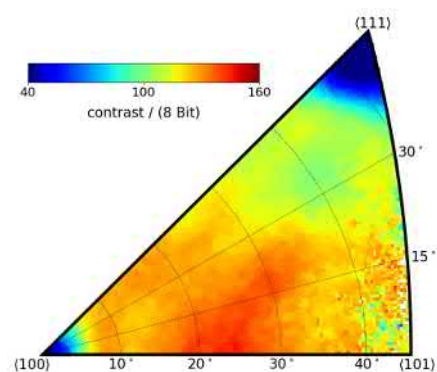


Figure 5.13: Correlation between SE intensity and sputter yield for 30 keV and 5 keV Ga ion energy on W: The crystal orientation data points inside the tungsten sputter yield IPF (see figure 5.6a and 5.8a) and SE intensity IPF (see 30 keV and 5 keV IPF in figure 5.2a) are correlated with color representing their grain orientation. Please note that crystal texture did not allow sufficient representation of grain orientations close to the (111) corner.

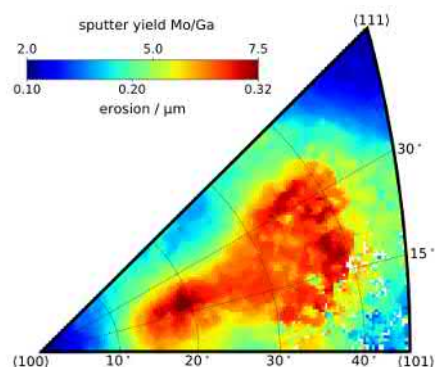
The 30 keV Ga ion energy molybdenum SE intensity IPF and sputter yield IPF in figure 5.14 also display matching results. The maxima and minima are similar in shape and intensity. For a Ga ion beam energy of 5 keV, the SE intensity IPF strongly differs from the sputter yield IPF for molybdenum. One factor for this unexpected behavior might be the previously described but unexplained inversion phenomenon for molybdenum.



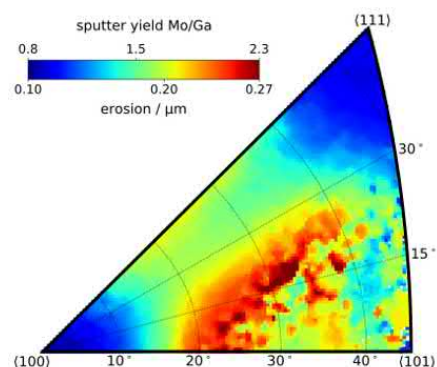
(a) Mo SE intensity IPF with 30 keV Ga ions (from figure 5.2b)



(b) Mo SE intensity IPF with 5 keV Ga ions (from figure 5.2b)



(c) Mo sputter yield IPF with 30 keV Ga ions (see figure 5.7a)



(d) Mo sputter yield IPF with 5 keV Ga ions (see figure 5.9a)

Figure 5.14: Comparison of SE intensity IPF and sputter yield IPF for molybdenum sputtering with a 5 keV and 30 keV Ga ion beam

Figure 5.15 displays a linear correlation for 30 keV molybdenum sputtering between sputter yield and SE intensity. For 5 keV Ga ion energy, the data points show a distinct bend. Sputter yield seems to increase rapidly at higher intensity with some intensity values representing multiple sputter yields.

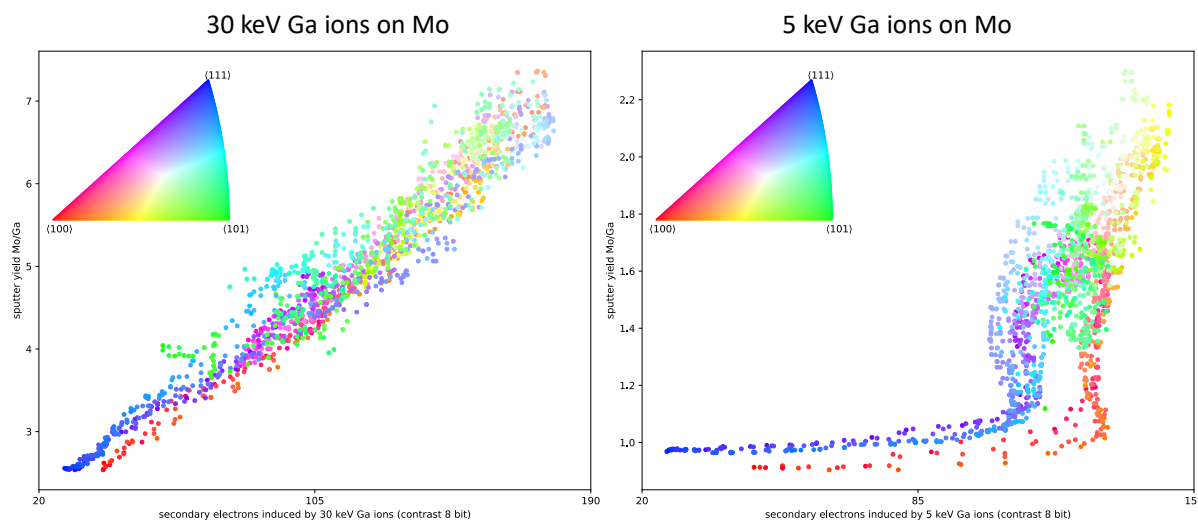


Figure 5.15: Correlation between SE intensity and sputter yield for 30 keV and 5 keV Ga ion energy on Mo: The crystal orientation data points inside the molybdenum sputter yield IPF (see figure 5.7a and 5.9a) and SE intensity IPF (see 30 keV and 5 keV IPF in figure 5.2b) are correlated with color representing their grain orientation. Please note the observed inversion phenomenon of low energy molybdenum measurements described in section 5.1.1

Overall, the bcc metals tungsten and molybdenum display reliable linear correlation of sputter yield and SE intensity for a Ga ion energy of 30 keV. Grain orientation does not significantly influence the linear distribution of datapoints. For a Ga ion energy of 5 keV, the linear correlation is not robust for tungsten and molybdenum results indicate no linear correlation between sputter yield and SE intensity, which might be due the unexplained inversion phenomenon described in section 5.1.1.

5.2 Face Centered Cubic Metals

5.2.1 SE Intensity of fcc Metals

The results of the fcc SE intensity energy series are displayed in figure 5.16. The maxima in the SE intensity IPF for copper and platinum align for 30 keV and 16 keV Ga ion energy. A less distinct minimum is visible in the left (100) and right (101) corner while one localized maximum is in the top (111) corner and one triangularly shaped between the top (111) and left (100) corner. For lower energy beams, the maxima for copper gradually widened with the triangular one becoming circular in shape and slightly shifting towards the left (100) corner. Platinum behaves differently as the maxima flatten almost completely. It could be suspected that also for Pt an unresolved effect changes the SE emission efficiency at lower energies. Again, like for the lowest Ga ion impact energies on molybdenum, Ga deposition may play a role. The triangular maximum for platinum slowly shifts towards the bottom edge in the 5 keV SE intensity IPF and accumulates in the left (100) corner at 2 keV Ga ion energy. Both metals display a distinct minimum in the right (101) corner for all investigated energies. Conclusively, SE intensity IPF for platinum may not be trustful below 16 keV.

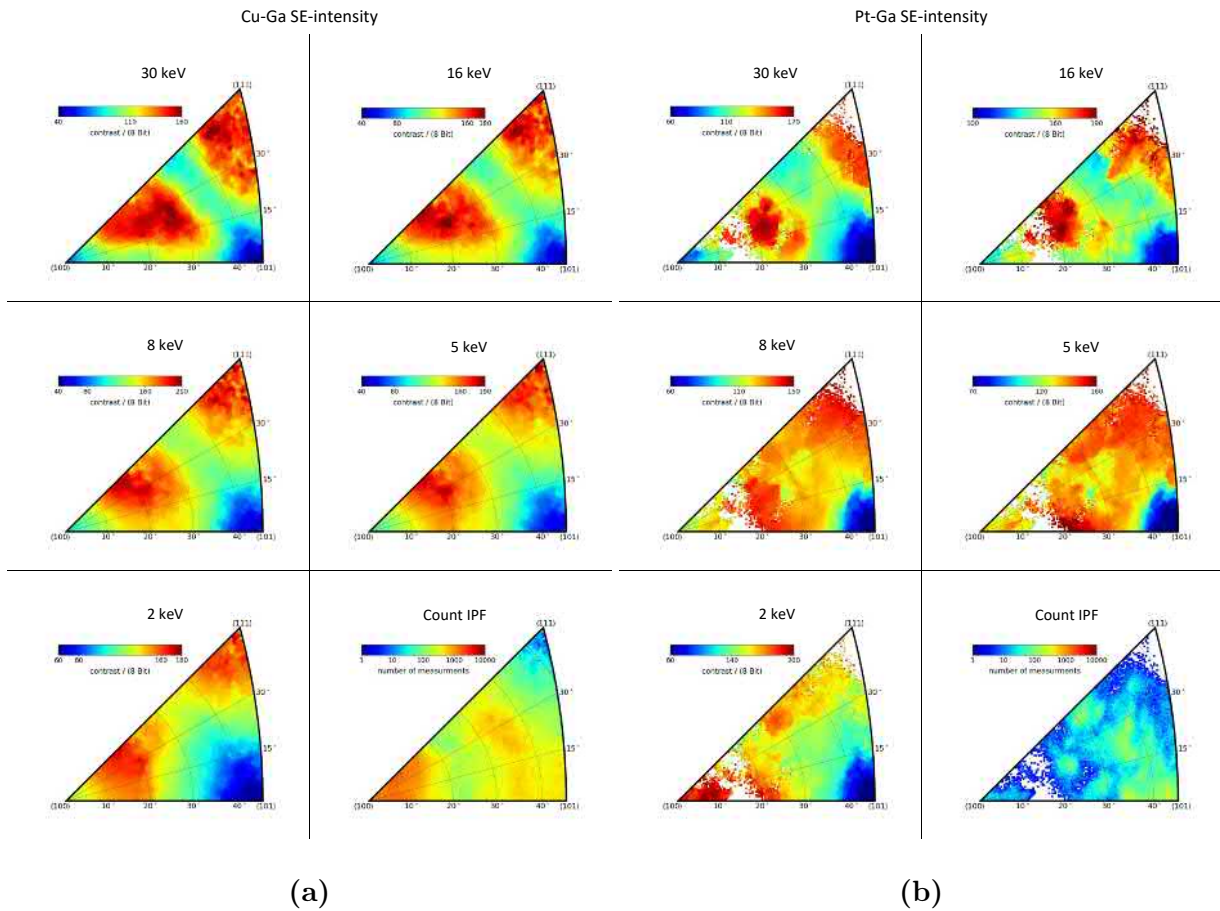


Figure 5.16: SE intensity energy series IPF for copper (a) and platinum (b): The count IPF in the bottom right corner is same for all measurements as images were taken from the same area. Platinum results were corrected with a second order linear fit. The unprocessed SE intensity IPF for platinum and all SD IPF are listed in appendix A.4.2

Copper displays small spatially uniformly distributed grains. The individual grains are distorted and thus contain more than one single orientation. The count IPF in figure 5.17b is covered with more data points in the left (100) corner. Copper thus displays a texture. The SD IPF in figure 5.17c shows that the standard deviation is higher at maxima and minima locations.

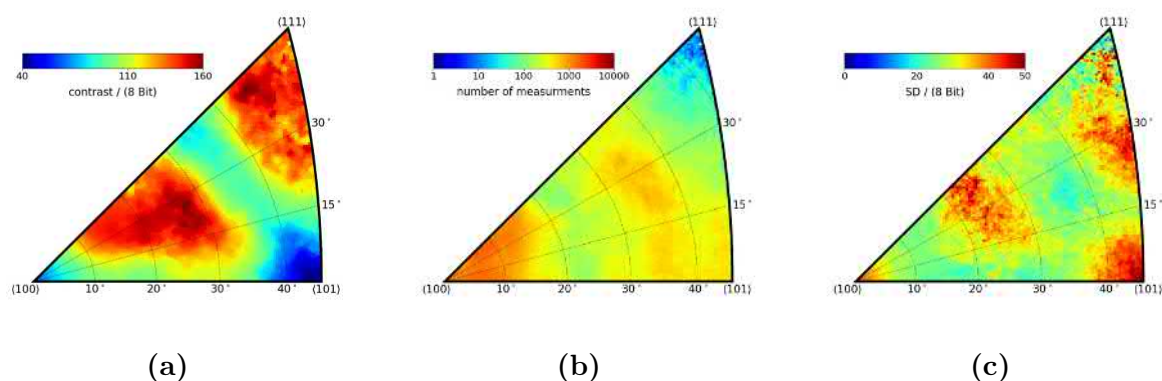


Figure 5.17: Cu 30 keV Ga ion energy SE intensity IPF (a), count IPF (b) and SD IPF (c): This plot is a magnified figure from the SE intensity energy series of Cu (see figure 5.16a)

The platinum specimen almost exclusively contains large grains as described in the specimens section 4.2. The grains display few distortions and are well-defined. This is represented by slightly outstretched patches in the count IPF in figure 5.18b. Grain orientations in the left (100) and top (111) corner are less present in the count IPF as those grains were not present in the selected sputter area inside the markers. Standard deviation is low across the SD IPF in figure 5.18c.

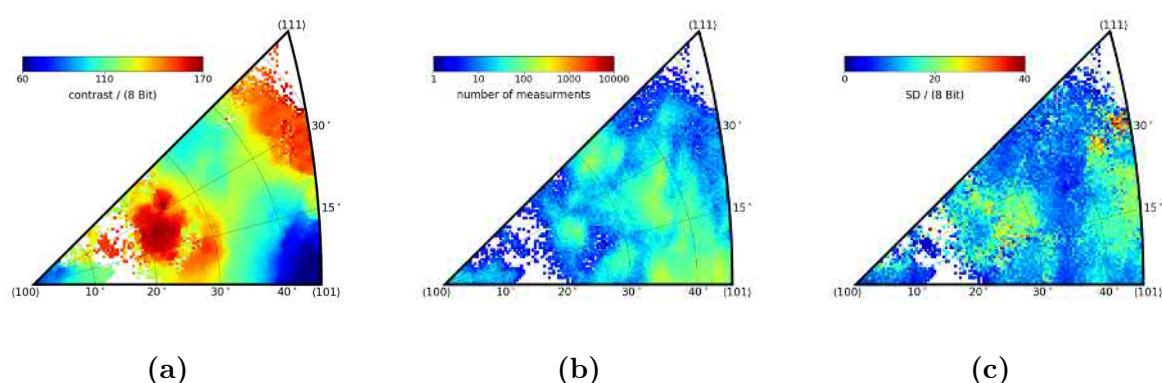


Figure 5.18: Pt 30 keV Ga ion energy SE intensity IPF (a), count IPF (b) and SD IPF (c): This plot is a magnified figure from the SE intensity energy series of Pt (see figure 5.16b)

The platinum intensity images taken by the FIB display a visible diagonal shading (see figure 5.19). This shading was previously discussed in the data workflow section 4.5.4. Low magnification was needed for platinum to capture the FIB images of a wide area in order to include as many grains as possible by the SEM. The detector is physically located close

to the brighter area and thus may have detected a higher number of secondary electrons. In addition to this, the specimen surface was not perfectly flat due to the overall small size of the sample and hence the more difficult sample preparation. A spherical surface warp is visible in figure 5.20. Please note, obtaining reliable data from such a warped surface requires difference microscopy (see section 4.5.3).

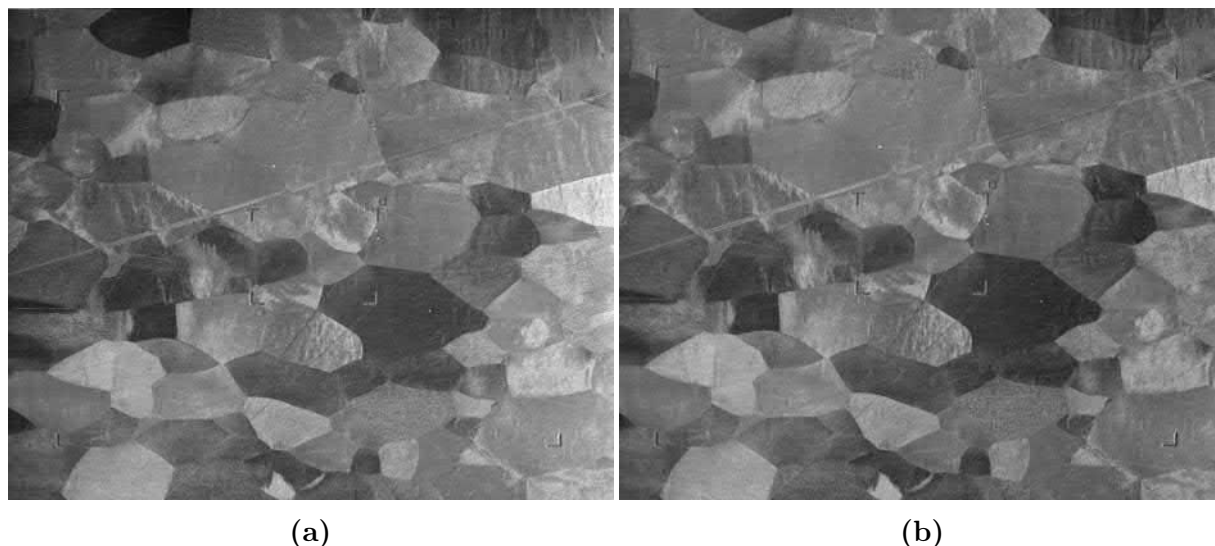


Figure 5.19: SE intensity image of platinum before (a) and after (b) quadratic shading correction

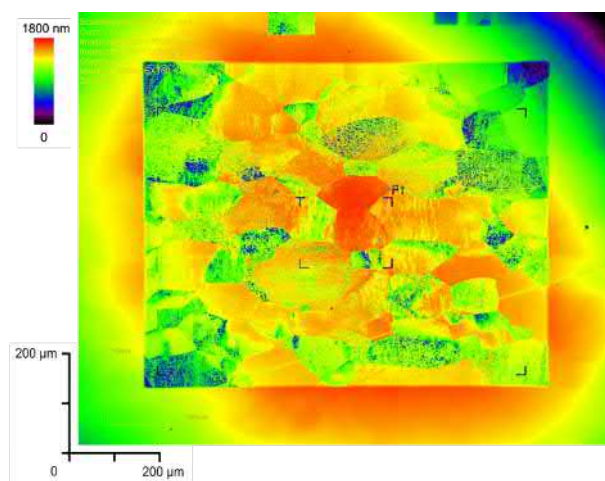


Figure 5.20: CLSM image of platinum specimen: The spherical warp of the sample spans about 1 μm.

A paraboloid surface was first fitted to and then subtracted from the intensity data with the help of the shading correction python tool (see appendix A.1 for a more detailed explanation). A quadratic fit like a paraboloid was preferred compared to a linear fit like a plane as the electric field for secondary electron detection is inversely correlated to the squared distance from the detector. Additionally, polishing morphology was mainly of second degree. Higher degree fitting bears the risk to overfitting without sufficient reason and hence can alter the measurement significantly. Especially low number of randomly oriented grains inside the marked area increase the risk of overfitting. The resulting subtraction paraboloid was consistent for all energy levels as shown in figure 5.21.

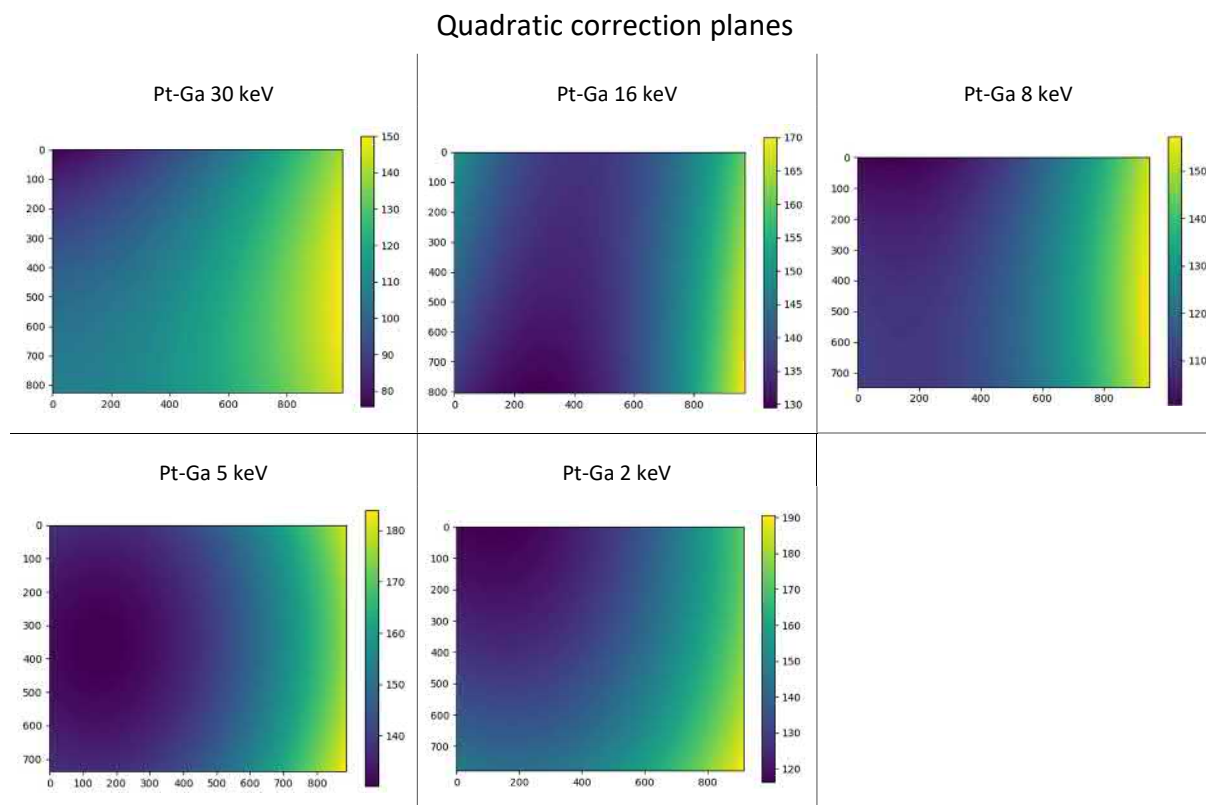


Figure 5.21: Shading correction paraboloids for each energy in the platinum SE intensity energy series (see figure 5.16b): The pixel in the x-y-plane are assigned the 8 Bit contrast value of the fitted surface.

Shading is likely to occur in all SEM images under the presented reasoning. Higher magnification makes this effect negligible compared to the intensity variation due to grain orientation, as the central area inside the fitted paraboloids in figure 5.21 display nearly no gradient.

5.2.2 Sputter Yield of fcc Metals

The copper results do not utilize difference microscopy as only one quadrant inside the marked area needed to be sputtered to obtain sufficiently distributed data in the IPF due to small grain size and distorted grains. As seen in figure 5.22, precise locations could not be determined in the CLSM data before and after the experiment but are critical to accurately subtract the height data. Better marker placement would have allowed the use of difference microscopy. Single CLSM data merge is heavily dependent on a flat surface before sputtering and thus sample preparation is critical. Some grain orientations might be more likely to wear off during sample polishing and those leave depressions which affect the calculated erosion and therefore the calculated sputter yield.

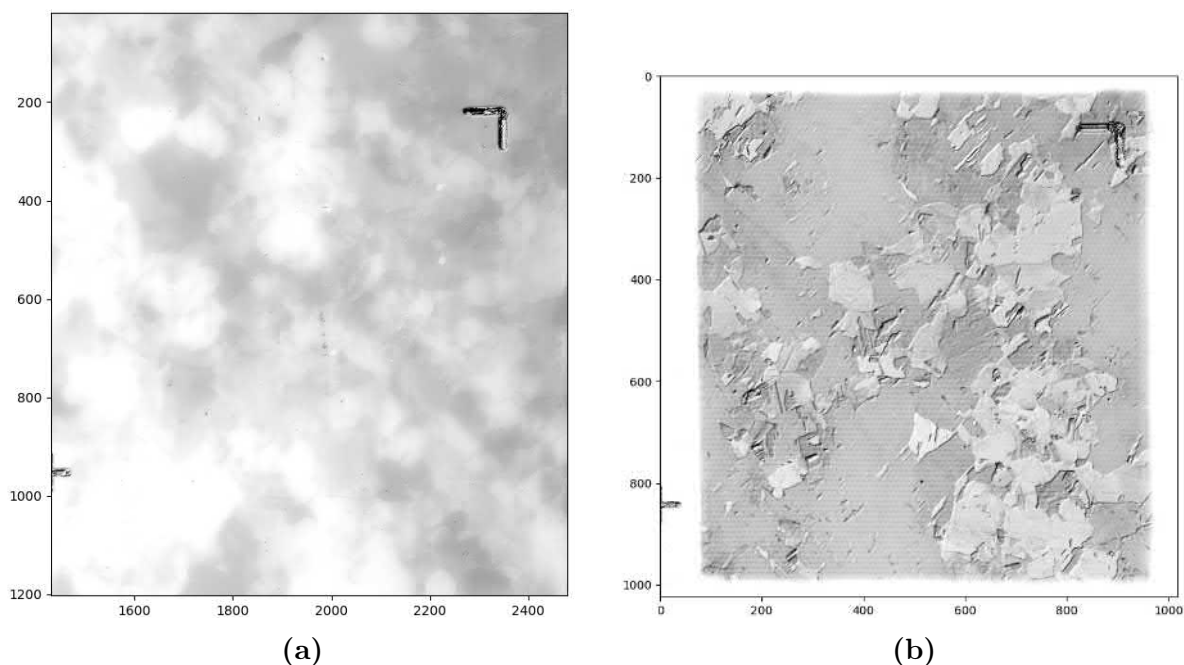


Figure 5.22: Cu CLSM height data before (a) and after (b) sputtering: Difference microscopy requires the selection of 4 identical points inside both plots. The missing markers did not allow reliable selection of these points and thus difference microscopy could not be utilized for copper sputtering.

The 30 keV Ga ion energy sputter yield IPF for copper in figure 5.23a displays one minimum at the left (100) corner and a broader one at the right (101) corner. The top (111) corner indicates one maximum, which is warped towards the right (101) corner, and another triangular shaped maximum between the left (100) and top (111) corner. Both show a gradual decrease in all directions with jagged boundaries. The platinum sample in figure 5.24a shows a matching minimum in the right (101) corner with outlines for two maxima placed at similar positions compared to copper inside the sputter yield IPF. Unfortunately, data points at the expected maxima locations are missing.

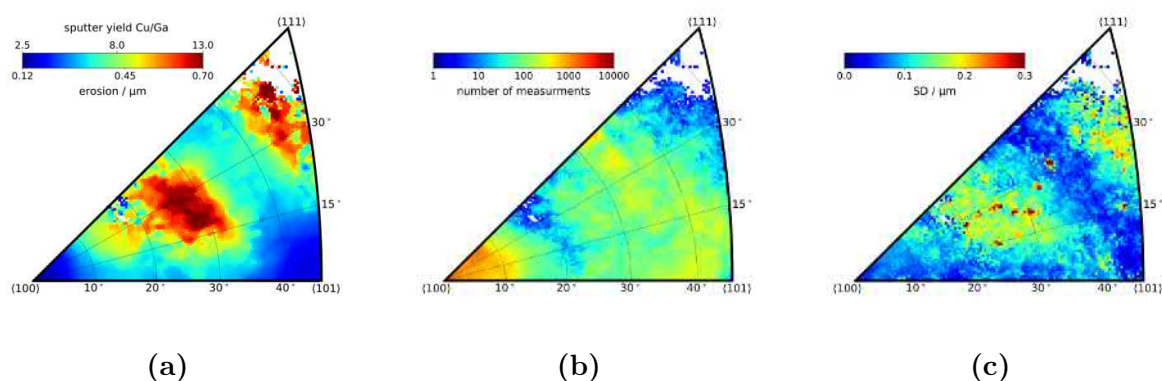


Figure 5.23: Cu 30 keV Ga ion energy sputter yield IPF (a), count IPF (b) and SD IPF (c)

The 30 keV count IPF for platinum in figure 5.24b is not fully covered. The available space on the platinum sample is very limited and the selected FIB marker region, unfortunately, did not contain many grains with orientations near the left (100) and top (111) corner. Individual grain size is big as described in section 4.2, so even with the greatest possible area covered, some grain orientations could not be captured. This wide sputtering area increases the sputtering to well over 30 hours. Sputter erosion experiments could be conducted on multiple marked positions if the available area on the sample would be sufficient and the datasets could be combined to measure the missing data points in the count IPF. This measurement would require several days of sputtering time.

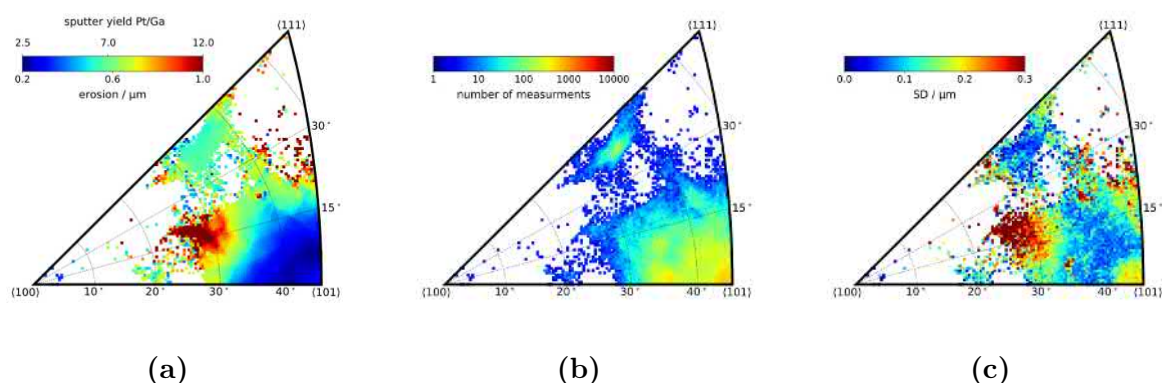


Figure 5.24: Pt 30 keV Ga ion energy sputter yield IPF (a), count IPF (b) and SD IPF (c)

For a Ga ion energy of 5 keV, copper displays one wide minimum in the right (101) corner inside the sputter yield IPF in figure 5.25a with one smaller and lower intensity minimum in the left (100) corner. One maximum is located in the top (111) corner with a second lower intensity one close to the diagonal edge between the left (100) and top (111) corner along the 20° arc. Both maxima are connected with a higher yield area along the diagonal with gradual decrease in all directions and jagged boundary.

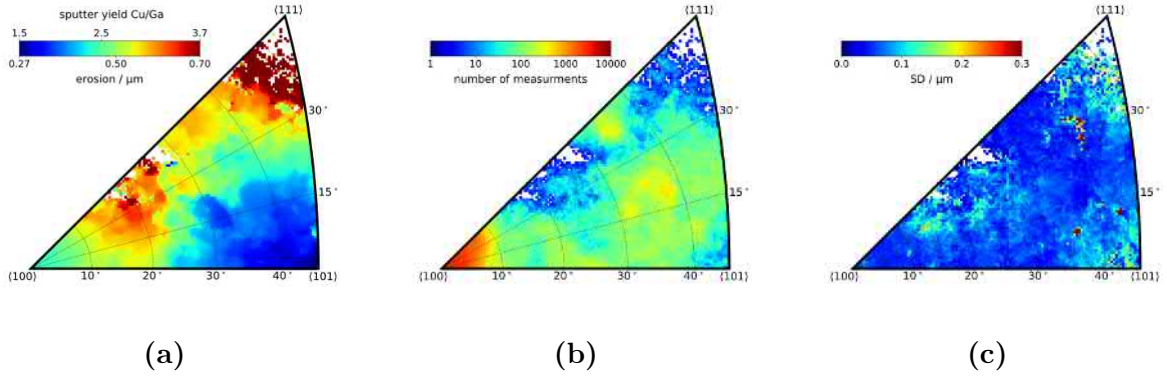


Figure 5.25: Cu 5 keV Ga ion energy sputter yield IPF (a), count IPF (b) and SD IPF (c)

The 5 keV Ga ion energy sputter yield IPF for platinum in figure 5.26a shows smooth gradients with one distinct broad minimum in the right (101) corner and one circular and slightly to the bottom distorted maximum at the diagonal edge along the 20° arc. A smaller lower intensity minimum is located at the left (100) corner. The position of these maxima and minima match the location of the copper extrema with the exception of the maximum in the top (111) corner. The selected platinum region inside the markers did not contain enough grains with orientations close to the top (111) corner.

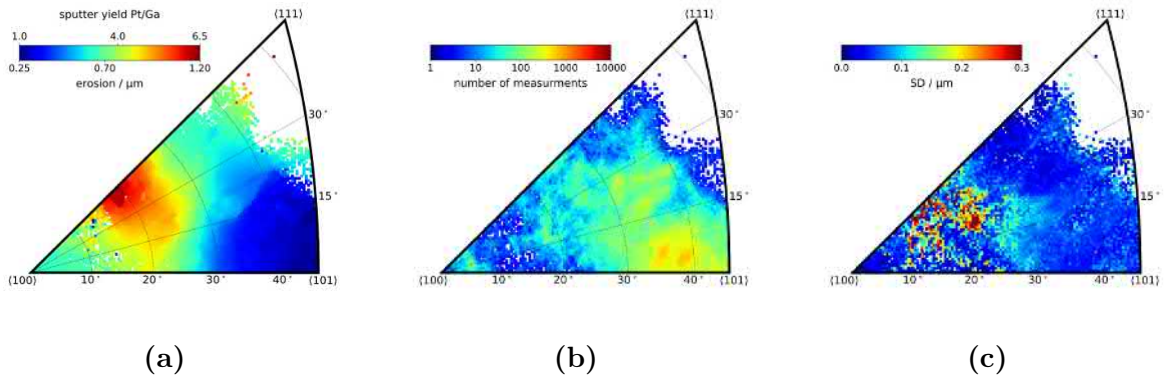


Figure 5.26: Pt 5 keV Ga ion energy sputter yield IPF (a), count IPF (b) and SD IPF (c)

Sputter yield data obtained in this thesis are compared with measurement data obtained from 50 year old literature [24]. Figure 5.27 displays the sputter yield of different fcc metals along the edge between the (100) and (111) corner in an IPF for Pt, Cu from figures 5.24a and 5.23a together with rotation of single-crystalline Pb, Au, Cu, Al, which represent crystallographic equivalent orientations. Please note that 20 keV Ar ions were used to generate the single-crystal data points [24]. The regression curve of Pt could not be determined below 29° because of insufficient data points due to the previously described lack of grain orientations inside the marked area (see section 4.2). The regression curve of Cu displays similar extrema locations when compared to the single-crystal regression curves. This similarity provides one confirmation to the second central question that grain dependent sputtering displays similarities for same crystal structure.

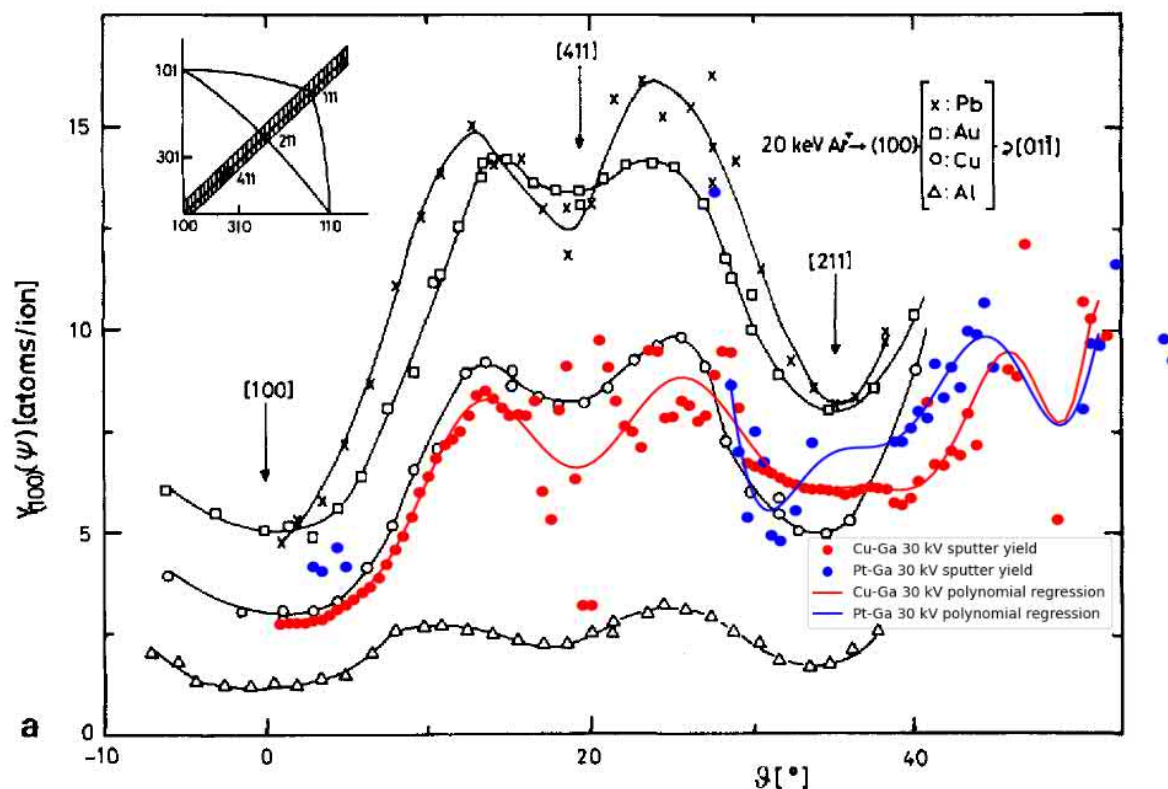
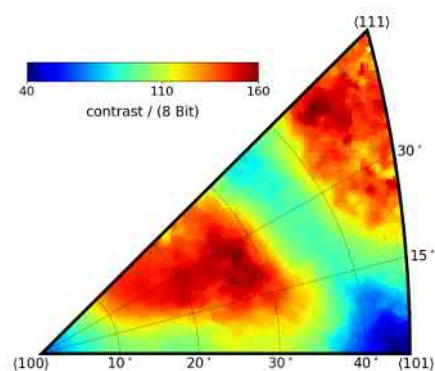


Figure 5.27: Linescan sputter yield of 30 keV Ga ion energy of Pt and Cu overlaid on data generated with rotation of single-crystals and 20 keV argon ion energy [24]: The polynomial regression curves of Pt and Cu are 15th order fits to the data points.

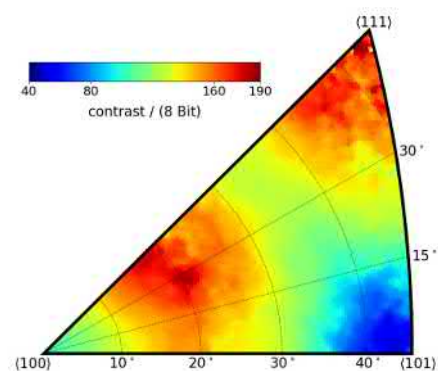
This similarity is visible even though argon ions with an energy of 20 keV were used to generate the single-crystal data. Tungsten sputter yield IPF with 30 keV and 16 keV Ga ion energy displayed almost identical positions of extrema in SCHLÜTERS work [4]. The fcc and bcc SE intensity energy series IPF in figure 5.16 and figure 5.2 back the assumption that qualitative distribution of maxima and minima inside the IPF does not vary significantly between 16 keV and 30 keV. Conducted sputter experiments with argon and neon ions of the same energy as projectiles displayed qualitatively similar angular sputter yield distribution of the single-crystal copper target [24]. The similar regression curve of the measurement conducted with Ga ions indicates that the position and distribution of extrema of sputter yield inside an IPF might be independent of ion type in the 'Linear-Cascade-Regime' and for equivalent projectile particle to target particle mass ratio. The targets of the argon ion beam have higher atomic number by a factor of 1.6 to 4.5 and the targets of the Ga ion beam display a 2.5 times higher atomic number in the case of Pt and close to optimal energy transfer is achieved in the case of Cu due to the nearly same atomic mass as Ga as stated in section 3.2. Additionally, single-crystal targets display similar sputter yield maxima and minima locations when rotated compared to polycrystalline targets containing individual differently oriented grains. Linescan plots (see figure 5.27) for fcc and bcc metals are provided in appendix A.4.3.

5.2.3 Comparison of fcc Sputter Yield and SE Intensity

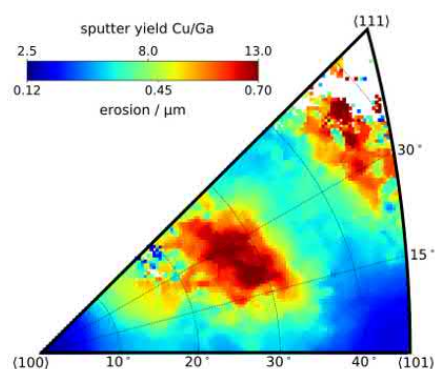
The 30 keV Ga ion energy copper SE intensity IPF and sputter yield IPF show matching results in figure 5.28a and 5.28c. The position and intensity of extrema align in both IPF. The triangular middle maximum and the top maximum warped towards the right (101) corner is clearly visible. The 5 keV Ga ion energy copper SE intensity IPF and sputter yield IPF differ from each other in figure 5.28b and 5.28d. The locations of extrema are similar. The minimum in the right (101) corner is smaller in the intensity IPF whereas the minimum in the sputter yield IPF covers almost one third of the plot. The decline from maxima is smoother in the intensity IPF and there is a less pronounced link between the two maxima, which is clearly visible in the 5 keV sputter yield IPF for copper. These irregularities might be due to the use of single CLSM data merging and resulting errors described in section 4.5.3 and 5.2.2.



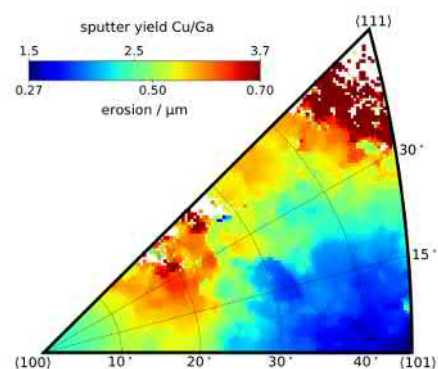
(a) Cu SE intensity IPF with 30 keV Ga ions (from figure 5.16a)



(b) Cu SE intensity IPF with 5 keV Ga ions (from figure 5.16a)



(c) Cu sputter yield IPF with 30 keV Ga ions (see figure 5.23a)



(d) Cu sputter yield IPF with 5 keV Ga ions (see figure 5.25a)

Figure 5.28: Comparison of SE intensity IPF and sputter yield IPF for copper sputtering with a 5 keV and 30 keV Ga ion beam

Plotting the sputter yield versus the SE intensity for copper shown in figure 5.29 may indicate a linear correlation for 30 keV Ga ion energy but sputter yield varies by a factor of 2.5 for higher intensity values in the right half of the plot. The 5 keV correlation plot shows a larger deviation from a linear trend, especially at higher intensity values where sputter yield varies by a total factor of 2 from lowest to highest data point in the right half.

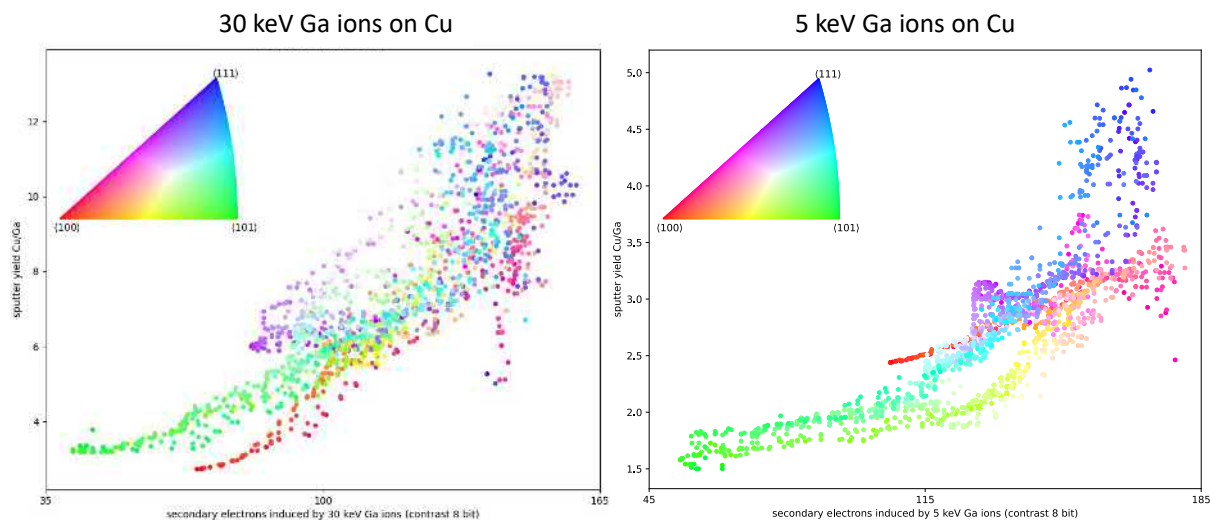
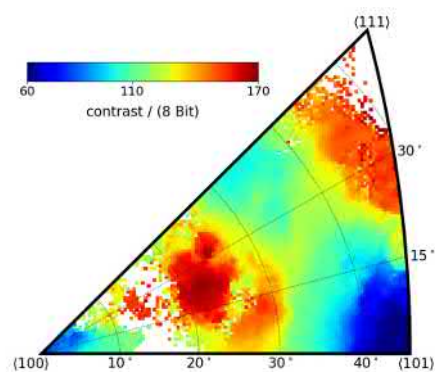
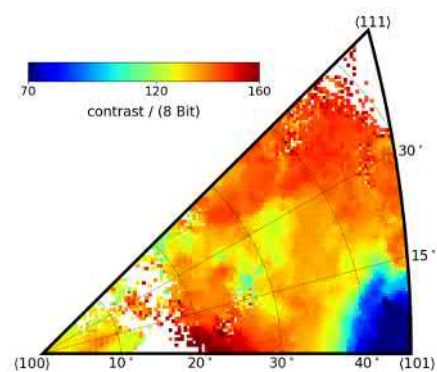


Figure 5.29: Correlation between SE intensity and sputter yield for 30 keV and 5 keV Ga ion energy on Cu: The crystal orientation data points inside the Cu sputter yield IPF (see figure 5.23a and 5.25a) and SE intensity IPF (see 30 keV and 5 keV IPF in figure 5.16a) are correlated with color representing their grain orientation. Please note the absence of difference microscopy for sputter yield measurement.

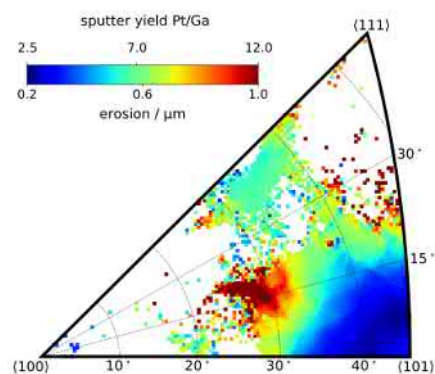
For a Ga ion energy of 30 keV on platinum, the SE intensity IPF and sputter yield IPF in figure 5.30a and figure 5.30c show similar results. The sputter yield IPF only contains limited information for exact location and magnitude of extrema but the general locations match for the measured data points. The minimum in the sputter yield IPF appears slightly broader. The 5 keV Ga ion energy SE intensity IPF and sputter yield IPF for platinum in figure 5.30b and figure 5.30d display significant differences. Only the general location of the minimum in the right (101) corner matches. The minimum itself is sharper in the SE intensity IPF. The maximum in the sputter yield IPF is circular and localized on the diagonal edge between the (100) and (111) corner. Ga ion deposition might be on possible cause for the unclear localization of the maximum in the SE intensity IPF.



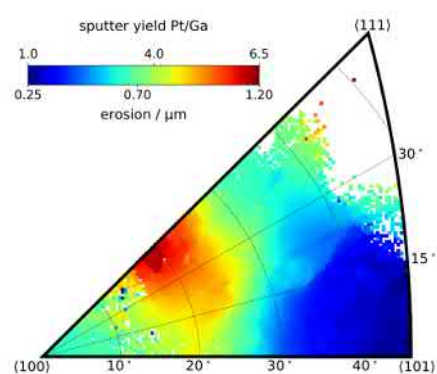
(a) Pt SE intensity IPF with 30 keV Ga ions (from figure 5.16b)



(b) Pt SE intensity IPF with 5 keV Ga ions (from figure 5.16b)



(c) Pt sputter yield IPF with 30 keV Ga ions (see figure 5.24a)



(d) Pt sputter yield IPF with 5 keV Ga ions (see figure 5.26a)

Figure 5.30: Comparison of SE intensity IPF and sputter yield IPF for platinum sputtering with a 5 keV and 30 keV Ga ion beam

For 30 keV Ga ion energy, figure 5.31 might indicate a linear trend between sputter yield and SE intensity for lower intensity values but the data points display no correlation for higher intensity values. For 5 keV Ga ion energy, the sputter yield trend shows a slow linear increase for intensity values below 110 with a sharp incline at higher intensity. Intensity values in the right half may also display multiple sputter yields.

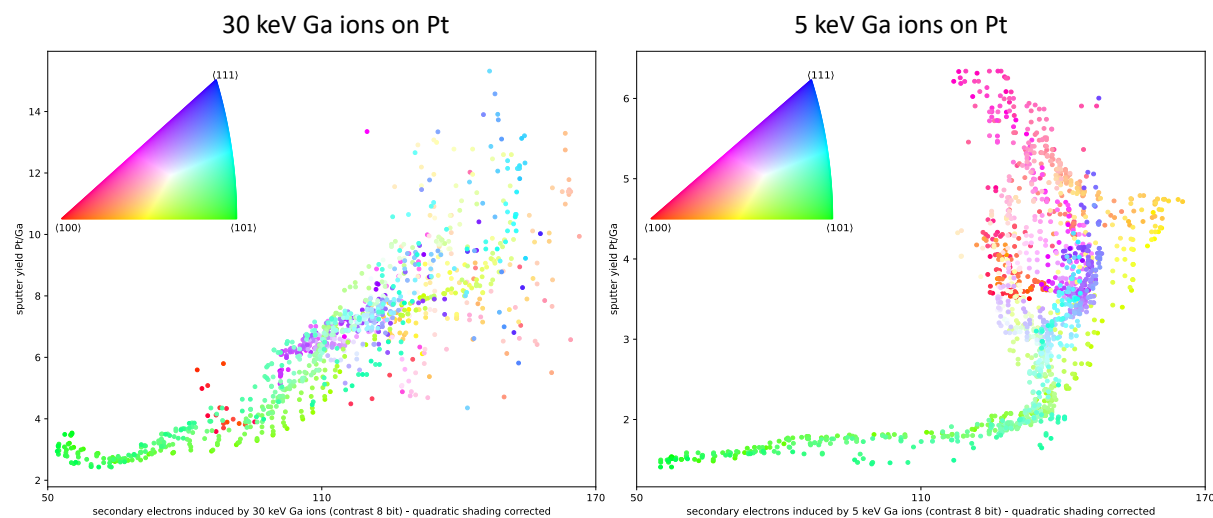


Figure 5.31: Correlation between SE intensity and sputter yield for 30 keV and 5 keV Ga ion energy on Pt: The crystal orientation data points inside the Pt sputter yield IPF (see figure 5.24a and 5.26a) and SE intensity IPF (see 30 keV and 5 keV IPF in figure 5.16b) are correlated with color representing their grain orientation. Please note the absence of grain orientations close to the (100) and (111) corner in the 30 keV IPF and close to the (111) corner in the 5 keV IPF, together with the presence of the platinum SE intensity shading described in section 4.5.4 and 5.2.1. The correlation plot without quadratic shading correction can be found in appendix A.4.2. The unprocessed dataset did not display a robust linear correlation.

The fcc metals copper and platinum do not display robust linear correlation of sputter yield and SE intensity for a Ga ion energy of 30 keV even though similar distribution of extrema inside the respective IPF suggest the contrary. Consequently, absolute sputter yield values cannot be deduced from SE intensity IPFs. The sputter yield varies up to a factor of 2 for higher intensity values. For a Ga ion energy of 5 keV, the linear correlation is not robust for copper at higher intensity values and platinum results indicate no linear correlation between sputter yield and SE intensity, which disproves the first central question. The platinum measurements influenced by the large grains shown in section 4.2 and SE intensity shading described in section 4.5.4 and section 5.2.1. The copper measurements could not utilize difference microscopy as elaborated in section 4.5.3 and 5.2.2.

Chapter 6

Conclusion and Outlook

The first central question asked if SE emission has a linear correlation to sputter yield. This linear correlation implies visually identical sputter yield IPF and SE intensity IPF. Great resemblance in SE intensity IPF is present for higher energies as described in sections 5.1.1 and 5.2.1. All four investigated metals show matching locations for extrema and similar gradients around them for 30 keV Ga ion energy. Brighter grains in the intensity images thus represent higher sputter yield. The linear correlation between sputter yield and SE intensity is only robust for the bcc metals tungsten and molybdenum for a Ga ion beam energy of 30 keV as investigated in section 5.1.3. Copper and platinum do not display reliable linear correlation across all intensity values even though locations and gradients of maxima and minima inside the respective IPF seem to match.

Investigations at lower energies show mixed results. While copper and tungsten SE intensity IPFs and sputter yield IPFs with 5 keV Ga ions show similarities with matching shape of extrema, the SE intensity and sputter yield IPFs for platinum and for molybdenum display significant deviation from each other. A linear correlation between sputter yield and SE intensity is not present as described in sections 5.1.3 and 5.2.3. Ga ion deposition might be one cause for the altered SE intensity IPF appearances. The SE energy series for molybdenum and platinum display a continuous transition from reliable high-energy plots to uncorrelated low-energy plots with its tipping point at an energy range around 8 keV. Further research on these deviations needs to be conducted to investigate the correlation of sputter yield and SE emission efficiency at lower ion beam energies.

The linear correlation implied from the first central question is not robust for all conducted measurements. SE intensity IPF generated with higher Ga impact energy thus only allow localization and rough approximation of sputter yield maxima and minima in an IPF. Lower Ga ion energies of 5 keV do not allow to draw conclusions on grain dependent sputter yield of a material. A higher amount of discrete energy steps with even higher ion beam energy in the SE energy series would create a broader understanding of SE emission efficiency. Such a refined SE energy series of the 'Linear-Cascade-Regime' may also give insight on the energy range, for which a linear correlation between sputter yield and SE intensity can be assumed and where it deviates. A possibly robust linear correlation across several investigated materials allows the extrapolation that other metals or material choices may also be characterized with SE intensity to quickly generate an estimate sputter yield IPF. Exact sputter yield than may only need to be measured for one energy and absolute data can be merged with the qualitative SE intensity IPF for rapid material classification. This may even allow extrapolation to grain dependent sputtering across a nearby energy range.

The second central question asked if the same lattice structures display nearly equal sputtering behavior. This question turns out to be true for body centered cubic metals under the given data as both molybdenum and tungsten samples showed the same erosion distribution. The location of maxima and minima in the IPF match for both 5 keV and 30 keV for the two metals.

Face centered cubic metals show promising results but still miss reliable data to draw conclusions at the moment. Unfortunately, the copper results may include polishing errors and the marked platinum areas did not contain enough grain orientations. Nevertheless, the locations of the extrema seem to match or indicate matching results for fcc metals. Better marker placement on the copper sample and additional sputter yield experiments on different locations on the platinum sample need to be performed. Additional verification of the measured sputter yield data was given through the comparison with sputter yield distribution of rotated single-crystals.

If the second central question turns out to be true, sputtering is mainly dependent on lattice structure and grain dependent sputtering of other metals can be classified by their crystal structure. In this case, metals of the hcp crystal lattice structure are expected to display respectively similar grain dependent sputtering behavior. Additionally, material-specific properties would then define the quantitative values inside a possibly generalized sputter yield IPF for one cubic crystal lattice structure. Further investigation may be performed with other relevant bcc and fcc metals, especially Fe, to confirm this question.

The data acquired in this thesis broadens the understanding of different metal behavior under ion beam exposure and the workflow for experimental grain dependent property analysis was described. The possibly greatly increased classification speed with SE emission efficiency for higher energy of the Ga ions may eventually lead to rapid data generation for grain dependent sputtering on polycrystalline targets. Material selection and manufacturing may also be altered due to these results. One possible outlook is preferred grain orientation relative to the most probable ion impact angle on the divertor, which may be achieved through different manufacturing methods. This could further decrease plasma contamination and increase the component lifetime. Another outlook might be to use a strongly textured sputter cathode for deposition, ground in direction of a sputter yield maximum.

Particularly, simulations of sputtering need experimental datasets for reference and validation. This validation was performed with tungsten measurements [5] and first simulations for copper [25] already display matching results (as depicted in appendix A.4).

Bibliography

- [1] P. Martin, *Review of Ion-based methods for optical thin film deposition*. J. Mat. Sci., 21, pages 1-25, 1986.
- [2] S. Mahieu J.E. Greene, D. Depla. *Handbook of Deposition Technologies for Films and Coatings (Third Edition)*, chapter 5. William Andrew Publishing, Oxford, 3 edition, 2010.
- [3] H. E. Roosendaal. *Sputtering Yields of Single Crystalline Targets*. In *Sputtering by particle bombardment I*, pages 219–256. Springer, 1981.
- [4] K. Schlüter. *Tungsten Properties Correlated with the Orientation of its Crystals*. PhD thesis, Technical University Munich, 2021.
- [5] K. Schlueter, K. Nordlund, G. Hobler, M. Balden, F. Granberg, O. Flinck, T. F. da Silva, and R. Neu. *Absence of a Crystal Direction Regime in which Sputtering Corresponds to Amorphous Material*. Phys. Rev. Lett., 125:225502, Nov 2020. doi: 10.1103/PhysRevLett.125.225502. URL <https://link.aps.org/doi/10.1103/PhysRevLett.125.225502>.
- [6] W. Heiland E. Taglauer. *Inelastic Particle-Surface Collisions*. Springer, 1980.
- [7] K. Nordlund. *Molecular dynamics simulation of ion ranges in the 1-100 keV energy range*. Computational Materials Science, 3(4):448–456, 1995. ISSN 0927-0256. doi: [https://doi.org/10.1016/0927-0256\(94\)00085-Q](https://doi.org/10.1016/0927-0256(94)00085-Q). URL <https://www.sciencedirect.com/science/article/pii/092702569400085Q>.
- [8] E. Marenkov, K. Nordlund, I. Sorokin, A. Eksaeva, K. Gutorov, J. Jussila, F. Granberg, and D. Borodin. *Angular and velocity distributions of tungsten sputtered by low energy argon ions*. Journal of Nuclear Materials, 496:18–23, 2017.
- [9] K. Nordlund. *Atomistic simulations of plasma-wall interactions in fusion reactors*. Physica Scripta T, T124:53–57, 2006.
- [10] K. G. Schmitt-Thomas. *Metallkunde für das Maschinenwesen*. Springer, Berlin, Heidelberg, 2 edition, 1988.
- [11] R. Behrisch. *Introduction and Overview*. In *Sputtering by particle bombardment I*, pages 2–4. Springer, 1981.
- [12] G. Franz. *Niederdruckplasmen und Mikrostrukturtechnik*. Springer, Berlin, Heidelberg, 3 edition, 2004.
- [13] A. Khursheed. *Scanning Electron Microscope Optics and Spectrometers*. World Scientific Publishing, 2011.

-
- [14] M. Gu. *Principles of Three-Dimensional Imaging in Confocal Microscopes*. World Scientific Publishing, London, 1996.
- [15] H. Briehl. *Chemie der Werkstoffe*. Springer, Berlin, Heidelberg, 4 edition, 2021.
- [16] Oxford Instruments NanoAnalysis. *Generating Orientation Maps to Present EBSD Data*, 2015. URL <https://www.azom.com/article.aspx?ArticleID=11775>. Last accessed 9 January 2021.
- [17] Sbyrnes321. *Crystalline polycrystalline amorphous*, 2011. URL https://commons.wikimedia.org/wiki/File:Crystalline_polycrystalline_amorphous.svg. Last accessed 9 January 2021.
- [18] M. T. Robinson. Theoretical aspects of monocrystal sputtering. In *Sputtering by particle bombardment I*, pages 74–144. Springer, 1981.
- [19] P. Sigmund. *Sputtering by Ion Bombardment: Theoretical Concepts*. In *Sputtering by particle bombardment I*, pages 9–71. Springer, 1981.
- [20] L. A. Giannuzzi et al. *Introduction to focused ion beams: instrumentation, theory, techniques and practice*. Springer Science and Business Media, 2004.
- [21] JEOL Ltd. *electron backscatter diffraction, EBSD*. URL https://www.jeol.co.jp/en/words/semterms/search_result.html?keyword=EBSD. Last accessed 10 January 2021.
- [22] P. Bauer. *Winkeldetektion des Ionenstrahls in der SIESTA*. Bachelor’s thesis, Hochschule für angewandte Wissenschaften, Landshut, 2020.
- [23] W. Eckstein R. Dohmen A. Mutzke, R. Schneider. *SDTrimSP version 5.00*. IPP Report 12/08, Max-Planck-Institut für Plasmaphysik (IPP) (2011).
- [24] D. Onderdelinden. *Single-crystal sputtering including the channeling phenomenon*. Canadian Journal of Physics, 46(6):739–745, 1968. doi: 10.1139/p68-091.
- [25] private communication from K. Nordlund, F. Kranberg et al., Department of Physics, P.O. Box 43, FIN-00014, University of Helsinki, Finland.

List of Figures

3.1	Schematic crystal structure of primitive cubic (a), body centered cubic (b), face centered cubic (c) and hexagonal close packed system (d) [10]	5
3.2	Unit cell with coordinate base and planes described with miller indices [10]	6
3.3	Construction of a pole figure [10]	6
3.4	Construction of an inverse pole figure: The colored triangle represents one of the 24 directionally equivalent areas for a cubic crystal lattice inside the pole figure. [16]	7
3.5	Crystalline (a), polycrystalline (b) and amorphous (c) structure [17]	7
3.6	Illustration of polycrystalline texture-free (a) and textured (b) surface [10]	8
3.7	Physical ion sputtering: R_p represents the projected range. [20]	9
3.8	General structure of a scanning electron microscope [13]	10
3.9	Principle of electron backscatter diffraction [21]	11
3.10	EBSD map for a polycrystalline recrystallized tungsten sample: The color encodes the detected Euler angles of the grain.	11
3.11	Images of the samples eroded by the FIB	12
3.12	Structure of a confocal laser scanning microscope [14] (a) and CLSM image of the Cu sample (b): The red surfaces mark elevated topology while blue surfaces show deeper sections relative to machine height-axis.	13
4.1	EBSD map (a) and CLSM image (b) of W specimen	16
4.2	EBSD map (a) and CLSM image (b) of Mo specimen: Please note the rectangular depression from FIB sputtering for sputter yield determination.	16
4.3	EBSD map (a) and CLSM image (b) of Cu specimen	17
4.4	EBSD map (a) and CLSM image (b) of Pt specimen	17
4.5	Picture of marker placement and experiment classification on platinum sample: The location for each specific experiment is marked.	18
4.6	Measurement workflow for IPF data generation: The upper blue path outlines the steps for SE intensity image generation. The lower orange path outlines the steps for obtaining sputter yield.	19
4.7	Workflow of EBSD, contrast and CLSM data with difference microscopy, filters and optimization	20

4.8	EBSD map before (a) and after (b) applying the noise filter: Spike errors visible in the yellow rectangle got discarded by the noise filter.	21
4.9	EBSD map before (a) and after (b) applying the grain boundary filter: The EBSD data was filtered with an exaggerated setting for illustrative purpose. Grains are clearly separated but even correctly classified datapoints were discarded.	22
4.10	Geometric levelling through a linear fitted plane	23
4.11	Example for visible contrast shade in SE intensity image of platinum . . .	24
4.12	Polar plot of minimum error optimization on incident beam angle: The color represents the mean standard deviation over the complete IPF plot at one applied rotation of the EBSD dataset. The minimum location indicates the most probable incident angle for the ion beam.	24
4.13	Data IPF (a), count IPF (b) and SD IPF (c) for W: A pixel inside the IPF equals about 1° , which is the expected accuracy achievable after data optimization. Pixels containing less than 3 data values were discarded with the cut-off filter.	25
5.1	SDTrimSP [23] sputter yield simulation results	27
5.2	SE intensity energy series IPF for the bcc metals tungsten (a) and molybdenum (b): The count IPF in bottom right corner is same for all measurement as images were taken from the same area. SD IPF are provided in appendix A.4.1	28
5.3	W 30 keV Ga ion energy SE intensity IPF (a), count IPF (b) and SD IPF (c): This plot is a magnified figure from the SE intensity energy series of W (see figure 5.2a)	29
5.4	Mo 30 keV Ga ion energy SE intensity IPF (a), count IPF (b) and SD IPF (c): This plot is a magnified figure from the SE intensity energy series of Mo (see figure 5.2b)	30
5.5	Molybdenum 2 keV Ga ion energy SE intensity IPF: This plot is a magnified figure from the SE intensity energy series of Mo (see figure 5.2b)	30
5.6	W 30 keV Ga ion energy sputter yield IPF (a), count IPF (b) and SD IPF (c)	31
5.7	Mo 30 keV Ga ion energy sputter yield IPF (a), count IPF (b) and SD IPF (c)	31
5.8	W 5 keV Ga ion energy sputter yield IPF (a), count IPF (b) and SD IPF (c)	32
5.9	Mo 5 keV Ga ion energy sputter yield IPF (a), count IPF (b) and SD IPF (c)	32
5.10	EBSD map of molybdenum sample before (a) and after (b) 5 keV Ga ion beam exposure: Please note the reduction of green and yellow pixels and thus grain orientations after (b) beam exposure.	33

5.11	Mo CLSM data merged with EBSD map generated before (a) and after (b) sputtering with 5 keV Ga ion beam	33
5.12	Comparison of SE intensity IPF and sputter yield IPF for tungsten sputtering with a 30 keV and 5 keV Ga ion beam	34
5.13	Correlation between SE intensity and sputter yield for 30 keV and 5 keV Ga ion energy on W: The crystal orientation data points inside the tungsten sputter yield IPF (see figure 5.6a and 5.8a) and SE intensity IPF (see 30 keV and 5 keV IPF in figure 5.2a) are correlated with color representing their grain orientation. Please note that crystal texture did not allow sufficient representation of grain orientations close to the (111) corner.	35
5.14	Comparison of SE intensity IPF and sputter yield IPF for molybdenum sputtering with a 5 keV and 30 keV Ga ion beam	36
5.15	Correlation between SE intensity and sputter yield for 30 keV and 5 keV Ga ion energy on Mo: The crystal orientation data points inside the molybdenum sputter yield IPF (see figure 5.7a and 5.9a) and SE intensity IPF (see 30 keV and 5 keV IPF in figure 5.2b) are correlated with color representing their grain orientation. Please note the observed inversion phenomenon of low energy molybdenum measurements described in section 5.1.1	37
5.16	SE intensity energy series IPF for copper (a) and platinum (b): The count IPF in the bottom right corner is same for all measurements as images were taken from the same area. Platinum results were corrected with a second order linear fit. The unprocessed SE intensity IPF for platinum and all SD IPF are listed in appendix A.4.2	38
5.17	Cu 30 keV Ga ion energy SE intensity IPF (a), count IPF (b) and SD IPF (c): This plot is a magnified figure from the SE intensity energy series of Cu (see figure 5.16a)	39
5.18	Pt 30 keV Ga ion energy SE intensity IPF (a), count IPF (b) and SD IPF (c): This plot is a magnified figure from the SE intensity energy series of Pt (see figure 5.16b)	39
5.19	SE intensity image of platinum before (a) and after (b) quadratic shading correction	40
5.20	CLSM image of platinum specimen: The spherical warp of the sample spans about 1 μm	40
5.21	Shading correction paraboloids for each energy in the platinum SE intensity energy series (see figure 5.16b): The pixel in the x-y-plane are assigned the 8 Bit contrast value of the fitted surface.	41
5.22	Cu CLSM height data before (a) and after (b) sputtering: Difference microscopy requires the selection of 4 identical points inside both plots. The missing markers did not allow reliable selection of these points and thus difference microscopy could not be utilized for copper sputtering.	42

5.23	Cu 30 keV Ga ion energy sputter yield IPF (a), count IPF (b) and SD IPF (c)	43
5.24	Pt 30 keV Ga ion energy sputter yield IPF (a), count IPF (b) and SD IPF (c)	43
5.25	Cu 5 keV Ga ion energy sputter yield IPF (a), count IPF (b) and SD IPF (c)	44
5.26	Pt 5 keV Ga ion energy sputter yield IPF (a), count IPF (b) and SD IPF (c)	44
5.27	Linescan sputter yield of 30 keV Ga ion energy of Pt and Cu overlaid on data generated with rotation of single-crystals and 20 keV argon ion energy [24]: The polynomial regression curves of Pt and Cu are 15th order fits to the data points.	45
5.28	Comparison of SE intensity IPF and sputter yield IPF for copper sputtering with a 5 keV and 30 keV Ga ion beam	46
5.29	Correlation between SE intensity and sputter yield for 30 keV and 5 keV Ga ion energy on Cu: The crystal orientation data points inside the Cu sputter yield IPF (see figure 5.23a and 5.25a) and SE intensity IPF (see 30 keV and 5 keV IPF in figure 5.16a) are correlated with color representing their grain orientation. Please note the absence of difference microscopy for sputter yield measurement.	47
5.30	Comparison of SE intensity IPF and sputter yield IPF for platinum sputtering with a 5 keV and 30 keV Ga ion beam	48
5.31	Correlation between SE intensity and sputter yield for 30 keV and 5 keV Ga ion energy on Pt: The crystal orientation data points inside the Pt sputter yield IPF (see figure 5.24a and 5.26a) and SE intensity IPF (see 30 keV and 5 keV IPF in figure 5.16b) are correlated with color representing their grain orientation. Please note the absence of grain orientations close to the (100) and (111) corner in the 30 keV IPF and close to the (111) corner in the 5 keV IPF, together with the presence of the platinum SE intensity shading described in section 4.5.4 and 5.2.1. The correlation plot without quadratic shading correction can be found in appendix A.4.2. The unprocessed dataset did not display a robust linear correlation.	49
A.1	Data processing with python shading correction tool	II
A.2	A fitted paraboloid surface (a) on corresponding intensity data (b)	III
A.3	CLSM images of all 4 specimens	IV
A.4	Evaluation of minimum error optimization: The SE intensity IPF in the bottom right cell display clearer edges around the maxima compared to the unoptimized IPF. The angle optimization process is elaborated in section 4.5.5.	V

A.5	Comparison between molecular dynamic simulation [25] sputter yield IPF (a) and experimental sputter yield IPF (b) for 30 keV Ga ion energy on a copper target: Please note the absence of difference microscopy due to problems mentioned in section 5.2.2. Zero-scaled sputter yield IPF for all 4 specimens can be found in appendix A.4.4	VI
A.6	The bcc SE intensity energy series IPF for tungsten (a) with corresponding SD IPFs (b) and molybdenum (c) with corresponding SD IPFs (d)	VII
A.7	The fcc SE intensity energy series IPF for copper (a) with corresponding SD IPFs (b) and platinum (c) with corresponding SD IPFs (d)	VIII
A.8	SE intensity energy series IPF for platinum (a) and corresponding SD IPF (b) without quadratic shading correction	IX
A.9	Correlation between SE intensity and sputter yield for 30 keV and 5 keV Ga ion energy on Pt without quadratic shading correction: The crystal orientation data points inside the Pt sputter yield IPF and SE intensity IPF are correlated with color representing their grain orientation. Please note the presence of the platinum SE intensity shading described in sections 4.5.4 and 5.2.1.	X
A.10	bcc linescans along one edge of the sputter yield IPF: Linescans in column (a) are from the left (100) corner to the right (101) corner and linescans in column (b) are from the left (100) corner to the top (111) corner in an IPF.	XI
A.11	fcc linescans along one edge of the sputter yield IPF: The regression curve is a 15th order fit. Linescans in column (a) are from the left (100) corner to the right (101) corner and linescans in column (b) are from the left (100) corner to the top (111) corner in an IPF.	XII
A.12	Reference bcc sputter yield IPFs	XIII
A.13	Reference fcc sputter yield IPFs	XIV

Appendix A

Appendices

A.1 Shading Correction Python Tool

Each image from a polycrystalline specimen containing a large quantity of grains should have an average intensity value over its surface. Due to previously elaborated reasons in the intensity shade section 4.5.4, some results displayed a visual shade in the intensity image, so the SE emission efficiency average over the complete imaged area deviated from its expected constant value. Data processing can correct this shading post measurement.

Figure A.1 shows the steps performed by the tool. The input image is converted to a data array. The mean intensity of all data values is calculated for later subtraction. The data array is then downsampled by local mean in 2x2 (or larger definable) pixel-clusters to increase computing speed. Downsampled results display similar results as the original image as long as the downsampled image does not lose local intensity information. The data is then fitted with a linear or quadratic approximation of a plane or paraboloid. One such paraboloid is shown in figure A.2. The fitted surface is upsampled to match the input array dimension with the help of its surface defining coefficients for the subtraction. Levelling subtracts the fitted surface from the original intensity data around its mean intensity. This new array is then reconverted to an image for future data processing.

Common errors during software usage include an unsupported image format. The input image needs to be successfully converted into an array for the following steps to work. A png image of the wrong bit-depth might get converted into a higher dimensional array and the following code sequences cannot discern the correct intensity data. A png image with a bit-depth of 8 was tested and verified. The input image should only consist of the specimen as any borders around the intensity image, e.g. additional information on scale or SEM magnification, are interpreted as height data points. This falsifies the parameters of the fitted surface. The use of linear and quadratic fitting should be considered carefully. Quadratic correction may correct higher order errors, but potential overfitting bears a risk. This tool only removes the intensity shade in images and can thus be utilized for other studies as well.

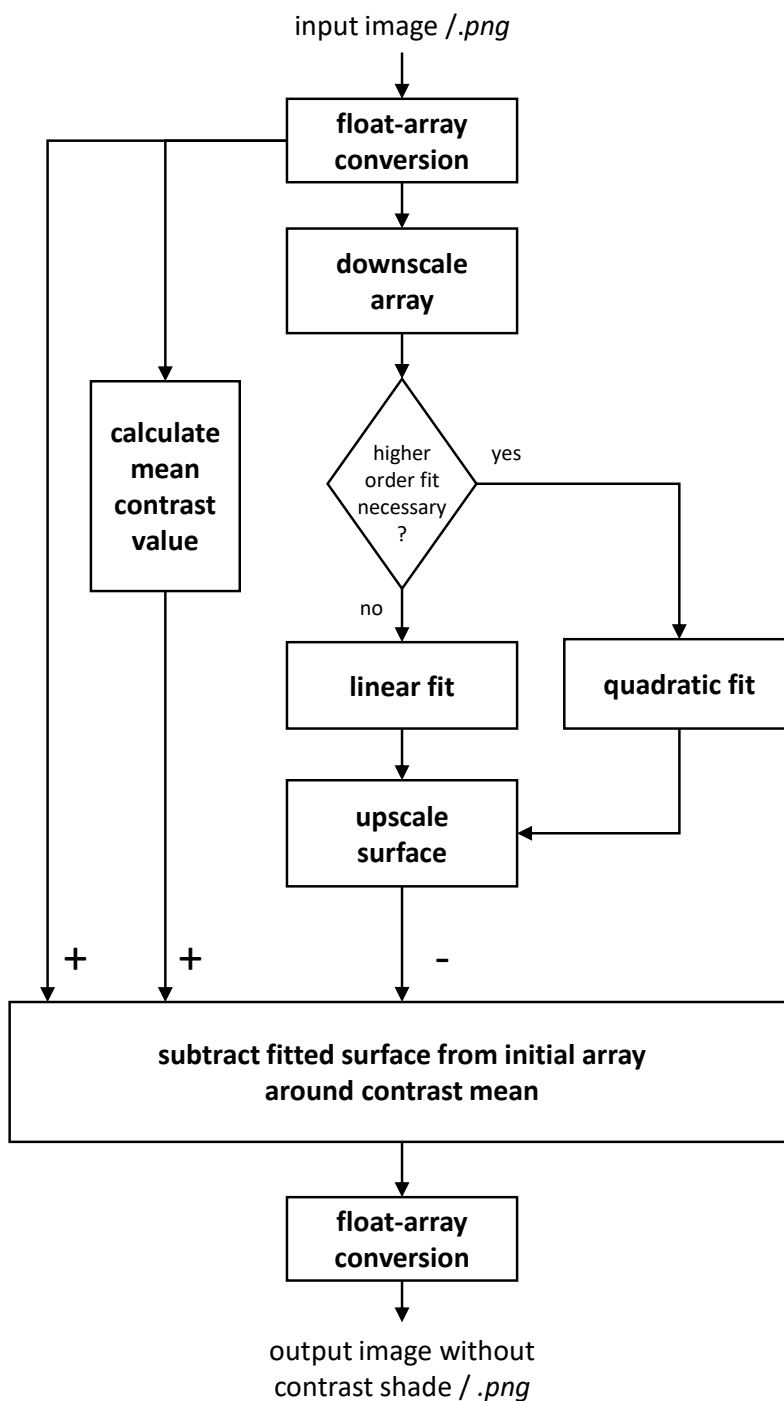


Figure A.1: Data processing with python shading correction tool

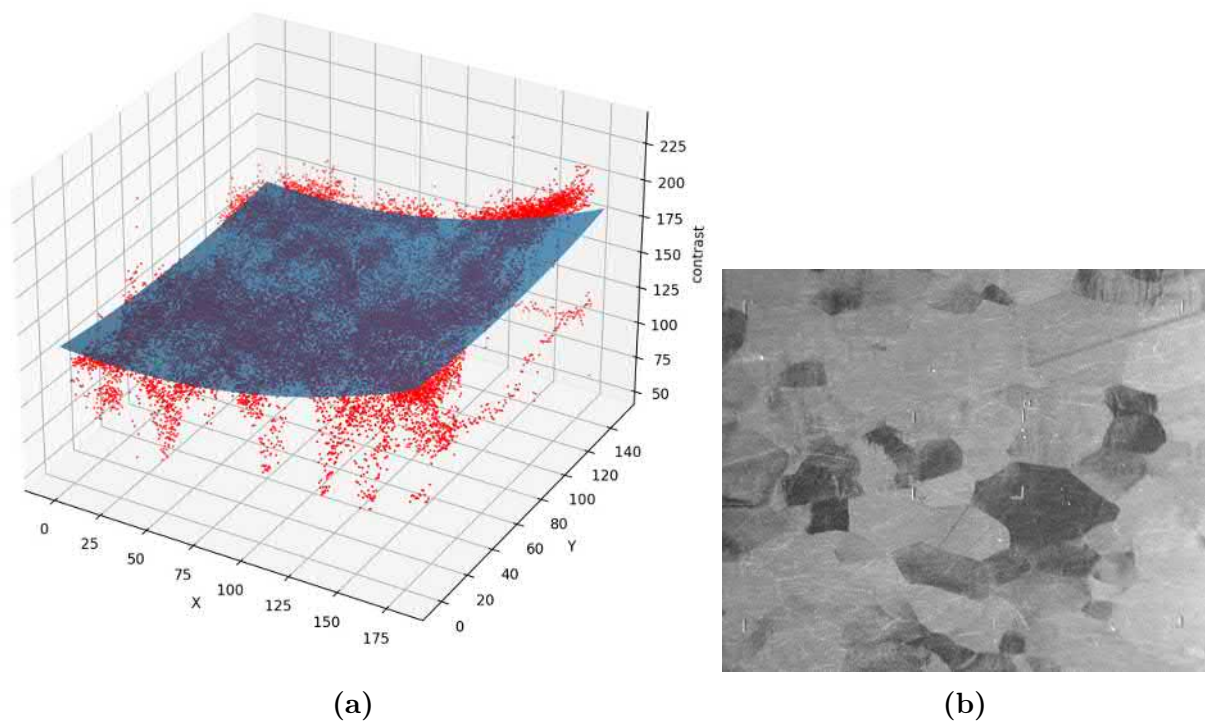
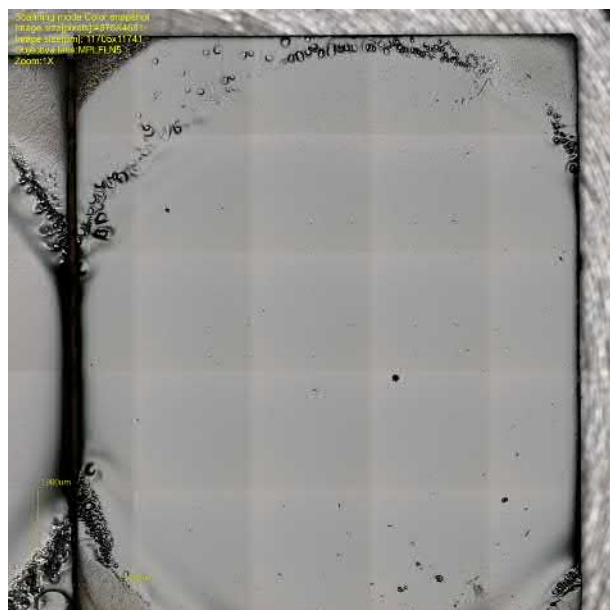


Figure A.2: A fitted paraboloid surface (a) on corresponding intensity data (b)

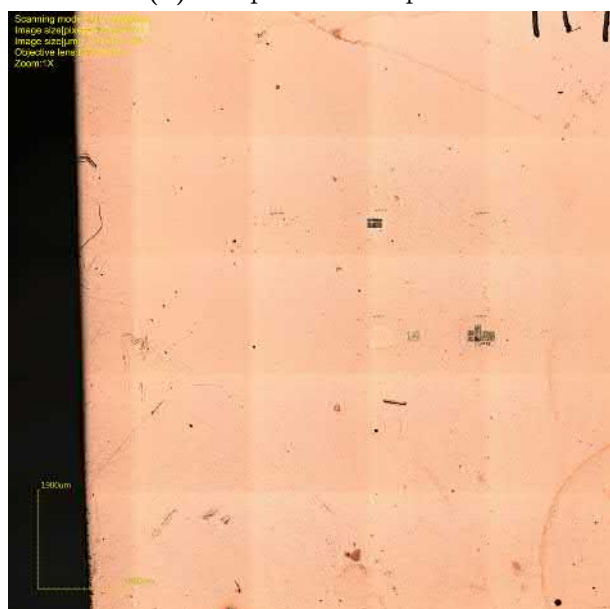
A.2 Specimen Snapshots



(a) W specimen snapshot



(b) Mo specimen snapshot



(c) Cu specimen snapshot



(d) Pt specimen snapshot

Figure A.3: CLSM images of all 4 specimens

A.3 Optimization Filters

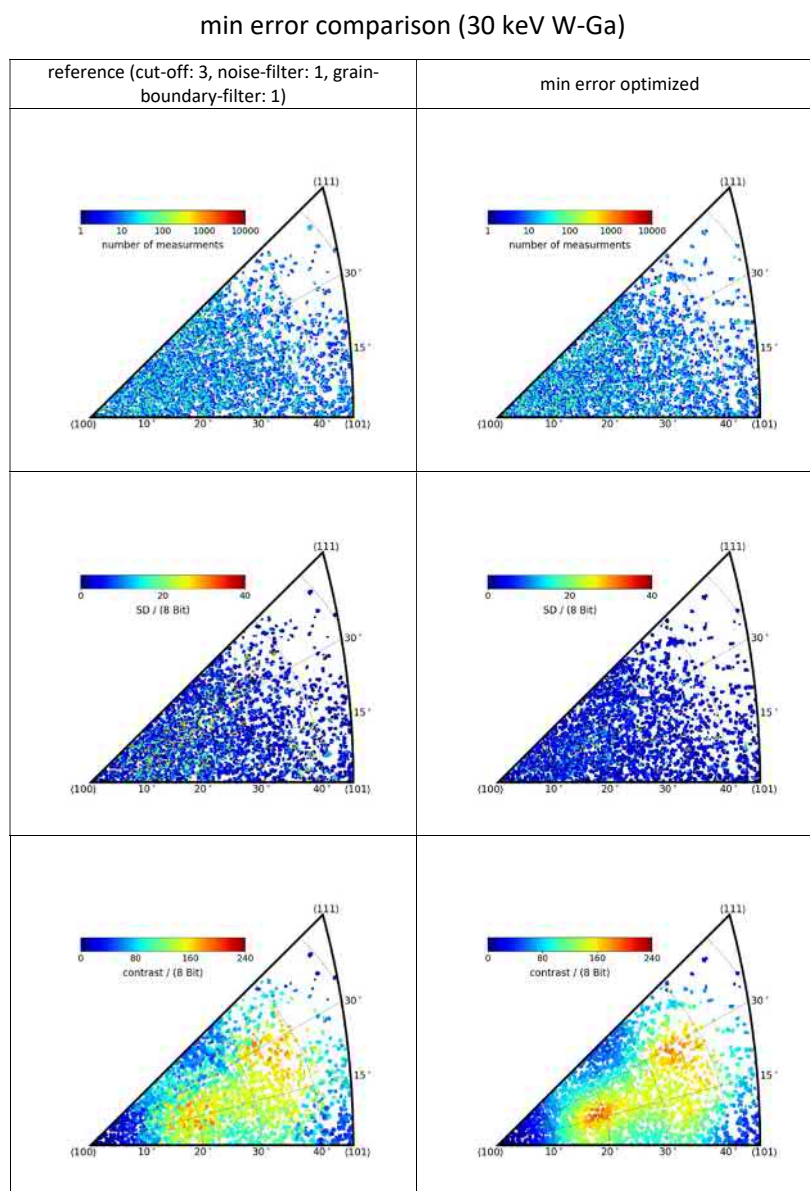


Figure A.4: Evaluation of minimum error optimization: The SE intensity IPF in the bottom right cell display clearer edges around the maxima compared to the unoptimized IPF. The angle optimization process is elaborated in section 4.5.5.

A.4 Supplementary IPF and Data

This section contains additional IPFs and plots generated for the purpose of reference.

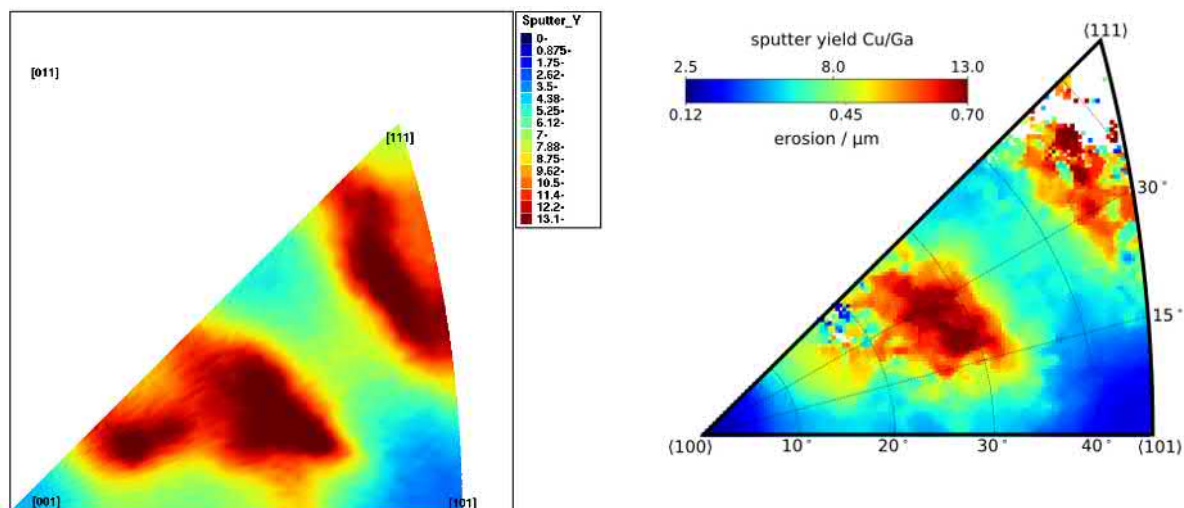


Figure A.5: Comparison between molecular dynamic simulation [25] sputter yield IPF (a) and experimental sputter yield IPF (b) for 30 keV Ga ion energy on a copper target: Please note the absence of difference microscopy due to problems mentioned in section 5.2.2. Zero-scaled sputter yield IPF for all 4 specimens can be found in appendix A.4.4

A.4.1 SE Energy Series IPF

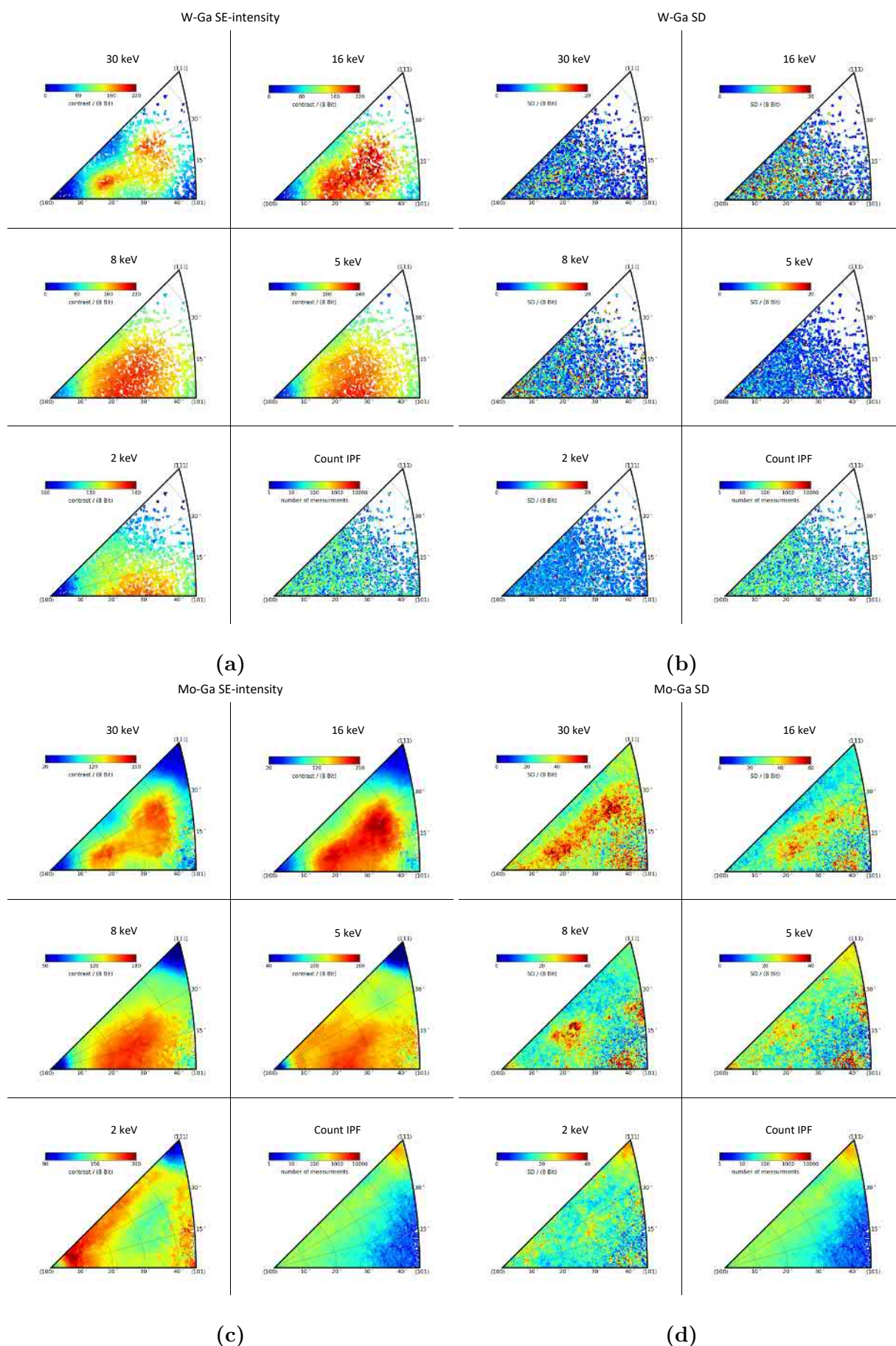


Figure A.6: The bcc SE intensity energy series IPF for tungsten (a) with corresponding SD IPFs (b) and molybdenum (c) with corresponding SD IPFs (d)

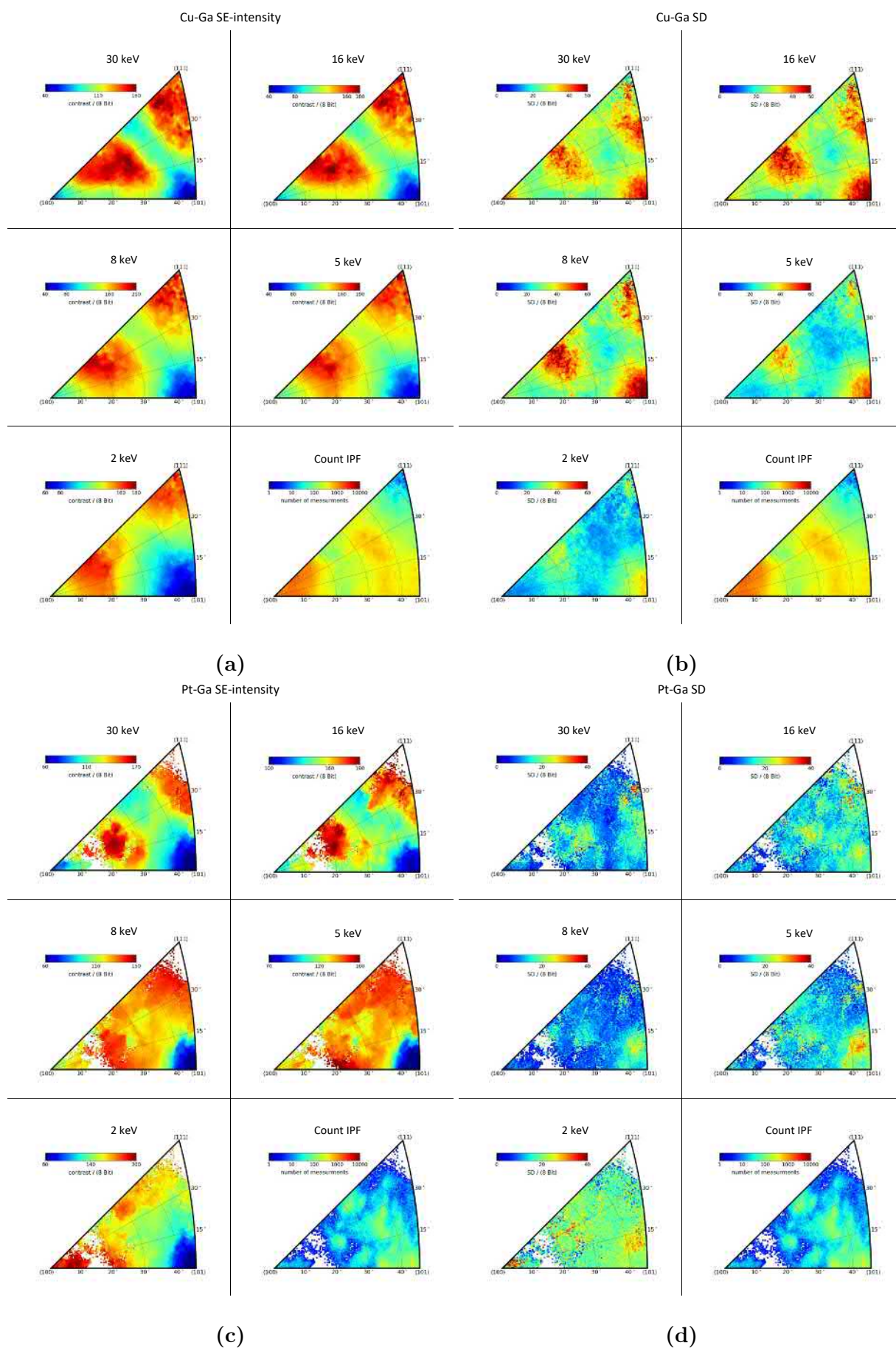


Figure A.7: The fcc SE intensity energy series IPF for copper (a) with corresponding SD IPFs (b) and platinum (c) with corresponding SD IPFs (d)

A.4.2 Platinum Data without Shading Correction

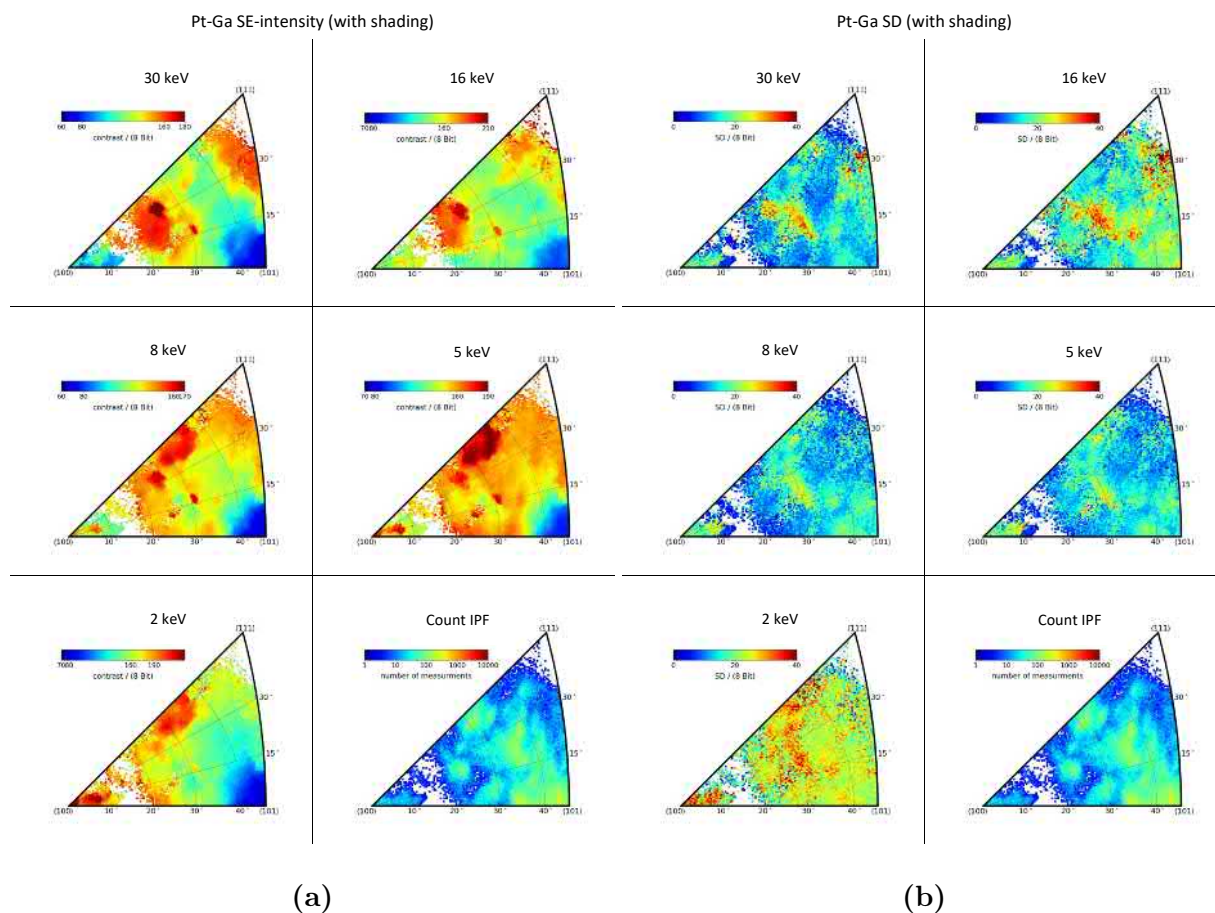


Figure A.8: SE intensity energy series IPF for platinum (a) and corresponding SD IPF (b) without quadratic shading correction

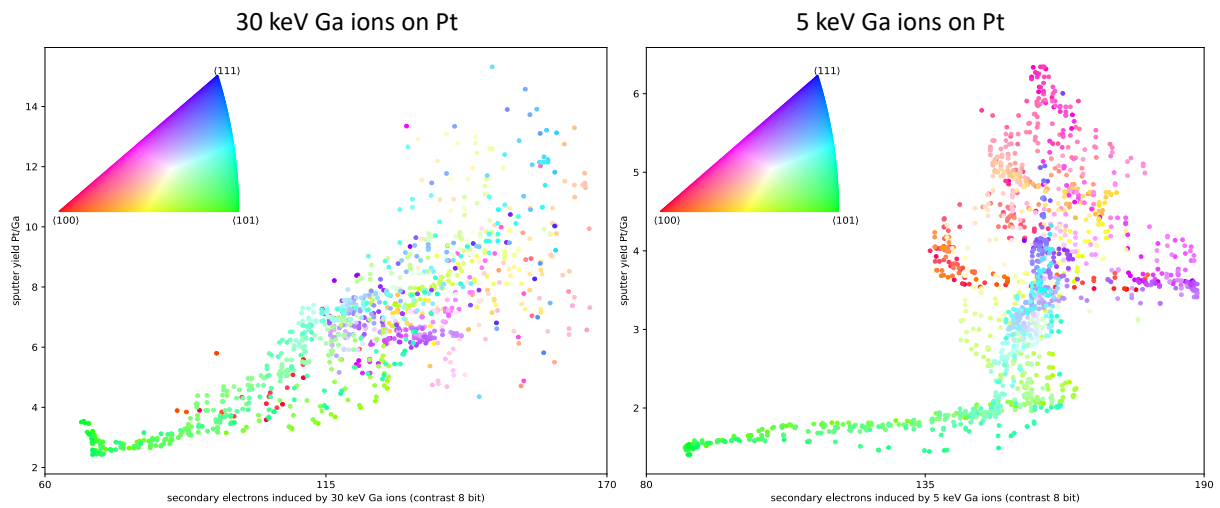


Figure A.9: Correlation between SE intensity and sputter yield for 30 keV and 5 keV Ga ion energy on Pt without quadratic shading correction: The crystal orientation data points inside the Pt sputter yield IPF and SE intensity IPF are correlated with color representing their grain orientation. Please note the presence of the platinum SE intensity shading described in sections 4.5.4 and 5.2.1.

A.4.3 Sputter Yield IPF Linescans

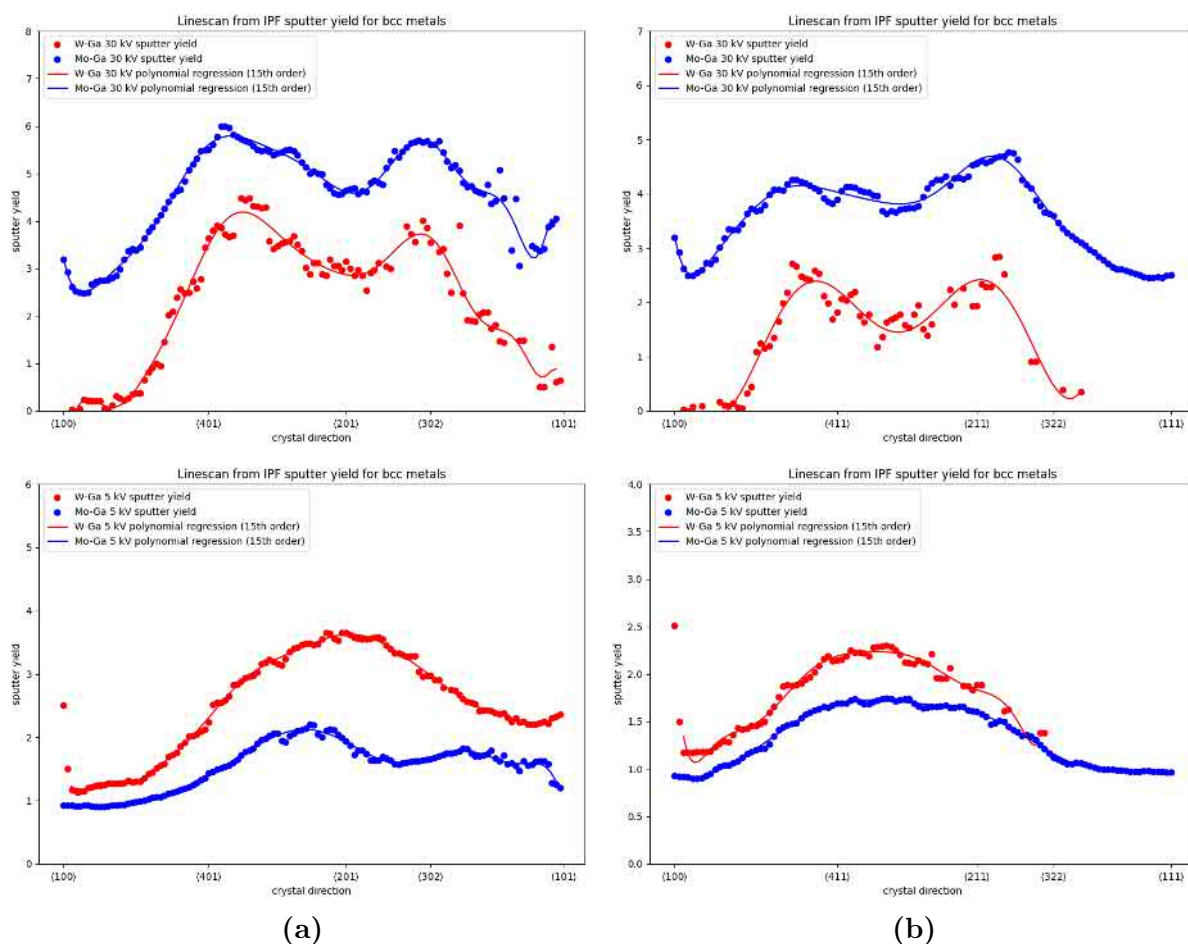


Figure A.10: bcc linescans along one edge of the sputter yield IPF: Linescans in column (a) are from the left (100) corner to the right (101) corner and linescans in column (b) are from the left (100) corner to the top (111) corner in an IPF.

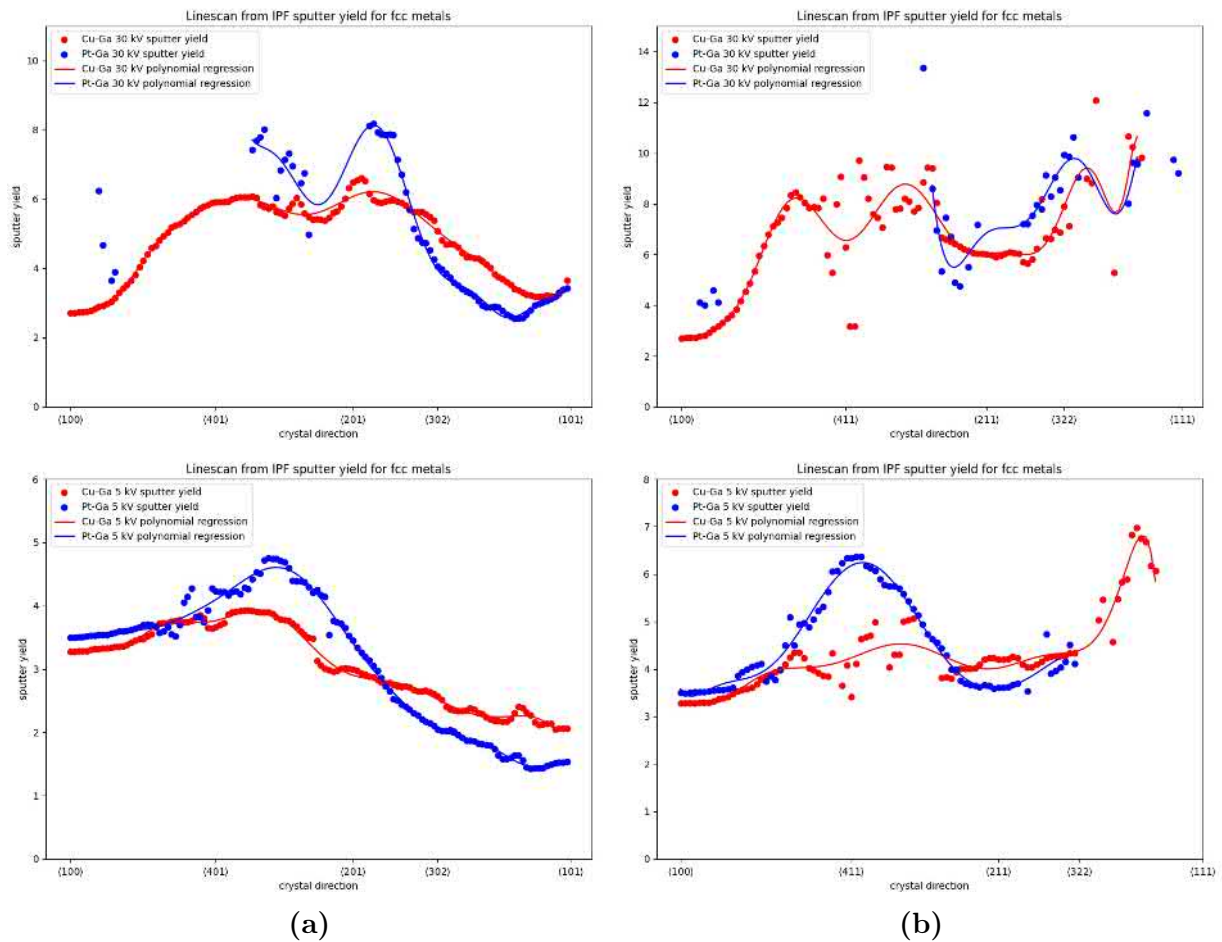
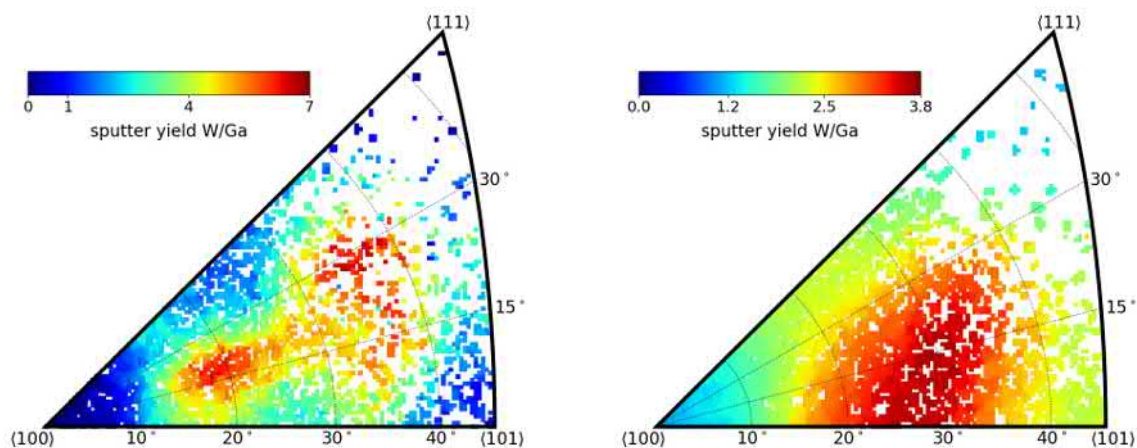


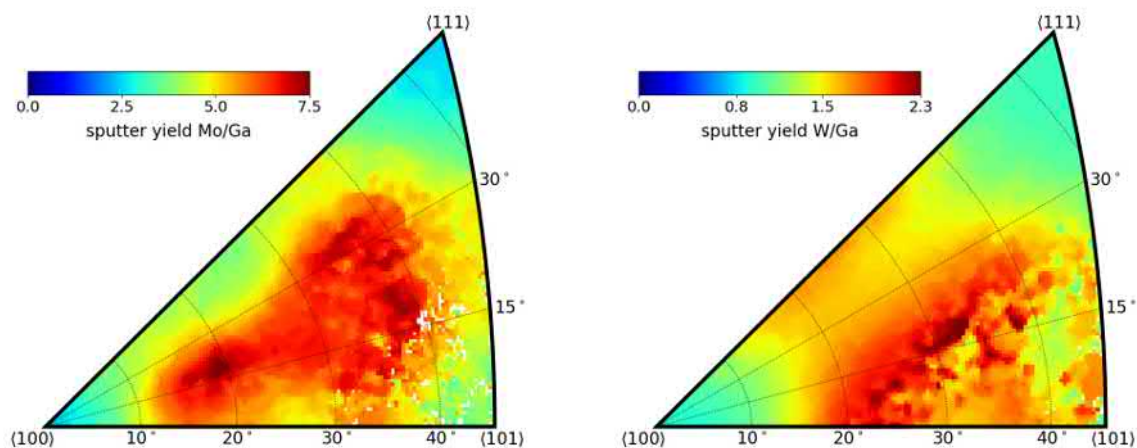
Figure A.11: fcc linescans along one edge of the sputter yield IPF: The regression curve is a 15th order fit. Linescans in column (a) are from the left (100) corner to the right (101) corner and linescans in column (b) are from the left (100) corner to the top (111) corner in an IPF.

A.4.4 Reference Sputter Yield IPF

All sputter yield IPFs from the conducted sputter yield measurements in sections 5.1.2 and 5.2.2 are listed in this section. The scale is adjusted to begin with a sputter yield of zero.

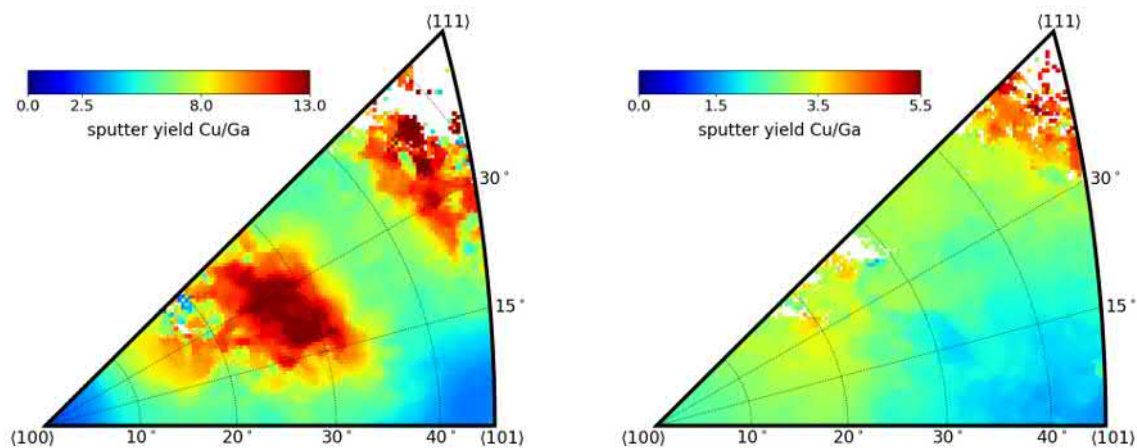


(a) W 30 keV Ga ion energy sputter yield IPF (b) W 5 keV Ga ion energy sputter yield IPF

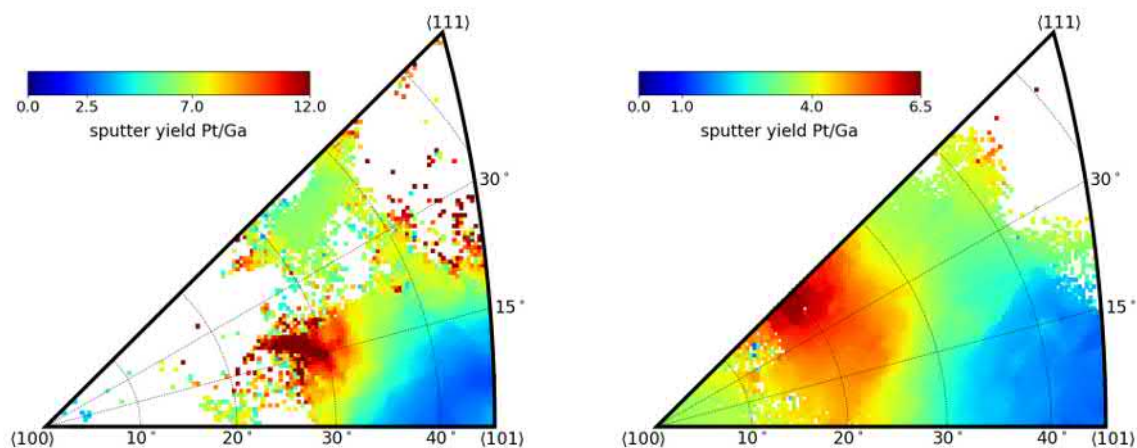


(c) Mo 30 keV Ga ion energy sputter yield IPF (d) Mo 5 keV Ga ion energy sputter yield IPF

Figure A.12: Reference bcc sputter yield IPFs



(a) Cu 30 keV Ga ion energy sputter yield IPF: (b) Cu 5 keV Ga ion energy sputter yield IPF: Please note the absence of difference microscopy and resulting errors in the IPF (see section 5.2.2).



(c) Pt 30 keV Ga ion energy sputter yield IPF (d) Pt 5 keV Ga ion energy sputter yield IPF

Figure A.13: Reference fcc sputter yield IPFs